

## All-optical control of the g-factor in self-assembled (In,Ga)As/GaAs quantum dots

**Citation for published version (APA):**

Quax, G. W. W. (2008). *All-optical control of the g-factor in self-assembled (In,Ga)As/GaAs quantum dots*. [Phd Thesis 1 (Research TU/e / Graduation TU/e), Applied Physics and Science Education]. Technische Universiteit Eindhoven. <https://doi.org/10.6100/IR636945>

**DOI:**

[10.6100/IR636945](https://doi.org/10.6100/IR636945)

**Document status and date:**

Published: 01/01/2008

**Document Version:**

Publisher's PDF, also known as Version of Record (includes final page, issue and volume numbers)

**Please check the document version of this publication:**

- A submitted manuscript is the version of the article upon submission and before peer-review. There can be important differences between the submitted version and the official published version of record. People interested in the research are advised to contact the author for the final version of the publication, or visit the DOI to the publisher's website.
- The final author version and the galley proof are versions of the publication after peer review.
- The final published version features the final layout of the paper including the volume, issue and page numbers.

[Link to publication](#)

**General rights**

Copyright and moral rights for the publications made accessible in the public portal are retained by the authors and/or other copyright owners and it is a condition of accessing publications that users recognise and abide by the legal requirements associated with these rights.

- Users may download and print one copy of any publication from the public portal for the purpose of private study or research.
- You may not further distribute the material or use it for any profit-making activity or commercial gain
- You may freely distribute the URL identifying the publication in the public portal.

If the publication is distributed under the terms of Article 25fa of the Dutch Copyright Act, indicated by the "Taverne" license above, please follow below link for the End User Agreement:

[www.tue.nl/taverne](http://www.tue.nl/taverne)

**Take down policy**

If you believe that this document breaches copyright please contact us at:

[openaccess@tue.nl](mailto:openaccess@tue.nl)

providing details and we will investigate your claim.

**All-optical control of the  $g$ -factor in self-assembled  
(In,Ga)As/GaAs quantum dots**

PROEFSCHRIFT

ter verkrijging van de graad van doctor aan de  
Technische Universiteit Eindhoven, op gezag van de  
Rector Magnificus, prof.dr.ir. C.J. van Duijn, voor een  
commissie aangewezen door het College voor  
Promoties in het openbaar te verdedigen  
op maandag 22 september 2008 om 16.00 uur

door

Guido Wouter Willem Quax

geboren te Breda

Dit proefschrift is goedgekeurd door de promotoren:

prof.dr. P.M. Koenraad

en

prof.dr. M.E. Flatté

Copromotor:

dr. A.Yu. Silov

This work has been financially supported by the COBRA Inter-University Research Institute on Communication Technology. Financial support is also received from NanoNed, a nanotechnology program of the Dutch Ministry of Economic Affairs and part of the research program of FOM, which is financially supported by NWO.

A catalogue record is available from the Eindhoven University of Technology Library  
ISBN 978-90-386-1355-0

© 2008 G.W.W. Quax Text and figures, unless credited otherwise

© 2007 Elsevier B.V. Figure 4.4, Figure 4.8 and Figure 4.9

All rights reserved. No part of this publication may be reproduced in any form without the written consent of the author or copyright owner.

Printed by the printservice of the Eindhoven University of Technology

Cover design by Oranje Vormgevers B.V. and Guido Quax

The plots on the cover are, from left to right, the steady-state photoluminescence spectrum of the (In,Ga)As quantum dots as a function of the laser excitation density (Fig. 4.4), the photoluminescence as a function of time (Fig. 5.3A), and the electroluminescence as a function of voltage (Fig. 3.14).

I think you and Uhlenbeck  
have been very lucky to get your  
spinning electron published and talked  
about before Pauli heard of it. It  
appears that more than a year ago  
Kronig believed in the spinning electron  
and worked out something; the first  
person he showed it to was Pauli.  
Pauli ridiculed the whole thing so  
much that the first person became also  
the last and no one else heard anything  
of it. Which all goes to show that  
the infallibility of the Deity does not  
extend to his self-styled vicar on earth.

Part of a letter by L.H. Thomas to S.A. Goudsmit (dated March 25<sup>th</sup>, 1926), illustrating the social context of the discovery of the electron spin by Uhlenbeck and Goudsmit (1925). Reproduced from a transparency shown by Goudsmit during a lecture for the Dutch Physical Society in 1971. The original is presumably in the Goudsmit archive kept by the AIP Center for History of Physics. More information can be found on [www.lorentz.leidenuniv.nl/history/spin/goudsmit](http://www.lorentz.leidenuniv.nl/history/spin/goudsmit) and [..../history/spin/spin](http://www.lorentz.leidenuniv.nl/history/spin/spin). Courtesy of C.W.J. Beenakker of the Lorentz Institute at the University of Leiden.





# Contents

<b>1</b>	<b>Introduction</b>	<b>7</b>
1.1	Self-assembled III-V semiconductor quantum dots . . . . .	8
1.2	Motivation and context of this thesis . . . . .	16
<b>2</b>	<b>Quantum dots in magnetic and electric fields</b>	<b>21</b>
2.1	Magnetic field effects in semiconductor nanostructures . . . . .	22
2.2	Electric field effects in semiconductor nanostructures . . . . .	29
<b>3</b>	<b>Experimental techniques &amp; sample</b>	<b>33</b>
3.1	Magneto-optical setup . . . . .	34
3.2	Time-resolved Photoluminescence setup . . . . .	41
3.3	Time-resolved Kerr rotation setup . . . . .	43
3.4	Sample structure . . . . .	45
3.5	Electrical characterization of the structure . . . . .	46
<b>4</b>	<b>All-optical control of the exciton <math>g</math> factor in (In,Ga)As quantum dots</b>	<b>51</b>
4.1	Introduction . . . . .	52
4.2	Model . . . . .	53
4.3	Photoluminescence and Stark shifts . . . . .	62
4.4	Sign reversal of the exciton $g$ factor . . . . .	67
4.5	Spin relaxation time as a function of magnetic field . . . . .	72
<b>5</b>	<b>Radiative recombination times of (In,Ga)As quantum dots in electric fields</b>	<b>77</b>
5.1	Introduction . . . . .	78
5.2	Model . . . . .	79
5.3	Results . . . . .	82
5.4	Discussion . . . . .	88

<b>6 Time-Resolved Kerr rotation spectroscopy on (In,Ga)As quantum dots</b>	<b>91</b>
6.1 Introduction . . . . .	93
6.2 Model . . . . .	94
6.3 Results . . . . .	100
6.4 Discussion . . . . .	106
<b>Summary</b>	<b>109</b>
<b>Acknowledgements</b>	<b>112</b>
<b>Bibliography</b>	<b>115</b>
<b>Curriculum Vitae</b>	<b>123</b>

## CHAPTER 1

# Introduction

### ABSTRACT

This chapter discusses the growth process and electronic properties of self-assembled quantum dots, with an emphasis on (In,Ga)As/GaAs quantum dots. We give an overview of the most influential experimental work on this type of quantum dots. We explain for what purpose controllable  $g$  factors are needed, and discuss a *gedankenexperiment* on spin echo's without radio-frequency waves.

## 1.1 Self-assembled III-V semiconductor quantum dots

Self-assembled semiconductor quantum dots are crystalline clusters of a semiconductor compound embedded in a semiconductor host material. Since the late 1980's, they have been studied in fundamental physics and applied in opto-electronics. Next to the applications in for example lasers, they can act as memory devices or (infrared) detectors as well. The quantum dot can be described by a potential well, confining charge carriers in all three directions. As their name suggest, sizes of quantum dots (diameter  $\sim 10 - 30$  nm, height  $\sim 2 - 8$  nm) are such that a zero-dimensional electronic system is formed. Their fully quantized energy spectrum makes them attractive for quantum information processing purposes (Loss and DiVincenzo, 1998), which is the main motivation of this thesis. We, however, first focus on the general properties of quantum dots and introduce the growth procedure, electronic structure and some important experiments on quantum dots.

### Growth procedure

The epitaxial techniques which can be employed for the growth of quantum dots are molecular beam epitaxy (MBE), metal-organic vapor deposition (MOCVD), and chemical beam epitaxy (CBE) (for an overview, see Petroff and DenBaars (1994) and Nötzel (1996)). Quantum dot growth can be performed in the Stranski-Krastanow growth mode, a type of epitaxial growth of two semiconductor compounds with a different lattice constant. In this growth mode, a thin (wetting) layer of the material with the largest lattice constant is formed on the substrate. Lattice strain builds up during this process. At a critical thickness, determined by the lattice mismatch of the materials, the strain can not be accommodated anymore and coherently strained quantum dots are formed. A transition from two-dimensional to three-dimensional growth is made at this point. Since the three-dimensional islands have a coherent strain distribution, no defects are formed, which results in good optical properties.

A Stranski-Krastanow growth mode is, for example, possible for InAs on GaAs, where InAs forms the quantum dots in the GaAs host material. These materials have a lattice mismatch of 7.2 %. For (In,Ga)As island formation to occur, the concentration of In should at least be 20 %, which corresponds to a minimum lattice mismatch of about 1 %. Typical (In,Ga)As quantum dot islands have a height between 2 nm and 8 nm and a base diameter between 10 nm and 30 nm. Both lens-shaped and truncated pyramid shapes have been observed for these quantum dots (Bruls *et al.*, 2002; Gong *et al.*, 2004). In the process of (In,Ga)As quantum dot formation, up to 50-60 % Ga can be intermixed into the quantum dot (Heyn and Hansen, 2003; Heyn *et al.*, 2005).

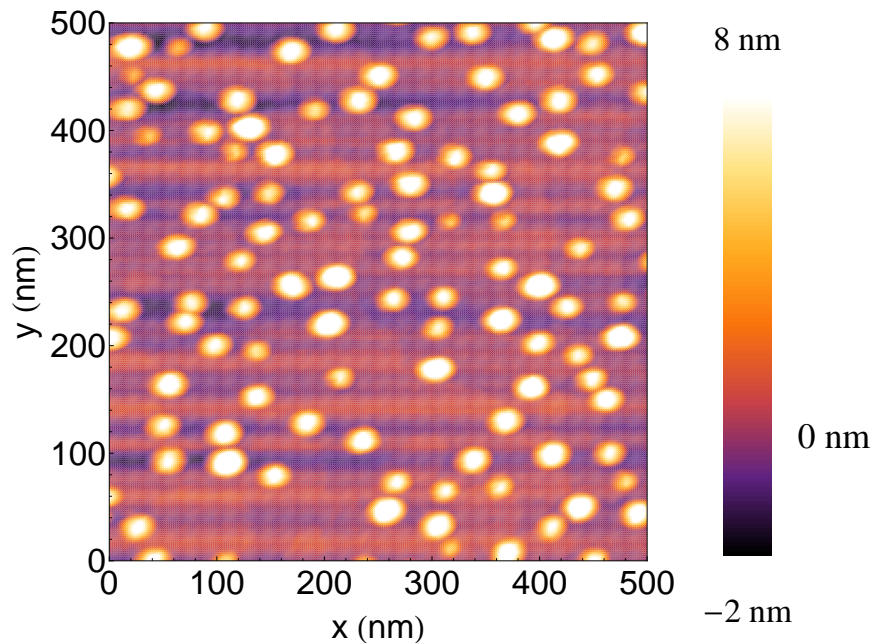


**Figure 1.1:** An atomic-force microscopy (AFM) image of a  $500 \times 500$  nm surface on which Stranski-Krastanow quantum dots are grown. These quantum dots have a surface density  $4.5 \times 10^{10} \text{ cm}^{-2}$ , a base diameter of  $25 \pm 5$  nm and a height of  $6.7 \pm 1.5$  nm. The 0 nm in the scale refers to the height above which only quantum dots occur (see also Fig. 3.9).

The size, shape, degree of intermixing, and surface density can be controlled by the temperature of the sample substrate, deposition rate, growth interrupts, and possible treatment afterwards, like annealing (Joyce *et al.*, 1998; Alloing *et al.*, 2007). Quantum dot surface densities range from  $10^8 \text{ cm}^{-2}$  up to  $10^{11} \text{ cm}^{-2}$ . Figure 1.1 shows an example of a  $500 \times 500$  nm surface on which quantum dots are grown, measured by atomic-force microscopy (AFM).

Figure 1.2 shows the bandgap and lattice constant of a large number of III-V semiconductor compounds which can be used in MBE growth. The open circles in Fig. 1.2 denote the binary compounds, whereas the lines represent ternary compounds. Note that not all combinations of compounds are suitable for confining quantum dots. The compounds with a lighter mass of the constituent components, like GaAs, InP, and GaP, have larger bandgaps, and are therefore commonly applied as host material for the quantum dots. The relatively large difference in bandgap between InAs and GaAs is attractive, since this results in well-confining quantum dots, even at higher temperatures.

Besides the self-assembled quantum dots, colloidal and electrostatically-defined quantum dots are currently investigated extensively. Colloidal quantum dots are smaller

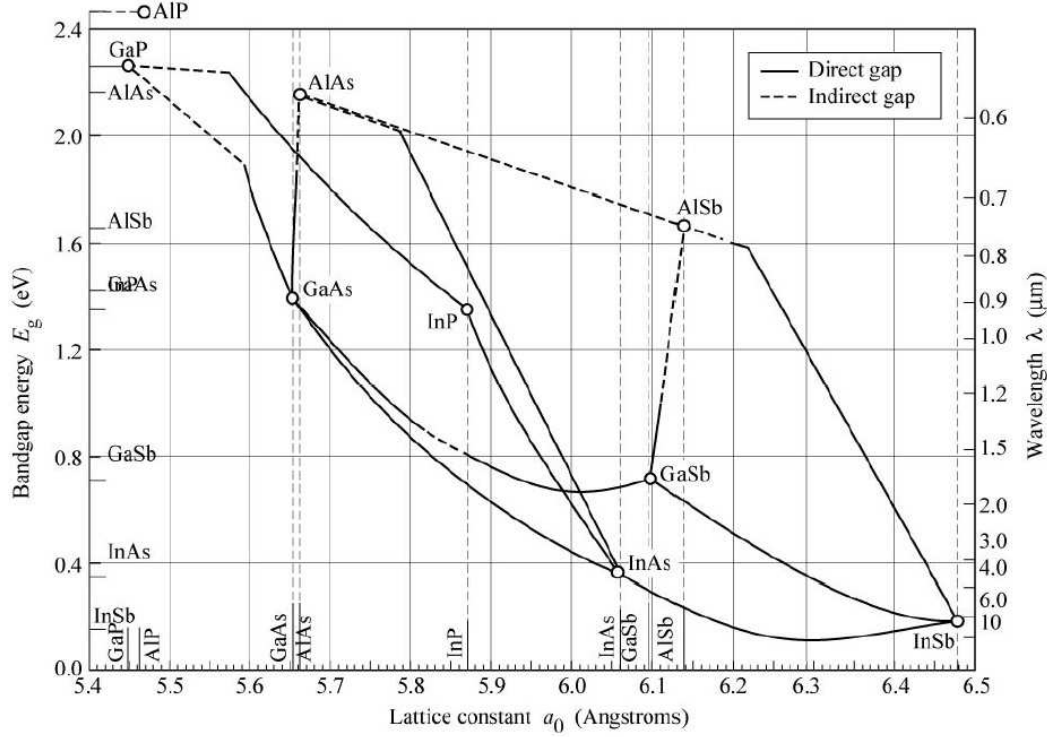


**Figure 1.2:** The bandgap energy as a function of the lattice constant for the III-V semiconductor compounds. Figure is from Tien (1988).

(3-10 nm) than Stranski-Krastonow-grown quantum dots, have good optical properties, and have promising applications in medicine (Rajh *et al.*, 1993). Qubit operation has already been demonstrated by Petta *et al.* (2005) and Koppens *et al.* (2006) for the electrostatically-defined quantum dots.

## Electronic structure

The density-of-states of solid state structures can be derived from the dispersion relation of the band structure and dimensionality of the system. One finds an increasing, constant, and decreasing behavior as a function of energy for the three-, two-, and one-dimensional structures, respectively, which is illustrated in Fig. 1.3. A discrete density-of-states is formed for zero-dimensional structures, i.e., quantum dots. The first experimental observation of such a discrete energy spectrum was made by Reed *et al.* (1987, 1988).

The discrete energy levels of an electron in a quantum dot can be determined from the Hamiltonian

$$\hat{H} = \hat{H}_{kin} + \hat{V} + \hat{\Delta}_Z \quad (1.1)$$

where  $\hat{H}_{kin}$  is the kinetic part of the Hamiltonian and  $\hat{V}$  is the confinement potential of

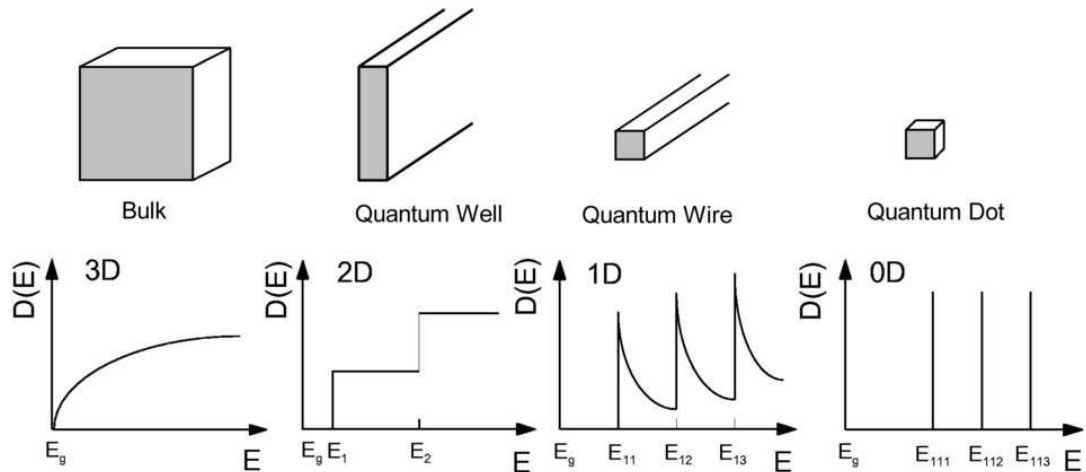


**Figure 1.3:** The density-of-states as a function of the energy  $E$ , shown for the bulk, quantum well, quantum wire and quantum dot. An increasing confinement leads to a lower 'overall' density-of-states. The subscripts, like 112 in  $E_{112}$  in the graph for the quantum dot, are the principal quantum number for each of the confinement directions. Courtesy of F. Scholz (Geiger, 1998, University of Ulm).

the quantum dot. The Zeeman term  $\hat{\Delta}_Z$  relates to the spin part of the wavefunction, describing the energy splitting between spin-up and spin-down energy level, and can be written as

$$\hat{\Delta}_Z = g\mu_B \mathbf{B} \cdot \mathbf{S} \quad (1.2)$$

where  $\mathbf{S}$  denotes the spin and  $\mathbf{B}$  is the magnetic field,  $\mu_B$  is the Bohr magneton and  $g$  is the Landé  $g$  factor. The Bohr magneton is the magnetic dipole moment of an electron with an angular momentum of  $\pm\hbar$ , and reads  $\mu_B = 0.058 \text{ meV/T}$ . The  $g$  factor describes the ratio of the magnetic moment and orbital angular momentum (of the spatial part of the wavefunction), or the ratio of the magnetic moment and the associated 'intrinsic' angular momentum of the spin (for the spin part of the wavefunction). Values for the  $g$  factor occur in a wide range, which is further explained in Ch. 2.

Calculated energy spectra of (In,Ga)As quantum dots are characterized by an energy spacing of the order  $\sim 30 \text{ meV}$  (Stier *et al.*, 1999; Schliwa *et al.*, 2007). One should note, however, that these energies depend on numerous parameters, like the size, shape and material composition of the dot. Other important parameters, which are more difficult to estimate, are the piezoelectric potential distribution and band lineup of the materials (Stier *et al.*, 1999; Schliwa *et al.*, 2007). If one considers multiple carriers in the quantum dot, Coulomb terms do affect the spectrum as well.

In this work, we focus on self-assembled (In,Ga)As quantum dots, grown on GaAs host material. These have transition energies ranging from 1.0 eV up to 1.3 eV and are



smaller than the II-VI quantum dots with transition energies over 2 eV. Differences between the materials occur, for example, in the polarity of the bonding of the crystal: the III-V materials have a weaker polar character. Moreover, the III-V quantum dots have a weaker coupling to the acoustic phonon bath. When spin relaxation is driven by acoustic phonons, one can therefore expect that III-V quantum dots have larger spin relaxation times. This leads to longer spin relaxation times, which we discuss in Ch. 4. Besides this difference between II-VI and III-V quantum dots, one can generally expect a more dense spectrum for the valence electrons than for the conduction electrons in (In,Ga)As quantum dots, due to the band lineup and larger effective mass of the valence electron. Furthermore, intermixing of Ga into the InAs quantum dot decreases the confinement potential well depth, which leads to an overall increase of transition energies.

Both electrical measurements, like C-V measurements (Reuter *et al.*, 2005), as well as optical experiments (Blokland *et al.*, 2007) have been performed to measure the electronic spectrum of (In,Ga)As quantum dots. Optical experiments even have shown results on the fine structure (e.g., exchange energies) (Gammon *et al.*, 1996; Ware *et al.*, 2005). The electric measurements have the advantage that they can easily differentiate between the conduction and valence electron spectrum. Experimental values for the confinement-induced energy spacing between subsequent energy levels (e.g., ground state and first excited state) for the valence electron are  $\sim 40$  meV (Reuter *et al.*, 2005). For the exciton, these energies range from  $\sim 15$  meV (Ediger *et al.*, 2007) up to  $\sim 70$  meV (Blokland *et al.*, 2007), which is deduced from the peaks of subsequent levels in photoluminescence spectra.

We consider the optical selection rules between the conduction and valence electron, since we measure the degree of circular polarization of the photoluminescence in magnetic field. The polarization of the photons is determined by the Bloch functions of the conduction and valence bands. The materials InAs and GaAs have a *s*-type Bloch function ( $L = 0$ ) for the conduction electron and a *p*-type Bloch function ( $L = 1$ ) for the valence electron. One has to couple the spin  $S$  with the angular momentum  $L$  of the Bloch function, such that  $J = L + S$ . This results in fourfold degenerate  $J = 3/2$  states at the top of the valence band and twofold degenerate  $J = 1/2$  states for the split-off subband.

Due to confinement in the quantum dot, the fourfold degenerate  $J = 3/2$  levels split into two twofold degenerate subbands with  $J_z = \pm 3/2$  (heavy holes) and  $J_z = \pm 1/2$  (light holes). The  $J_z = 3/2$  states are at the top of the valence band, and are therefore involved in the lowest-energy optical transitions. We measure the degree of circular polarization from the  $S_z = \pm 1/2$  conduction electron states to the  $J_z = \pm 3/2$  valence

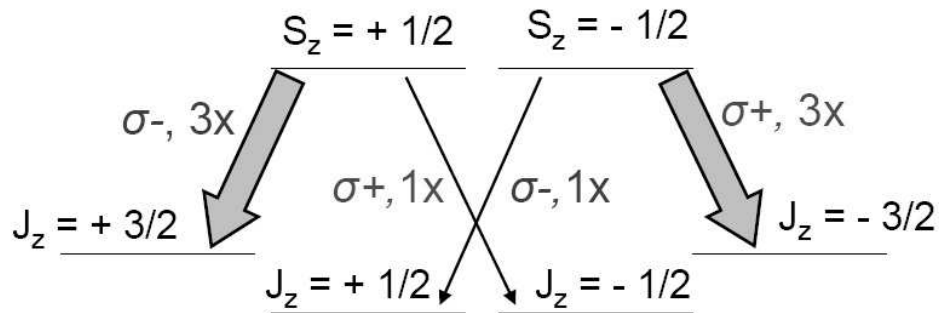


**Figure 1.4:** Optical transitions in the quantum dot occur from the  $S_z = \pm 1/2$  to the  $J_z = \pm 3/2$  (emission of  $\sigma_{\mp}$  photons) and  $J_z = \mp 1/2$  (emission of  $\sigma_{\pm}$  photons) level. The oscillator strength for the transitions involving  $J_z = \pm 1/2$  are three times lower. Note that we use a valence electron point-of-view for the transitions, and not a hole point-of-view.

electron states. When the magnetic field and the propagation direction of the emitted  $\sigma_{\pm}$  photons (i.e., right- (+) and left-handed (-) circularly polarized photons) are pointing in the same  $z$ -direction, the optical transitions from the conduction to valence electrons can be written as  $\pm 1/2 \rightarrow \pm 3/2 + \sigma_{\mp}$  (see Fig. 1.4). The angular momentum of the conduction electron of  $\pm \hbar$  is transferred to the photon. Transitions between the conduction electron and the  $J_z = \pm 1/2$  subband are also allowed, and can be written as  $\pm 1/2 \rightarrow \mp 1/2 + \sigma_{\pm}$ . Due to a different overlap of the heavy- and light-hole Bloch functions, the transition strength for light-holes is three times smaller. Throughout the thesis, we only use the terminology of heavy- and light-hole when differentiation between the  $J_z = \pm 3/2$  and  $J_z = \pm 1/2$  states is required.

Besides the polarization of the photons, originating from the symmetry of the Bloch functions, the oscillator strength  $f$  of these transitions is determined by the overlap of the envelope of the orbital part of the electron and hole wavefunction. The oscillator strength is proportional to the squared matrix element between the initial and final envelope  $\psi_i$  and  $\psi_f$ . When the symmetry of the states  $\psi_i$  and  $\psi_f$  are orthogonal (e.g., a  $s$ -type and  $p$ -type envelope function), the oscillator strength can be zero: the transition would then be forbidden.

A commonly applied notation for the electron-hole pair is the exciton notation. To introduce this, we denote the  $S_z = \pm 1/2$  conduction electron states and  $J_z = \pm 3/2$  valence electron states with  $|\pm 1/2\rangle$  and  $|\pm 3/2\rangle$ , respectively, which is applied throughout the thesis. A bright  $|\pm 1\rangle$  exciton is formed from the  $|\mp 1/2\rangle$  conduction electron and the  $|\mp 3/2\rangle$  valence electron (or  $|\pm 3/2\rangle$  hole). Similarly, dark  $|\pm 2\rangle$  excitons can be formed from a  $|\pm 1/2\rangle$  conduction electron and  $|\mp 3/2\rangle$  valence electron. Only the  $|\pm 1\rangle$  states are optically active, which optical transitions can be written as  $|\pm 1\rangle \rightarrow \sigma_{\pm}$ . In (In,Ga)As quantum dots, the  $|\pm 1\rangle$  states are at a higher energy than the  $|\pm 2\rangle$  states,

due to the exchange interaction energy of the order of  $\lesssim 200 \mu\text{eV}$  (Bayer *et al.*, 1999).

In the case of intermixing of the light hole state into the heavy hole state, one can not expect a complete conversion into photons with one type of helicity. The light-hole fraction in predominantly heavy hole state, quantized by its squared amplitude in the state, emits with opposite helicity (to that of the heavy hole) at a three times weaker strength, which 'dilutes' the conversion. Experiments (Cortez *et al.*, 2001) and calculations (Sheng, 2007), however, have indicated that this light-hole fraction is very small, and does not exceed 10%.

## Important experiments on quantum dots

We briefly discuss some experimental breakthroughs in the field of quantum dots, where we focus on the experiments related to the subjects of this thesis.

Among the most difficult experiments in this field are probably those involving coherence and control of the coherence of charge carriers. The complexity in these measurements arise from the quantum mechanical nature of coherence, for which any environmental disturbance is destructive. These conditions can be met at low temperatures and in a well-controllable system. One of the first measurements on coherence in quantum dots, involving four-wave-mixing to probe the absorption spectrum, revealed a long decoherence time  $T_2^*$  in quantum dots (compared to other solid state structures) (Birkedal *et al.*, 1999; Borri *et al.*, 2001). An other study on coherence effects in quantum dots was done by Chen *et al.* (2000), where they measured a coherent superposition of Zeeman levels. Later, quantum beats in time-resolved photoluminescence spectra proved the coherent precession between two exchange-interaction-split levels (Flissikowski *et al.*, 2001). Rabi oscillations, which occur in the case of coupling of the light field to the discrete levels under strong optical excitation, were observed by Stievater *et al.* (2001), Zrenner *et al.* (2002) and Li *et al.* (2003).

A study with an enormous impact was the measurement on the longitudinal spin relaxation time  $T_1$  of the conduction electron by Kroutvar *et al.* (2004), which was actually anticipated by Paillard *et al.* (2001) and Hanson *et al.* (2003). This revealed that spin relaxation up to milliseconds was possible, and that the spin relaxation times of the conduction electron follow a power law behavior as a function of the magnetic field (i.e.,  $T_1 \sim B^{-5}$ ). This measurements matched exactly with the theoretical predications on spin relaxation, made some years before (Khaetskii and Nazarov, 2000, 2001). In this thesis, we point out that such a power law behavior also exists for the excitons, like in the theoretical prediction (Tsitsishvili *et al.*, 2003), but with a weaker magnetic field dependence (i.e.,  $T_1 \sim B^{-3}$ ).

Kerr/Faraday rotation measurements were introduced to the quantum dot research field by Gupta *et al.* (1999), which was, however, a study on colloidal quantum dots. The first study on embedded III - V quantum dots (MOCVD-grown InP dots on GaAs) was presented by Kanno and Masumoto (2006). The technique had already been applied extensively to bulk semiconductor (Awschalom *et al.*, 1985) and semiconductor quantum wells (Koopmans and de Jonge, 1999; Salis *et al.*, 2001). The first study on (In,Ga)As quantum dots was done by Greulich *et al.* (2006a), who also exploited the coherence properties of the two-level spin system (Greulich *et al.*, 2006b). Their study was based on annealed quantum dots<sup>†</sup>. We present the first study on un-annealed (In,Ga)As quantum dots with high-energy luminescence. Generally speaking, un-annealed quantum dots contain a smaller fraction of Ga than their annealed counterparts.

Besides the optical techniques we have discussed so far, electrical measurements have been performed. They were initially executed on electrostatically-defined quantum dots, which for instance revealed the shell filling behavior of the electrons (i.e., the quantum numbers and chemical potentials of subsequently added electrons) (Tarucha *et al.*, 1996). For self-assembled quantum dots, capacitance-voltage measurements revealed that the hole is positioned at the apex of the quantum dot (Fry *et al.*, 2000b). The same technique showed the filling behavior of the holes in self-assembled quantum dots (Reuter *et al.*, 2005).

Among the milestones in of quantum computation and quantum information, the experiments demonstrating a single spin readout from Elzerman *et al.* (2004) in electrostatically-defined quantum dots should be mentioned. A slightly different optical counterpart, demonstrating the spin state preparation in self-assembled quantum dots, was achieved some years later (Atatüre *et al.*, 2006). Coherent control over the single spins has recently been demonstrated by electron spin resonance (Koppens *et al.*, 2006) in electrostatically-defined quantum dots, which was one of the crucial steps to overcome. This research was succeeded by a demonstration of spin control by alternating electric fields (Nowack *et al.*, 2007). These experiments employed, in fact, actual single qubit quantum computers, allowing full coherent control over the spin. The later experiments of Berezovsky *et al.* (2006, 2008), Atatüre *et al.* (2007) and Mikkelsen *et al.* (2007) should also be mentioned for their measurements of single spins in quantum dots by Kerr and Faraday rotation techniques.

---

<sup>†</sup>The reason for the annealing procedure is the consequent lowering of the transition energy, due to intermixing of Ga. Since the Kerr/Faraday rotation experiments are performed (quasi-)resonantly, the transition energy of the quantum dot and laser should overlap. Because of the decreasing performance of the regularly used Ti:Sapphire laser for wavelengths above 900 nm, an annealing procedure to reduce the transitions wavelengths below 900 nm is desirable.

## 1.2 Motivation and context of this thesis

The quantized energy spectrum of quantum dots, as well as their long spin relaxation time, makes them attractive for quantum information processing purposes (Loss and DiVincenzo, 1998). As possible candidates for quantum information devices, they require a controllable  $g$  factor for selective addressability of the qubits. A general necessity for these devices is to have a long decoherence time, since quantum information employs the phase of the spin. These two issues have been addressed in this thesis, as well as a result on the control of radiative recombination times.

Quantum information typically exploits two-level systems, like the two polarization states of the photon or the spin-up and spin-down states of the electron. Such a system is called a qubit, where the levels are commonly denoted by  $|0\rangle$  and  $|1\rangle$ . Contrary to the regular bit, which adapts 0 *or* 1, the qubit can be described by a (coherent) superposition of these states, like  $\Psi = \alpha|0\rangle + \beta|1\rangle$ , where  $|\alpha|^2 + |\beta|^2 = 1$ . The decay of the phase difference between the  $|0\rangle$  and  $|1\rangle$  state is then described by the decoherence time.

### Control over the $g$ factor

An important parameter for the spin-up and spin-down two-level system is the energy splitting between the levels in a magnetic field, given by the Zeeman energy. This energy difference arises due to an oppositely directed magnetic moment associated with the spin-up and spin-down state.

Let us consider the qubit formed by the Zeeman levels of the quantum dot. Operations on such qubits can be performed by electron spin resonance (ESR), which has recently been demonstrated by Koppens *et al.* (2006) in electrostatically-defined quantum dots. Control over the qubit is achieved when the ESR radio-frequency matches with the precession frequency of the spin state in a magnetic field. Since one wants to address *individual* qubits in an array of quantum dots, it is desirable to have control over the Zeeman energy in each quantum dot (Kane, 1998; Vrijen *et al.*, 2000). Such control over the Zeeman energy, which is proportional to the  $g$  factor, has already been demonstrated in bulk semiconductor material (Kato *et al.*, 2003) and quantum wells (Salis *et al.*, 2001). In this thesis, we show evidence of control of both the *in-plane* and *growth direction*  $g$  factor of the *quantum dot* Zeeman levels by an electric field.

A  $g$  factor which can be reversed in sign would even have more advantages in spin processing schemes. We describe a *gedankenexperiment* on the possible implications of a sign-controllable  $g$  factor. Generally speaking, the control of the spin is performed using radio-frequency waves. Typical control schemes make use of  $90^\circ$  and  $180^\circ$  pulses

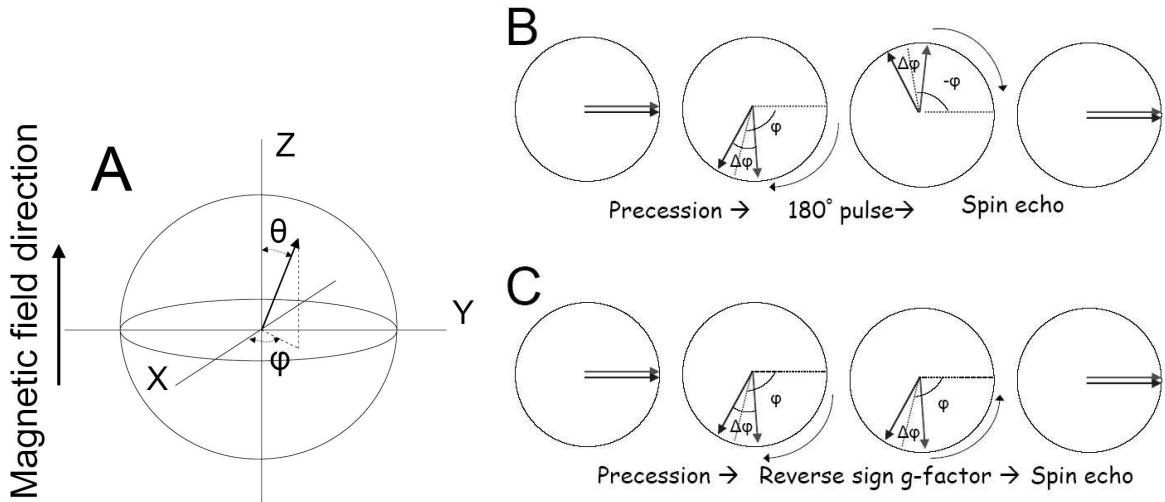


**Figure 1.5:** Figure A shows a geometric representation of the quantum mechanical two-level system, known as the Bloch sphere, where a state is uniquely determined by the angles  $\theta$  and  $\phi$ . The state can be written as  $\psi = \cos(\theta/2)|0\rangle + \sin(\theta/2)e^{i\phi}|1\rangle$ , where  $|0\rangle$  and  $|1\rangle$  are the eigenstates of the spin in a magnetic field pointing in the Z-direction. Longitudinal spin relaxation times  $T_1$  are associated with the spin flip along the Z-direction (or the angle  $\theta$ ), whereas decoherence times  $T_2$  are associated with the precession in the X/Y plane (or the phase  $\phi$ ). Figure B and C show the X/Y plane of the Bloch sphere, where one should read from the left to the right figure. A magnetic field in the Z-direction induces the spin to precess in the X/Y plane with a frequency  $\frac{g\mu_B B}{\hbar}$ . A  $180^\circ$  pulse on the Y axis (Fig. B) would mirror the spin, which leads to a spin echo. Alternatively, a spin echo can be achieved by a reversible  $g$  factor (Fig. C). Note, however, that this is an idealized description, or rather a *gedankenexperiment*, which does not take into account the effect of the electric field on the decoherence process.

that perform rotations of the spin in the Bloch sphere (i.e., a graphical representation of the quantummechanical two-level system, shown in Fig. 1.5A). Since the time-evolution of a coherent superposition of the two spin eigenstates  $|\uparrow\rangle$  and  $|\downarrow\rangle$  can be written as  $\Psi(t) = |\uparrow\rangle + e^{i\delta t}|\downarrow\rangle$ , where  $\delta$  describes the precession frequency of the state by  $\delta = \frac{g\mu_B B}{\hbar}$  (where  $\mu_B$  is the Bohr magneton and  $B$  is the magnetic field), a sign change of the  $g$  factor would result in a reversal of the precession. This has the same effect as a radio-frequent pulse of a certain time duration, resulting in a rotation of the spin on the Bloch sphere. *A sign reversible  $g$  factor could therefore replace the  $180^\circ$  pulse.* Figure 1.5B and 1.5C display the in-plane part (compared to the magnetic field direction) of the Bloch sphere, and show how a reversed  $g$  factor can be employed to form a spin echo. Note, however, that this idealized description does not take into account the decoherence induced by the electric field.



## Spin relaxation times

Besides the control over the  $g$  factor, long decoherence times  $T_2^*$  and longitudinal relaxation times  $T_1$  of the spin system are a general requirement for proper quantum information processing with quantum dots. Preskill (1998) states that approximately  $10^4$  operations should be performed in a decoherence period, for quantum error correction (i.e., a certain type of algorithm in quantum information processing) schemes to work correctly.

Demonstrations on atoms (Anderlini *et al.*, 2007) and electrostatically-defined quantum dots (Elzerman *et al.*, 2004; Gorman *et al.*, 2005; Koppens *et al.*, 2006) have shown that spin operations (typically a  $180^\circ$ -pulse) can be performed in approximately 100 ns. A recent proposal of Pioro-Ladrière *et al.* (2007) introduces an additional lateral magnetic field on this electrostatically-defined structures to reduce the operation speed below 100 ns. While the operation times were initially estimated to be at least 25 ns (Sherwin *et al.*, 1999), recently more efficient methods of operation have been proposed. For instance, quantum operations based on spin-flip Raman transitions could perform operations in the order of 10 ps (Chen *et al.*, 2004). A combination of operation time and the required number of operations leads to an estimate of  $\sim 100$  ns as the required minimum for the decoherence time.

The current experimental results on decoherence times in (In,Ga)As quantum dots have reached  $\sim 10$  ns (Mikkelsen *et al.*, 2007), although decoherence times exceeding 100 ns occur in low doped  $n$ -type bulk material (Kikkawa and Awschalom, 1999). Measurements on the longitudinal spin relaxation time, however, reveal values exceeding 1 ms for both the electron (Kroutvar *et al.*, 2004) and hole (Gerardot *et al.*, 2008) in (In,Ga)As quantum dots. In this thesis, we show that also the exciton  $T_1$  can exceed 100 ns.

## The methods and results of this thesis

In this thesis, we investigate a single layer of self-assembled (In,Ga)As quantum dots in the center of  $p$ - $i$ - $n$  structure. The quantum dots experience an electric field in the growth direction, which can be controlled by photo-created carriers of an (additional) excitation laser. For increasing excitation densities of the laser, the electric field over the quantum dots is suppressed due to screening. The screening effect is very well observed in the Stark shift (i.e., a shift in energy due to the electric field) of the PL spectra.

In chapter 4, we discuss the steady-state photoluminescence and the degree of circular polarization of this photoluminescence to determine the (sign of) the exciton  $g$  factor in the growth direction and the longitudinal spin relaxation time  $T_1$  of the exciton. A remarkable sign change of the degree of circular polarization as a function of excitation

density (i.e., electric field) is associated with a sign change of the  $g$  factor of the exciton of the (ensemble of) (In,Ga)As quantum dots. The longitudinal spin relaxation times  $T_1$  exhibit a power law dependence as a function of the magnetic field  $B$ , which has been theoretically predicted by Tsitsishvili *et al.* (2003). We find  $T_1 \sim B^{-2.9 \pm 0.4}$ , matching well with the theoretical prediction of  $T_1 \sim B^{-3}$  of Tsitsishvili *et al.* (2003).

Chapter 5 discusses a combined measurement of the spectrally- and time-resolved photoluminescence (PL) spectra. The PL intensity decay exhibits a non-single exponential decay, which we do not assign to a 'broadening' of radiative lifetimes due to different quantum dot sizes, since we measure at a fixed energy. Instead, we associate the non-single exponential decay to a varying radiative recombination time as a function of time, since the electric field varies in time. We correlate the electric field as a function of time, monitored by the Stark shift in time, with the variable recombination time to deduce its dependence on the electric field. Electric fields up to 200 kV/cm can enlarge the radiative recombination time by a factor 4.

Finally, chapter 6 presents time-resolved Kerr rotation measurements on the single layer of (In,Ga)As quantum dots. Besides the pulsed pump- and probe laser, an additional He:Ne laser is used to control the effective electric field over the quantum dots. Like in chapter 4, the electric field can be measured via the Stark shift in the PL spectra. When an in-plane magnetic field is applied, the signal oscillates, which can be interpreted as the precession of the spins in the (ensemble of) quantum dots. The frequency of the precession is proportional to the in-plane  $g$  factor, and the decay time of the signal can be interpreted as the spin decoherence time in the (In,Ga)As quantum dots. When the electric field over the quantum dot is increased, the in-plane  $g$  factor increases marginally.

The values presented in this thesis embody the longitudinal spin relaxation time  $T_1$  of the exciton, the spin decoherence time  $T_2^*$  of the conduction and valence electron, the radiative recombination time  $\tau_{rec}$  of the exciton, the longitudinal exciton  $g$  factor, and the in-plane valence electron  $g$  factor in quantum dots. On the latter, no experimental data did exist for un-annealed (In,Ga)As quantum dots. Finally, Stark shifts up to 40 meV, associated with electric fields up to  $F \sim 200$  kV/cm, have been observed in electroluminescence, steady-state photoluminescence and time-resolved photoluminescence spectra.





## CHAPTER 2

# Quantum dots in magnetic and electric fields

### ABSTRACT

This chapter gives an overview of the Zeeman effect in semiconductor nanostructures, in particular quantum dots. We recall some general theory of the energy levels of semiconductor structures in magnetic field, and discuss ways to approximate these effects in low-dimensional structures. The exciton  $g$  factor is introduced as a combination of the conduction and valence electron  $g$  factor. The theoretical and experimental results of growth direction  $g$  factors in quantum dots are discussed. We comment on the experimental methods to probe the  $g$  factor in the growth and in-plane direction and its restrictions. Finally, we discuss the Stark shift, induced by an electric field over quantum-confined structures, and tunneling of charge carriers out of the quantum dot.

## 2.1 Magnetic field effects in semiconductor nanostructures

A magnetic field results in a diamagnetic shift of the energy levels due to stronger localization of the spatial part of the wavefunction, and into a Zeeman energy between the spin-up and spin-down part of the wavefunction. The Zeeman energy  $\Delta_Z$  is given by Eq. 1.2 in Ch. 1. When the magnetic field  $B$  is pointing in the  $z$ -direction, the Hamiltonian reduces to  $\Delta_Z = g\mu_B S_z B$ . For a Landé  $g$  factor of 2 (i.e., the value of the electron  $g$  factor in vacuum), Zeeman energies are approximately  $100 \mu\text{eV}$  for a magnetic field of 1 T.

For a confined charge carrier (e.g., in a quantum dot), one should incorporate, besides the spin-dependent Zeeman splitting, the effect of the angular momentum of the spatial part of the wavefunction. In the case of a *weak coupling* between the spin  $\mathbf{S}$  and the angular momentum  $\mathbf{L}$ , one can sum the angular momentum and spin to write the Hamiltonian

$$H = \mu_B(g_L\mathbf{L} + g_S\mathbf{S}) \cdot \mathbf{B} \quad (2.1)$$

Such a system is fully determined by the quantum numbers  $\{L, l_z, S, s_z\}$ , where  $l_z$  and  $s_z$  describe the projection of the angular momentum and the spin on the axis of the magnetic field. The  $g$  factors  $g_L$  and  $g_S$  of the angular momentum and spin of the wavefunction have the values 1 and 2, respectively.

We measure optical transitions between the conduction and valence electron, and therefore must consider the Zeeman energies of both charge carriers. The valence electron Bloch functions in GaAs and InAs experience strong spin-orbit coupling. One has to introduce a new quantum number  $J$  for these states, where  $J = L + S$ . Equation 2.1 can be rewritten with the new quantum number  $J$ , and reads,

$$H = g_J\mu_B\mathbf{J} \cdot \mathbf{B}, \quad (2.2)$$

where we have introduced the Landé factor  $g_J$  for the coupled system. This Landé factor is a linear combination of the Landé factors for the angular momentum ( $g_L$ ) and spin ( $g_S$ ). The coupled  $g$  factor  $g_J$  is determined by the quantum numbers  $L$  and  $S$  and reads

$$g_J = g_L \frac{J(J+1) - S(S+1) + L(L+1)}{2J(J+1)} + g_S \frac{J(J+1) + S(S+1) - L(L+1)}{2J(J+1)}, \quad (2.3)$$

where  $g_L = 1$  and  $g_S = 2$ . The Zeeman energy in the strongly coupled system is determined by the quantum numbers  $\{J, J_z, L, S\}$ , and its  $g$  factor by  $\{J, L, S\}$ . The heavy and light hole states have quantum numbers  $\{J, L, S\} = \{\frac{3}{2}, 1, \frac{1}{2}\}$ , which yields  $g_J = \frac{4}{3}$ . They differ in their Zeeman energy due to a different projection of the angular

momentum, which is  $J_z = \pm\frac{3}{2}$  for the heavy-holes and  $J_z = \pm\frac{1}{2}$  for the light holes. The split-off band, which is not involved in our optical transitions, has  $\{J, L, S\} = \{\frac{1}{2}, 1, \frac{1}{2}\}$ , resulting in  $g_J = \frac{2}{3}$ . Since Eq. 2.2 contains, besides the  $g$  factor, also the projection of the angular momentum of the wavefunction on the magnetic field axis, the Zeeman energy for the heavy hole ( $J_z = \pm\frac{3}{2}$ ,  $g_J = \frac{4}{3}$ ) can still be larger than for the conduction electron ( $S_z = \pm\frac{1}{2}$ ,  $g_S = 2$ ).

Throughout this whole work, we employ the 'experimental' definition of the  $g$  factor, regardless of the (coupled) angular momentum  $J$  of the charge carrier wavefunction, which is defined as

$$g^* = \frac{E_{\uparrow} - E_{\downarrow}}{\mu_B B}, \quad (2.4)$$

where  $E_{\uparrow(\downarrow)}$  is the energy of the spin up (down) state of the conduction or valence electron. All discussions on the  $g$  factor are performed from an electron point-of-view, to avoid confusion due to the positive charge of the hole (Pryor and Flatté, 2007). Certain authors, like Babinski *et al.* (2006), use the definition where the  $g$  factor of the valence electron describes the Zeeman energy between the  $J_z = +\frac{1}{2}$  and  $J_z = -\frac{1}{2}$  angular momentum states, whereas in our definition of Eq. 2.4, it is the difference between  $J_z = +\frac{3}{2}$  and  $J_z = -\frac{3}{2}$  state. Therefore, our valence electron  $g^*$  factor is three times larger than the value used by Babinski *et al.* (2006). The  $g^*$  in Eq. 2.4 embodies also possible spin-orbit effects, and is thus called the effective  $g$  factor.

To write down the Zeeman Hamiltonian for the complete wavefunction, one should incorporate a spin-orbit term  $\mathbf{L} \cdot \mathbf{S}$  between the angular momentum and spin part of the wavefunction (Heine, 1993). For the eight most important bands ( $2 \times$  conduction,  $4 \times$  valence, and  $2 \times$  split-off band), one can write

$$H_c = \mu_B(\mathbf{L} + 2\mathbf{S}) \cdot \mathbf{B} + \lambda_c \mathbf{L} \cdot \mathbf{S} \quad (\text{Conduction electron}) \quad (2.5)$$

$$H_v = \mu_B(\mathbf{L} + \frac{4}{3}\mathbf{J}) \cdot \mathbf{B} + \lambda_v \mathbf{L} \cdot \mathbf{J} \quad (\text{Valence electron}) \quad (2.6)$$

$$H_{so} = \mu_B(\mathbf{L} + \frac{2}{3}\mathbf{J}) \cdot \mathbf{B} + \lambda_{so} \mathbf{L} \cdot \mathbf{J} \quad (\text{Split - off electron}) \quad (2.7)$$

where the  $\mathbf{L}$ 's in Eq. 2.5 – 2.7 are the angular momenta associated with the envelope part of the carrier wavefunction. The parameter  $\lambda$  describes the spin-orbit contribution to each band and depends on the geometry of the system.

Equations 2.5 – 2.7 can be written in terms of the effective  $g$  factor we have just introduced. The conduction Hamiltonian becomes  $H = g_c^* \mu_B B S_z$ , the valence electron Hamiltonian  $H = g_v^* \mu_B B \tilde{S}_z$ , and the split-off electron Hamiltonian  $H = g_{so}^* \mu_B B \tilde{S}_z$ . Note that the  $\tilde{S}_z$  indicate the (pseudo) spin projections with  $\tilde{S}_z = \pm\frac{1}{2}$ , because of our

definition of Eq. 2.4. For the *conduction* electron  $g$  factor, one can write, due to the spin-orbit effects (Roth *et al.*, 1959),

$$g_c^* = 2 - \frac{E_p \Delta_0}{3E_0(E_0 + \Delta_0)} \quad (2.8)$$

where  $E_p = \frac{2\langle S|P|X\rangle^2}{m}$  is the Kane energy (Kane, 1957, 1959; Yu and Cardona, 2001). Values for III–V semiconductors range from +0.4 for the light compounds like AlGaAs to  $-50$  for the heavy compounds like InSb. Our research is focussed on GaAs, which has a conduction electron  $g$  factor of  $-0.44$  (Oestreich and Rühle, 1995), and InAs, with a conduction electron of  $-15$ . Heavy hole  $g$  factors are  $-9$  and  $-45$  for GaAs and InAs, respectively, whereas the light holes have a  $g$  factor of  $-3$  and  $-15$  (Yu and Cardona, 2001).

In optical experiments on quantum dots, like micro-PL (abbreviated  $\mu$ -PL, i.e., the PL of a small area of the order of  $1 \mu m^2$ , typically revealing the discrete energy levels of quantum dots), one effectively probes on the  $g$  factor of both charge carriers. It is therefore convenient to introduce the  $g$  factor of the exciton. If we disregard the exchange interaction for a moment, one can write a combined  $g^*$  factor for the exciton of  $g_{exc}^* = -g_c^* + g_v^*$  for the bright optical transitions. For the exciton, a similar definition as Eq. 2.4 exists:  $g_{exc}^* = \frac{E_{\sigma+} - E_{\sigma-}}{\mu_B B}$ , where  $E_{\sigma\pm}$  is the exciton energy level which emits predominantly  $\sigma\pm$  photons.

### Landé $g$ factors in the growth direction in III-V semiconductor quantum dots

The  $g$  factor in the growth direction (i.e., the  $[100]$  direction in the crystal) of charge carriers in quantum dots depends on numerous parameters (like the shape, composition and size), which results in a large range of  $g^*$  factors. It is possible to give the range of possible  $g^*$  factors of all semiconductor structures. The Hamiltonians Eqs. 2.5 – 2.7 depend on the spin-orbit parameters  $\lambda_c$ ,  $\lambda_v$  and  $\lambda_{so}$ . In GaAs and InAs, these have a positive value (Yu and Cardona, 2001), which leads to a preferential *antiparallel alignment* of the angular momentum  $L$  and spin  $S$ . For the conduction electron, therefore, only  $g$  factors between the bulk  $g$  factor and the vacuum value of 2 occur. For the valence electron,  $g$  factors between the bulk  $g$  factor and  $g_v^* = 4$  occur, where 4 is the value for the  $g$  factor of the Bloch part of the wavefunction.

From Eqs. 2.5 – 2.7, one can read that, when the angular momentum  $\mathbf{L}$  of a state goes to zero, known as the quenching of the envelope angular momentum, the response in magnetic field is determined by the Bloch functions. The quenching of the envelope angular momentum embodies the reduced coupling between conduction and valence band, since the envelope wavefunction in the quantum dot differs strongly from the bulk

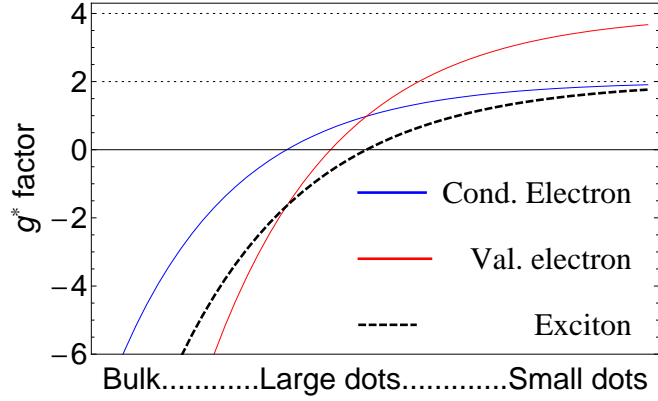


**Figure 2.1:** A schematic representation of the qualitative behavior of the effective  $g$  factor in the growth direction as a function of the confinement. The effective  $g$  factor converges to the  $g$  factor of the Bloch state when the confinement increases. The exciton  $g$  factor follows from  $g_{exc}^* = -g_c^* + g_v^*$ .

envelope wavefunction in magnetic field. The  $g$  factors of the states with a quenched envelope angular momentum are therefore determined by the  $g$  factor of the Bloch part of the wavefunction (which are  $g_c^* = 2$  and  $g_v^* = 4$  for the conduction and valence electron, respectively). It can be shown that quenching of the angular momentum occurs when spatially symmetric eigenstates (e.g.,  $p_x, p_y, p_z$ ) are nondegenerate in the potential (van Vleck, 1932).

The effect of the reduced envelope angular momentum is schematically drawn in Fig. 2.1. The  $x$  axis in this figure is a qualitative measure for the confinement level. When this is increased, the angular momentum is reduced (Pryor and Flatté, 2006), which leads to convergence of the growth direction  $g$  factor to  $g_c^* = 2$  and  $g_v^* = 4$  for the conduction electron and valence electron, respectively. The  $g_{exc}^*$  in Fig. 2.1 can be written as  $g_{exc}^* = -g_c^* + g_v^*$ .

In the theoretical literature, there have appeared several calculations on the growth direction  $g$  factor in self-assembled (In,Ga)As quantum dots, which either apply a  $\mathbf{k} \cdot \mathbf{p}$  calculation (Nakaoka *et al.*, 2004, 2005; Pryor and Flatté, 2006, 2007) or tight-binding calculation (Sheng and Babinski, 2007; Sheng, 2007). In these studies, the dependence on several parameters, like the shape, Ga content and size are investigated. One can draw several conclusions from these calculations. First of all, they indicate that the conduction electron is less sensitive to the variation in the size, shape and composition than the valence electron. Values for  $g_c^*$  range from  $-1$  to  $0$ . There is a tendency for the conduction electron  $g$  factor to increase when (i) the quantum dot contains more Ga (Nakaoka *et al.*, 2004) or when (ii) the quantum dot size gets smaller (Pryor and Flatté, 2006, 2007).

The valence electron, on the other hand, has values ranging from  $-7$  (Pryor and

Flatté, 2006, 2007) to +1 (Nakaoka *et al.*, 2004). The largest (negative) values are found in quantum dots consisting of pure InAs. The  $g_v^*$  increases with decreasing size of the quantum dot (Nakaoka *et al.*, 2004), which can be associated with the quenching of the angular momentum (see Fig. 2.1). Little effect is observed from the increase of Ga content in the dot (Nakaoka *et al.*, 2004), although this remains difficult to conclude since their presentation does not allow to extract the behavior by changing this single parameter. Sheng and Babinski (2007) show that the valence electron  $g$  factor can cross zero when the height of the quantum dot increases. Moreover, Sheng (2007) showed that the valence electron is very sensitive to the elongation (i.e., the ratio of the longest and shortest axis of the footprint) of the quantum dots.

To summarize these calculations, one can say that  $g_v^*$  occurs in a large range and is most sensitive to the *size* of the quantum dot. Therefore, the valence electron line in Fig. 2.1 immediately acts as a crude representation of the  $g_v^*$  of self-assembled (In,Ga)As quantum dots.

We note that the calculations show that there exist positive valence electron  $g$  factors (Nakaoka *et al.*, 2004). In the calculation of Nakaoka *et al.* (2004), a positive  $g$  factor for the valence electron is found for quantum dots with large Ga content, diameter sizes in the range of 10 nm, and a truncated pyramid shape. The PL emission of such quantum dots occurs in the energy range from 1.25 eV to 1.30 eV.

## **Experimental methods to determine the $g$ factor in the growth direction in quantum dots**

One can determine the  $g$  factor in the growth direction most accurately by  $\mu$ -PL measurements, where one should apply a Faraday geometry. An extraction of the growth direction  $g$  factor can also be done from the method we present in this work, which is a macro-PL measurement, and from electrical measurements like C-V spectroscopy (Medeiros-Ribiero *et al.*, 2003; Hanson *et al.*, 2003; Björk *et al.*, 2005; Reuter *et al.*, 2005). In 2007, two 'new' methods have appeared, which employ linear dichroism rotation spectroscopy (Yugova *et al.*, 2007) and dynamic nuclear spin polarization (Tartakovskii *et al.*, 2007; Kaji *et al.*, 2007). For the  $g$  factor determination by a macro-PL measurement, one does need the spin relaxation time and radiative relaxation time as extra input parameters.

From electrical measurements, it is hard to distinguish the sign of the growth direction  $g$  factor (which is relatively easy determined from the polarization in optical measurements). The possibility to discriminate between the conduction and valence electron  $g$  factor, however, is an advantage in electrical measurements (Medeiros-Ribiero

**Table 2.1:** Effective  $g$  factors  $g_v^*$ ,  $g_c^*$  and  $g_{exc}^*$  in the growth direction, determined from optical experiments in a Faraday geometry, for (In,Ga)As, (In,Al)As and (Al,Ga)As quantum dots. The *red. strain* refers to an additional strain reducing layer in the quantum dot growth (Nakaoka *et al.*, 2005).

Author (Year)	Material	$g_v^*$	$g_c^*$	$g_{exc}^*$
Bayer <i>et al.</i> (1995)	(In,Ga)As			$ g_{exc}^* =2$
Bockelmann <i>et al.</i> (1997)	(Al,Ga)As			(0.7,2)
Kuther <i>et al.</i> (1998)	(In,Ga)As			-3.02
Toda <i>et al.</i> (1998)	(In,Ga)As			$ g_{exc}^* =(1.21,1.73)$
Bayer <i>et al.</i> (1999)	(In,Ga)As	-2.21	-0.81	-3.02
Goni <i>et al.</i> (2000)	(In,Ga)As, <i>annealed</i>			(-0.7,-0.3)
Kotlyar <i>et al.</i> (2001)	In <sub>0.1</sub> Ga <sub>0.9</sub> As, <i>etched</i>			-6
Finley <i>et al.</i> (2002)	(In,Ga,Al)As			$ g_{exc}^* =2.25$
Nakaoka <i>et al.</i> (2004)	(In,Ga)As			(-2.5,-2)
Nakaoka <i>et al.</i> (2005)	(In,Ga)As, <i>red. strain</i>			-1
Mensing <i>et al.</i> (2006)	(In,Ga)As			(-0.4,0)
Babinski <i>et al.</i> (2006)	(In,Ga)As			$ g_{exc}^*  < 0.8$
Yugova <i>et al.</i> (2007)	(In,Ga)As			$ g_{exc}^*  = 0.16$
Kaji <i>et al.</i> (2007)	(In,Al)As	$ g_v^* =2.54$	-0.37	

*et al.*, 2003; Reuter *et al.*, 2005). It is possible to distinguish between conduction and valence electron  $g$  factor by optical measurements (Bayer *et al.*, 1999), but this requires a cumbersome method and a search for specific peaks<sup>†</sup> in the spectrum. The method of Kaji *et al.* (2007), employing dynamic nuclear polarization, also allows to distinguish between  $g_c^*$  and  $g_v^*$ .

Table 2.1 shows values of exciton  $g$  factors from optical measurements. One should note that a large range of  $g_{exc}^*$  has been observed. Bayer *et al.* (1995) specifically notes that both positive and negative  $g_{exc}^*$  can be observed among quantum dots. Measurements on AlGaAs structures have a positive  $g$  factor (Bockelmann *et al.*, 1997), which could be expected from the reduced spin-orbit contributions due to incorporation of Al. Most of the other authors find a negative values for  $g_{exc}^*$ . Recently, measurements on quantum dots with a large Ga content showed a  $g_{exc}^*$  factor close to zero (Mensing *et al.*, 2006), which matches with the theoretical trend. All absolute values for the exciton  $g_{exc}^*$  factor of self-assembled quantum dots are smaller than 3.

Small  $g$  factors in the growth direction ( $|g_{exc}^*| < 0.5$ ) were observed in linear dichroism rotation spectroscopy measurements (Yugova *et al.*, 2007), as well as  $\mu$ -PL measurements (Mensing *et al.*, 2006; Babinski *et al.*, 2006). Each of these authors associate this with

<sup>†</sup>This should be peaks for optical states which are partially intermixed with dark excitons. From their behavior in magnetic field one can distinguish between a conduction and valence electron  $g$  factor.



an increased size of the quantum dot, together with increased Ga content due to an annealing procedure. Recent calculations of J.A.S.F. Pingenot and M.E. Flatté also indicate relatively small  $g$  factors for large (In,Ga)As quantum dots with 50% Ga.

### **Experimental methods to determine the *in-plane* $g$ factor in quantum dots**

Considerably less literature is available on the in-plane  $g$  factors in self-assembled quantum dots. Among the most applied methods are the time-resolved Kerr/Faraday rotation technique (for colloidal quantum dots: Gupta *et al.* (1999), for (In,Ga)P quantum dots: Kanno and Masumoto (2006), for (In,Ga)As quantum dots: Greilich *et al.* (2006b); Yugova *et al.* (2007)) and Hanle depolarization measurements (Epstein *et al.*, 2001; Masumoto *et al.*, 2006). Generally speaking, the values for the in-plane  $g$  factor are much smaller than the  $g$  factor in the growth direction. The in-plane  $g$  factor ranges from 0.1 (Dutt *et al.*, 2005) to  $\sim 0.6$  (Greilich *et al.*, 2006b; Yugova *et al.*, 2007) for the conduction electron in (In,Ga)As quantum dots. In chapter 6, we present the first results on the in-plane  $g$  factor of the valence electron, presumably, in (In,Ga)As quantum dots.

## 2.2 Electric field effects in semiconductor nanostructures

Two main electric field effects occur for the localized carrier wavefunctions in quantum dots. First of all, the electric field leads to a quantum-confined Stark shift for the energy levels of the states. Secondly, at high electric fields, carriers can tunnel out of the quantum dot.

The quantum-confined Stark effect in quantum dots consists of a linear and quadratic term with the electric field. The linear term arises from the built-in dipole in the quantum dot, which is constituted by the electron-hole pair. The quadratic term arises from a perturbation calculation on the state. The complete quantum-confined Stark shift  $\Delta_S$  can be described by

$$\Delta_S = \beta F^2 + \mathbf{p} \cdot \mathbf{F}, \quad (2.9)$$

where  $\beta$  describes the polarizability and  $\mathbf{p}$  the built-in electric dipole. Note that the orientation of the dipole, which can either be directed from base-to-apex or from apex-to-base in the quantum dot<sup>†</sup>, has a significant influence on the response of the state in an electric field. Due to the symmetry of the potential, the dipole is generally aligned (either parallel or anti-parallel) along the growth direction, which in our case matches with the electric field direction. We can therefore simplify Eq. 2.9 to  $\Delta_S = \beta F^2 + pF$ , where  $p$  is the scalar value of the built-in dipole.

Several observations of the polarizability  $\beta$  and the built-in dipole  $p$  have been gathered in Tab. 2.2. Only Hsu *et al.* (2001) state a value for  $\beta$  in their work. The values for  $p$  ranges from 0 to 8 eÅ. According to these parameters, the Stark shifts for quantum dots at an electric field of 100 kV/cm appear in the range 10 ~ 30 meV. We find Stark

---

<sup>†</sup>There is no full consistency in the observations of the orientation of the built-in electric dipole. Most of the observations (Fry *et al.*, 2000b; Hsu *et al.*, 2001) reveal an orientation where the hole is found at the apex of the quantum dot. However, observations of an oppositely oriented dipole (Jin *et al.*, 2004) also exist, which is also observed in our measurements. The variation can be explained by the strong dependence of the dipole on the In gradient within the quantum dot.

**Table 2.2:** Experimental values for the built-in dipole  $p$  and the polarizability  $\beta$  of the exciton ground state in self-assembled (In,Ga)As quantum dots. The abbreviations ER and PC mean electroreflectance and photocurrent spectroscopy, respectively, whereas  $\mu$ -EL stands for micro-electroluminescence.

Author (Year)	Method	$\beta$ ( $10^{-4}\text{meV}/(\text{kV}/\text{cm})^2$ )	$p$ (eÅ)
Itskevich <i>et al.</i> (2000)	$\mu$ -EL		$3.5 \pm 1$
Fry <i>et al.</i> (2000b)	PC		$4 \pm 1$
Hsu <i>et al.</i> (2001)	ER, PC, PL	$5.5 \pm 0.5$	$6.2 \pm 1.3$
Jin <i>et al.</i> (2004)	ER		-4
Finley <i>et al.</i> (2004)	$\mu$ -PL		$0 < p < 8$

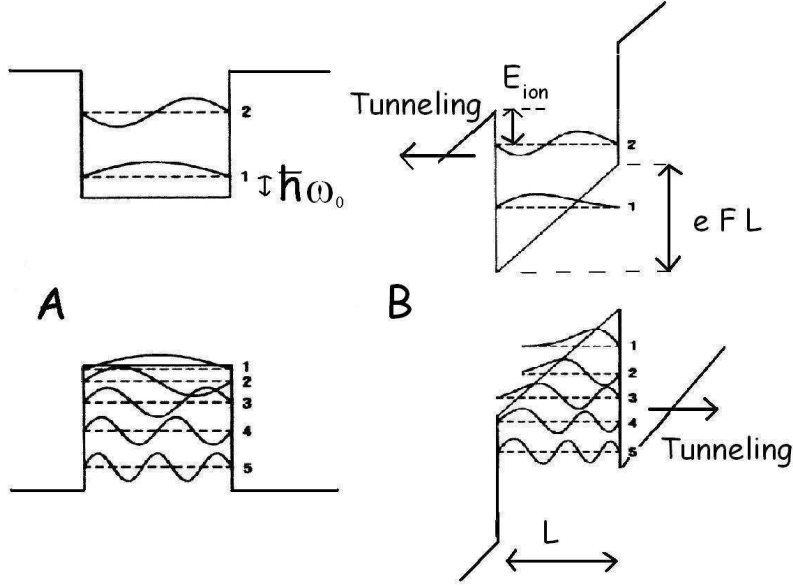


**Figure 2.2:** A schematic picture of the energy levels in a quantum well (dot) with width (height)  $L$ , both without (Fig. A) and with (Fig. B) electric field. A comparison between the parameter  $eFL$  (Fig. B) and the confinement energy  $\hbar\omega_0$  (i.e., difference between the bottom of the band and energy of a state, shown in Fig. A), can be an important parameter to determine whether the wavefunction is strongly deformed or not. This is an edited figure from Miller *et al.* (1986).

shifts  $\Delta_S \sim 40$  meV for electric fields  $F \sim 200$  kV/cm. Such values have also been calculated by Wang *et al.* (2006) for (In,Ga)As quantum dots of different shapes and In-Ga compositions. Similar values for the Stark shift have been observed in quantum well structures (Miller *et al.*, 1984, 1985, 1986), as well as in CdSe nanocrystallite quantum dots (Empedocles and Bawendi, 1997).

Figure 2.2 shows the lowering of the energy levels of the carriers in a quantum well. An important parameter in this process is  $eFL$ , which describes the energy drop along the growth direction over a distance  $L$ , the height of the quantum dot or the width of the quantum well. This energy can be compared with the confinement energy,  $\hbar\omega_0$ , which has the largest contribution from the confinement in the growth direction. When the energy associated with the confinement is smaller than  $eFL$ , the confinement height is affected, which deforms the carrier wavefunction. This could also be a situation at which the  $g$  factor of the carrier wavefunction is strongly affected.

Tunneling through the barrier (see Fig. 2.2) occurs for charge carriers in a quantum well or quantum dot subjected to high electric fields. The tunneling process can be monitored either by photoluminescence (Fry *et al.*, 2000a) or photocurrent measurements (Chang *et al.*, 2000). Experimental studies of Fry *et al.* (2000a) and Finley *et al.* (2004) indicate that photoluminescence quenches (due to tunneling) between 120 kV/cm and

150 kV/cm. The escape rate  $\tau_{tunnel}^{-1}$  from a quantum dot can be approximated by (Fry *et al.*, 2000a)

$$\tau_{tunnel}^{-1} = \frac{\hbar\pi}{2m^*L^2} \exp\left(-\frac{4}{3} \frac{\sqrt{2m^*E_{ion}^3(F)}}{e\hbar F}\right) \quad (2.10)$$

where  $m^*$  is the effective mass of the charge carrier and  $E_{ion}(F)$  is the ionization energy of the carrier, which is a function of the electric field  $F$ . In the case of an electric field, the energy levels lower their electric field due to a Stark shift (see Eq. 2.9), but the depth of the potential well can also be slightly reduced by the electric field. It is therefore hard to find an approximation for the function  $E_{ion}(F)$ . Most authors (Fry *et al.*, 2000a; Oulton *et al.*, 2002) assume a constant dependence. Equation 2.10 indicates that, under equal circumstances for the conduction and valence electron, conduction electrons start to tunnel at lower electric fields, due to their smaller effective mass. Kuo and Chang (2000) and Larkin and Vagov (2003) have presented more detailed studies on tunneling effects in quantum dots.



## CHAPTER 3

# Experimental techniques & sample

### ABSTRACT

In this research, we have used magneto-optical photoluminescence, micro-photoluminescence ( $\mu$ -PL), time-resolved photoluminescence and time-resolved Kerr rotation spectroscopy as techniques, which each require a setup. The magneto-optical setup was used to measure the degree of circular polarization of photoluminescence, which is utilized to determine the spin relaxation time and sign of the growth direction  $g$  factor of the exciton. Radiative recombination times of the electron-hole pairs in quantum dots were determined by the time-resolved PL setup. We give arguments for an omission of a deconvolution procedure with the instrument response function of the detector in the time-resolved PL setup. The  $\mu$ -PL setup was used to measure the  $g$  factors of single quantum dots in the Faraday geometry, whereas the Kerr rotation setup was allowed us to obtain the spin decoherence time and in-plane  $g$  factor of (an ensemble of) the quantum dots. In the final section, we discuss the growth of the sample and its electrical characterization.

### 3.1 Magneto-optical setup

This setup contains a superconducting magnet which can generate magnetic fields up to 7 T. The sample is mounted in a Helium bath, which can be evacuated to reach temperatures of 2 K. A complete scheme of the setup is shown in Fig. 3.1. We use a continuous wave Ti:Sapphire laser for the excitation. A diffraction limit of  $40\ \mu\text{m}$  for the excitation spot was determined for a laser beam diameter of  $\sim 1\ \text{cm}$  and focal distance of 40 cm of the last lens. The geometry of the lenses is such that one fiftieth of the PL emission reaches the monochromator. Note that for a spot diameter of  $100\ \mu\text{m}^2$  and quantum dot surface density  $10^{10}\text{cm}^{-2}$ , we probe  $\sim 3 \times 10^6$  quantum dots.

We employ a double-stage monochromator to spectrally resolve the luminescence with a maximum resolution of  $\sim 0.08\ \text{nm}$  at a slit width of  $100\ \mu\text{m}$ . The highest resolutions are, however, not exploited in our polarization measurements, since we perform macro-PL measurements on this setup.

The detection on the double-stage monochromator is done by a water-cooled InGaAs photomultiplier tube (PMT) in the photon counting mode, which has an increasing quantum efficiency from 0.3% to 1% in the energy range from 1.24 eV to 1.38 eV. The dark count rate of the PMT is approximately 20 counts per second throughout all measurements. The response time of the PMT on a photon detection event is  $\sim 3\ \text{ns}$ , which is negligible compared to the counting time period of the dual-gate counter ( $> 1\ \mu\text{s}$ ). For the simultaneous measurements of the Stark shift and the polarization, an additional single-stage monochromator with a Si-CCD camera was used. A beam splitter was put in the detection track to distribute the signal to both monochromators.

To perform measurements on the degree of circular polarization in real-time, we use a photo-elastic modulator, denoted by PEM, together with a linear polarizer. The

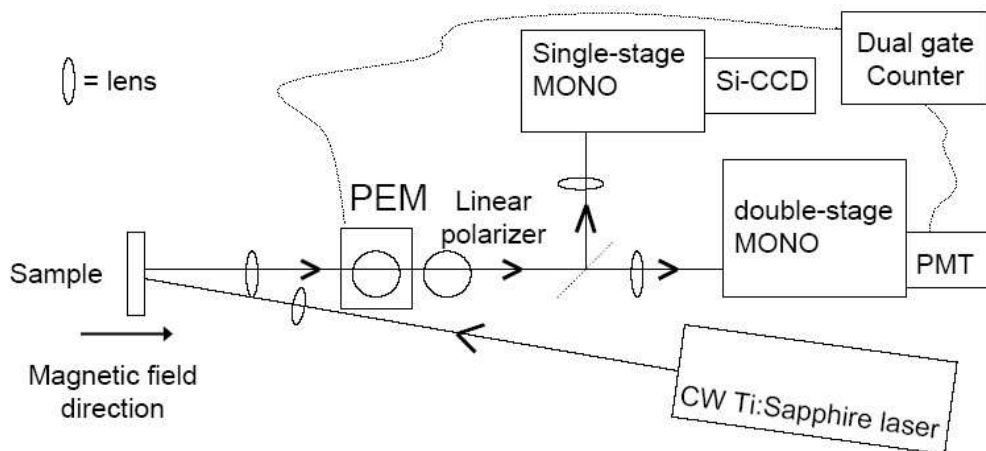


**Figure 3.1:** A scheme of the magneto-optical setup.

photons are counted by the PMT for these measurements. The active axis of the linear polarizer is oriented at an angle of  $45^\circ$  with the slit and grating of the monochromator. The PEM consists of a silica crystal operating at its eigenfrequency of 42 kHz, and induces a phase difference  $\phi(t) = A_0 \sin(\omega t)$  along the active axis (where  $2\pi\omega = 42\text{kHz}$ , corresponding with a period of  $23.9 \mu\text{s}$ ). For the measurements on the degree of circular polarization in Ch. 4, we employ a maximum phase difference of  $A_0 = \frac{\pi}{2}$ , corresponding to the action of a  $\pm\lambda/4$  plate at the maximal compression/extraction of the PEM. When passing the PEM, linearly polarized light is alternately turned into  $\sigma+$  and  $\sigma-$  light. Equivalently, circularly polarized light is turned into linearly polarized light. The PEM module gives an electrical trigger to a home-built dual-gate counting module at the PEM frequency. The temporal resolution of the counting module is  $0.1 \mu\text{s}$ .

To determine the spin relaxation times and monitor the  $g$  factors in the quantum dots in Ch. 4, we measure the degree of circular polarization. After passing the PEM, the circularly polarized light is turned into linearly polarized light of alternating direction. The linear polarizer, placed behind the PEM, is transparent for only one type of linear polarization. The dual-gate counter opens its counting bins exactly synchronously with the  $+\lambda/4$  and  $-\lambda/4$  action of the PEM, thereby counting the photons with opposite circular helicity in the separate bins.

### Temporal calibration of the PEM

For a proper timing of the counting windows of the dual-gate counter, we have to determine at what time *after* the electrical trigger pulse from the PEM module, the crystal acts as a  $\lambda/4$  or  $-\lambda/4$  plate.

As a first experiment, we determine the points where the PEM does not modulate the signal. This can be determined in a setup shown schematically in Fig. 3.2A. In this alignment, two crossed linear polarizers have their axis orthogonally oriented, and the PEM crystal is placed in between them. We apply a maximum phase shift of  $A_0 = \frac{\pi}{2}$ . If there would be no PEM crystal, transmission of light would be blocked. Figure 3.2B shows the signal intensity as we vary the position of a window of  $0.5 \mu\text{s}$  throughout the whole cycle time of  $23.9 \mu\text{s}$ . The curves for three different wavelengths show a minimum at  $8\text{-}8.5 \mu\text{s}$  and  $20.5 \mu\text{s}$ , which correspond to the times where the PEM does *not* modulate the light. The PEM thus acts as a  $\pm\lambda/4$  plate at  $2.5 \mu\text{s}$  and  $14 \mu\text{s}$ .

In the second experiment, we check the efficiency of the detection of the polarization, by a setup displayed in Fig. 3.3A. We perform this experiment to determine which counting window width we should apply. This setup is similar as in Fig. 3.2A, but now with an extra  $\lambda/4$  plate in front of the PEM. The axis of the  $\lambda/4$  is at the same angle as the active axis of the PEM. The linearly polarized light, described by  $\frac{1}{\sqrt{2}}(|X\rangle + |Y\rangle)$



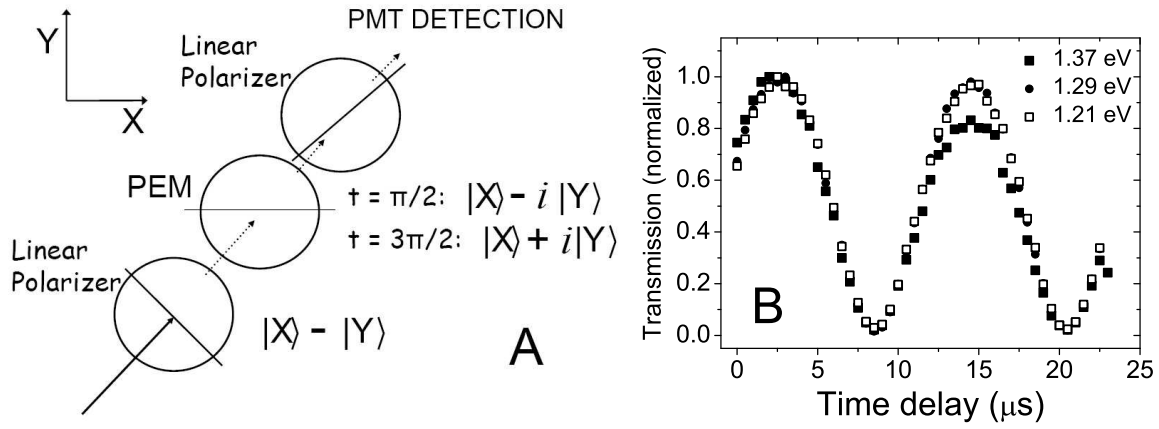


**Figure 3.2:** Figure A shows the scheme which can be used to determine when the light is passing unmodulated. The transmission data at several energies, shown in Fig. B, reveal that this occurs at  $t = 8 - 8.5 \mu\text{s}$  and  $t = 20.5 \mu\text{s}$  after the electrical trigger.

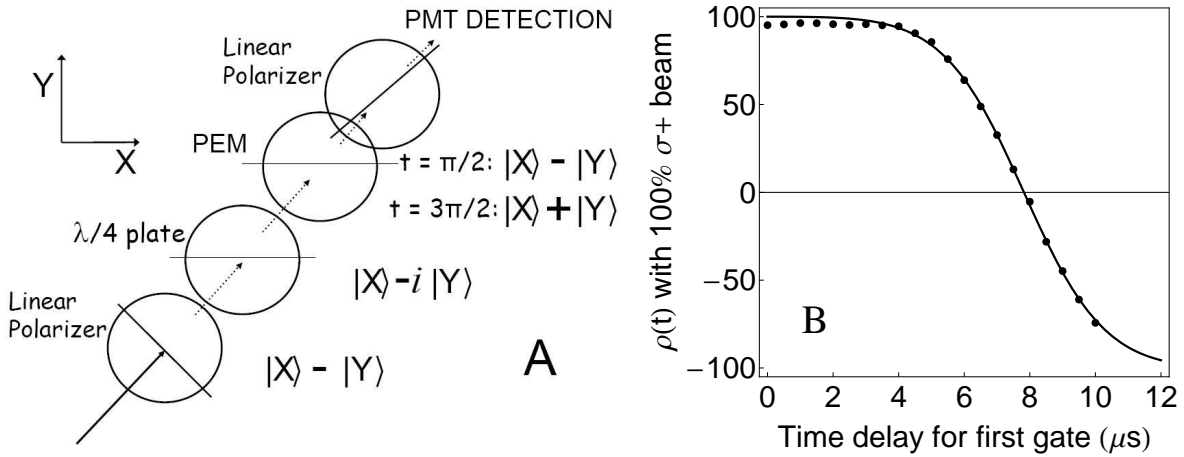


**Figure 3.3:** In this setup (Fig. A), we measure the polarization of a 100% circularly polarized beam as a function of the positioning of two narrow windows ( $0.5 \mu\text{s}$ ) separated half the PEM cycle period ( $11.9 \mu\text{s}$ ). Figure B shows that efficiencies over 95% were found at times from  $0 \mu\text{s}$  up to  $4.5 \mu\text{s}$ . The solid line in Fig. B is prescribed by Eq. 3.1.

in Fig. 3.3A, becomes circularly polarized light when passing the  $\lambda/4$  plate, described by  $\frac{1}{\sqrt{2}}(|X\rangle + i|Y\rangle)$ . When the circularly polarized light hits the PEM, and the PEM acts as a  $+\lambda/4$  ( $-\lambda/4$ ) plate, the polarization aligns with the probing linear polarizer at  $|X\rangle + |Y\rangle$  ( $|X\rangle - |Y\rangle$ ). The signal intensity is therefore alternately blocked and unblocked.

To interpret the calibration results, we exercise the property that the transmission  $T$  is proportional to  $\cos(\alpha)^2$  for a polarization vector at  $\alpha^\circ$ . For the PEM-modulated signal, the transmission  $T$  of a 100% circularly polarized beam can therefore be approximated by  $T_{\sigma_+}(t) \sim \cos^2(\frac{\pi}{2} \sin(\omega t))$ , since the phase difference induced by the PEM is  $\phi(t) = \frac{\pi}{2} \sin(\omega t)$ . If we would enter with 100% polarized beam of the opposite circular polarization, the transmission would follow  $T_{\sigma_-}(t) \sim \cos^2(\frac{\pi}{2} \sin(\omega t + \frac{\pi}{2}))$ .

Figure 3.3B presents the *degree* of circular polarization  $\rho(t)$  from two narrow windows with width  $0.5 \mu\text{s}$ , separated by half the cycle period ( $11.9 \mu\text{s}$ ). The variable on the  $x$  axis denotes the time after the PEM trigger pulse at which the *first* counting gate opens. Since we enter with a 100% circularly polarized light beam, we expect a probed polarization of 100% at the times where the PEM acts as a  $\pm\lambda/4$  plate. From the transmission of the  $\sigma_+$  and  $\sigma_-$  photons, we can now write

$$\rho(t) = \frac{T_{\sigma_+}(t) - T_{\sigma_-}(t)}{T_{\sigma_+}(t) + T_{\sigma_-}(t)} = \frac{\cos^2(\frac{\pi}{2} \sin(\omega t)) - \cos^2(\frac{\pi}{2} \sin(\omega t + \frac{\pi}{2}))}{\cos^2(\frac{\pi}{2} \sin(\omega t)) + \cos^2(\frac{\pi}{2} \sin(\omega t + \frac{\pi}{2}))}. \quad (3.1)$$

The line in Fig. 3.3B is a plot of Eq. 3.1 (with  $\omega \sim 46 \text{ kHz}/2\pi$  and an extra phase difference of  $\Delta\phi = 0.063$  at  $t = 0$ ). Almost a perfect overlap exists between the predicted and measured data. We observe polarization exceeding 95% in the range from  $0 \mu\text{s}$  to  $4.5 \mu\text{s}$ , which allows us to use relatively wide counting windows without correcting the signal afterwards. Based on Fig. 3.3B, we use a counting window width of  $4.5 \mu\text{s}$ , positioned at  $0 \mu\text{s}$  and at  $12 \mu\text{s}$ . No corrections are made for the deviation from 100% within the windows.

### Sign of the exciton g-factor

The *sign* of the degree of circular polarization is calibrated using a (static)  $\lambda/4$  plate, the PEM and two linear polarizers. With a linear polarizer and  $\lambda/4$  plate, we can create light with a known circularity, specified by the manufacturer. The PEM and the linear polarizer for the detection are placed such that a beam of predominantly  $\sigma_+$  photons generates a positive polarization.

One should further note that the magnetic fields in this work are pointing into the direction of the detection track, which is shown in Fig. 3.1. Since one knows both the direction of the magnetic field and the dominating circularity of the luminescence,

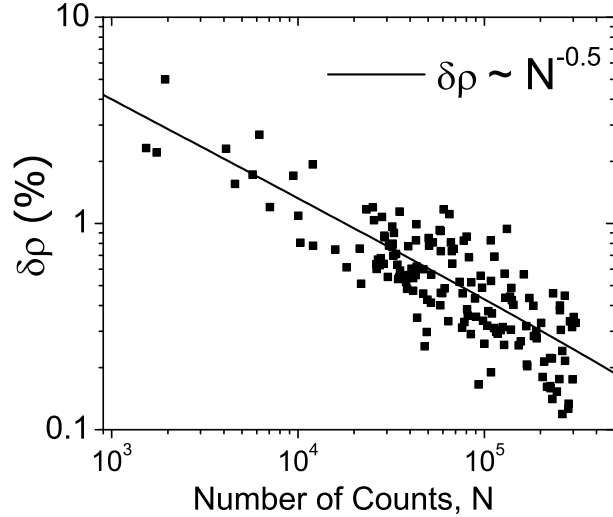


**Figure 3.4:** The standard deviation of data with small polarizations ( $\rho \lesssim 10\%$ ) as a function of the number of counts  $N$ . The data shows a behavior  $\delta\rho \sim N^{-0.5}$ , which matches the prediction in Eq. 3.4.

one can determine the sign of the  $g$  factor. In Ch. 2, we associated a positive  $g$ -factor with predominantly  $\sigma$ - photons (if the magnetic field direction and photon propagation direction are pointing in the same direction). Since there is a one-to-one relation between the predominant polarization of the photons and the sign of the degree of circular polarization, we can conclude that a positive (negative) degree of circular polarization corresponds to a negative (positive)  $g$  factor of the exciton.

## Errors

An error in the degree of circular polarization,  $\delta\rho$ , should be incorporated due to statistical nature of the detection by the photomultiplier. The detection of photons in the beam follows a Poisson distribution, which is characterized by  $p(k, \lambda) = \frac{1}{k!} \lambda^k e^{-\lambda}$ , where  $p(k, \lambda)$  is the change for a discrete event to occur  $k$  times, given a mean  $\lambda$  for the system. The Poisson distribution has a standard deviation of  $\sqrt{\lambda}$ , which we employ to derive the error arising due to the detection system.

To consider the error in the polarization, we write

$$\frac{\delta\rho}{\rho} = \frac{\delta(N_+ - N_-)}{N_+ - N_-} + \frac{\delta(N_+ + N_-)}{N_+ + N_-}, \quad (3.2)$$

which is the regular summation of relative errors in the case of division. We consider small polarizations, since these are observed in our measurements. In that case, the condition  $(N_+ - N_-) \ll (N_+ + N_-)$  holds, equivalent to  $N_+ \sim N_- \sim N$ . Without loss

of generality, we assume that  $N_+ > N_-$ . If one neglects the second term in Eq. 3.2, one can write

$$\begin{aligned}\frac{\delta\rho}{\rho} &\simeq \frac{\delta(N_+ - N_-)}{N_+ - N_-}, \\ \frac{\delta\rho}{\rho} &\simeq \frac{2\delta N}{\Delta N},\end{aligned}\tag{3.3}$$

where  $\Delta N = N_+ - N_-$  and  $\delta N = \delta N_+ = \delta N_-$ . Since the statistics follow a Poisson distribution, the error  $\delta N$  can be written as  $\delta N = \sqrt{N}$ . Therefore, one can write the absolute error in the polarization,  $\delta\rho$ , as

$$\delta\rho \simeq \frac{2\delta N}{\Delta N}\rho \simeq \frac{2\delta N}{\Delta N} \frac{\Delta N}{2N} \simeq N^{-0.5},\tag{3.4}$$

which is independent of  $\Delta N$ . The behavior of Eq. 3.4 was checked by the standard deviation of data with small polarizations ( $\rho \lesssim 10\%$ ) as a function of the count rate, presented in Fig. 3.4. A fitting procedure with a power law function,  $\sim N^m$ , resulted in  $m = -0.5$ , matching with the prediction in Eq. 3.4. Figure 3.4 and Eq. 3.4 show that one requires  $10^4$  counts to achieve an error below 1%. Most of our data of the degree of circular polarization was obtained with  $\sim 10^5$  counts, leading to errors below 1%. However, some of the data of the degree of circular polarization in Ch. 4 could not be obtained with a total count number of  $\sim 10^5$ , which resulted in larger errors.

### Micro-photoluminescence setup

In addition to the magneto-optical setup for macro-PL, we have a  $\mu$ -PL setup at our disposal. The  $\mu$ -PL setup can be used for an exact determination of the exciton  $g$  factors of individual quantum dots. Figure 3.5 shows an example of a spectrum, where a degenerate pair of levels is split up by the Zeeman energy. The  $\mu$ -PL setup can generate magnetic fields up to 5 T. Contrary to the bath-type setup we described before, the sample in this setup is mounted on a cold finger. Excitation is done by a He:Ne or continuous wave Ti:Sapphire laser, where the excitation beam is focussed through a 50x or 100x objective. The laser spot can be focussed to an area of  $\sim 1 \mu\text{m}^2$ , thereby crudely defining the spatial resolution without additional masking. We use a triple-stage monochromator and a Si-CCD camera to resolve and detect the PL.

Depending on the density of the quantum dots in the sample, it might be necessary to deposit additional masking on the top of the sample. We used circular masks with a diameter of  $2 \mu\text{m}$ ,  $1 \mu\text{m}$ ,  $800 \text{ nm}$  and  $400 \text{ nm}$ . It was possible to perform  $\mu$ -PL measurements with all mask diameters.

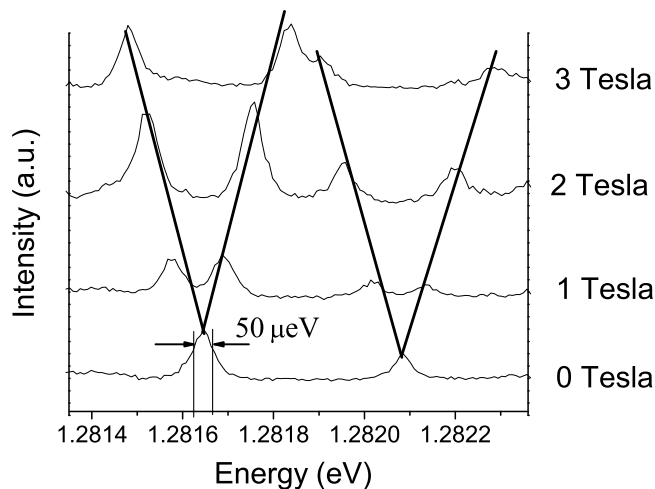


**Figure 3.5:** The  $\mu$ -PL setup can be used to determine the exciton  $g$  factor very accurately. This figure shows  $\mu$ -PL spectra with an increasing Zeeman energy with increasing magnetic field. The spectra in this figure were measured on a sample with equivalent quantum dots as the main sample of this thesis. The sample structure, however, did not contain a built-in electric field.

### 3.2 Time-resolved Photoluminescence setup

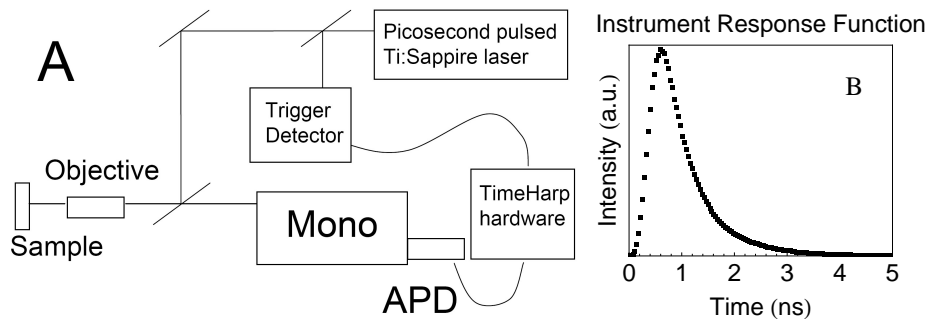
Figure 3.6A shows the scheme of the time-resolved setup, which consists of a sample on a micropositioner, a 50 x or 100 x objective, a monochromator and detector. We use a picosecond-pulsed excitation laser with a repetition rate of 76 Mhz, a single stage 0.5 m monochromator, and an avalanche photodiode (APD) detector. Additional hardware is used to record the arrival times of the photons, which electronics has a maximum resolution of 37 ps.

Figure 3.6B shows the instrument response function (IRF) of the APD, which is the response of the APD to a laser pulse. The IRF has a full width at half maximum of  $\sim 600$  ps and has a rather symmetric shape. The observed decay is convoluted with the IRF of the detector. The signal can therefore be described by  $F(t) \sim \int_0^t f(\tau)IRF(t-\tau)d\tau$ , where  $F(t)$  is the measured (convoluted) signal and  $f(t)$  is the actual intensity decay of the quantum dots. Since our measured signal is convoluted, it needs to be deconvoluted to determine  $f(t)$ .

We did *not* apply a deconvolution procedure, because the quality of the signal (i.e., the signal-to-noise ratio) is strongly reduced by the deconvolution procedure. In chapter 5, we analyze the variable decay rates of time-resolved photoluminescence. These variable decay rates are interpreted as a temporarily varying recombination time. The recombination time is determined from the derivative of the natural logarithm of the intensity (since the intensity decay is described by  $I(t) \sim e^{-t/\tau_{rec}}$ ). To investigate whether the omission of the deconvolution procedure is permitted, we investigate the *ratio of the derivatives* of the of an unconvoluted and convoluted signal:

$$\mathcal{D}(t) = \frac{\ln(f(t))'}{\ln(F(t))'} = \left( \frac{f'(t)}{f(t)} \right) \left( \frac{\int_0^t f(\tau)IRF(t-\tau)d\tau}{\int_0^t f(\tau)IRF'(t-\tau)d\tau} \right), \quad (3.5)$$

where we have employed that  $IRF(0) = 0$ . In fact, the function  $\mathcal{D}(t)$  represents the



**Figure 3.6:** Figure A shows the scheme of the time-resolved setup. Figure B shows the instrument response function of the APD.

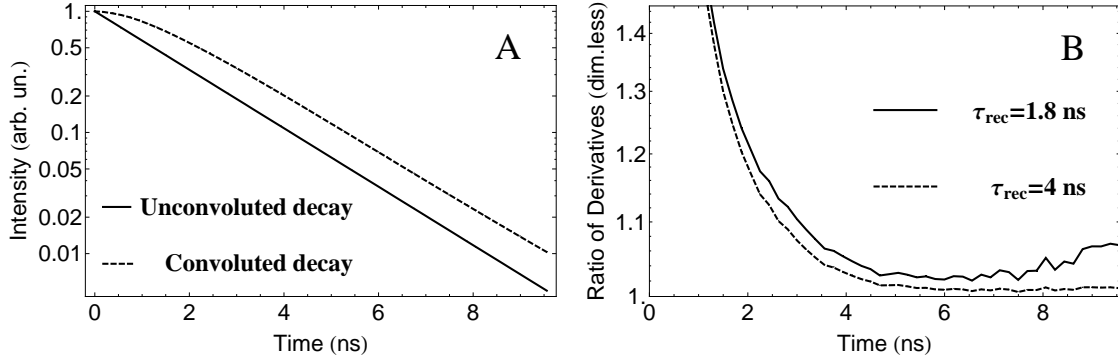


**Figure 3.7:** Figure A shows the calculated unconvoluted ( $f(t)$ ) and convoluted ( $F(t)$ ) intensity decay of a signal with  $\tau_{rec} = 1.8$  ns on a logarithmic scale. Figure B shows the function  $\mathcal{D}(t)$  of Eq. 3.5 of both decays, for  $\tau_{rec} = 1.8$  ns and  $\tau_{rec} = 4.0$  ns. Significant errors arise only before 2 ns.

ratio of the measured and actual recombination times in time. Note that  $\mathcal{D}(t)$  a function of the recombination time  $\tau_{rec}$  (not written in Eq. 3.5).

Figure 3.7A shows the (calculated) convoluted and unconvoluted decay for a recombination time of 1.8 ns, where we have employed the *measured* IRF for the convolution. The derivatives of both functions appear rather constant and similar, except in the range from 0 to 2 ns. Figure 3.7B shows the function  $\mathcal{D}(t)$  of Eq. 3.5 as a function of time for the recombination times of 1.8 ns and 4.0 ns (which is the typical range of recombination times we will encounter). Since the measured IRF function is involved, one observes an increased signal-to-noise ratio near  $t = 8$  ns. The differences are below 20% after 2 ns. Since larger deviations occur before 2 ns, these derivatives are *not* incorporated in the analysis of the decay rates in Ch. 5.

### 3.3 Time-resolved Kerr rotation setup

The orientation of the spins of electrons in quantum dots can be monitored by measuring the Kerr rotation, which is based on a change in reflection coefficient for right- and left-handed circularly polarized light.

#### Introduction Kerr rotation

Linearly polarized light can be described as a superposition of two circularly polarized beams. The Kerr effect occurs when these circularly polarized components have a different reflection coefficient. We introduce the complex Fresnel reflection coefficient, written as  $\tilde{r}_+ = r_+ e^{i\Phi_+}$  and  $\tilde{r}_- = r_- e^{i\Phi_-}$  for  $\sigma+$  and  $\sigma-$  light, respectively, to introduce the two components of the Kerr effect:

- the Kerr rotation ( $\theta_K$ ), which rotates the linear polarization of the incoming beam with an angle. This rotation can be written in terms of the complex phase shift of the Fresnel coefficients:  $\theta_K = \frac{1}{2}(\phi_+ - \phi_-)$ .
- the Kerr ellipticity ( $\eta_K$ ), which arises due to a difference in amplitude of both reflection coefficients and causes ellipticity. The ellipticity is described as  $\eta_K = \frac{r_+ - r_-}{r_+ + r_-}$ .

As a next step, we derive the values for  $\theta_K$  and  $\eta_K$  from the dielectric tensor of a material,  $\vec{\epsilon}$ , consisting of the elements  $\epsilon_{ij}$  ( $i, j = x, y, z$ ). We assume the material to be invariant for rotations around the  $z$  axis, which leads to  $\epsilon_{xx} = \epsilon_{yy}$  and  $\epsilon_{xy} = -\epsilon_{yx}$ . Moreover, we assume a polar geometry, where the magnetization (of the spins) is directed orthogonal to the sample plane. In that case, the off-diagonal elements  $\epsilon_{xz}$ ,  $\epsilon_{yz}$ ,  $\epsilon_{zx}$  and  $\epsilon_{zy}$  of the dielectric tensor of the material are zero. The dielectric tensor  $\vec{\epsilon}$  can be written as

$$\vec{\epsilon} = \begin{pmatrix} \epsilon_{xx} & \epsilon_{xy} & 0 \\ -\epsilon_{xy} & \epsilon_{yy} & 0 \\ 0 & 0 & \epsilon_{zz} \end{pmatrix}. \quad (3.6)$$

In a polar geometry, the Fresnel reflection coefficients  $\tilde{r}_\pm$  can be expressed in terms of the complex index of refraction  $n_\pm$  for circularly polarized light by  $\tilde{r}_\pm = \frac{1-n_\pm}{1+n_\pm}$ . Furthermore, one can write the complex index of refraction in terms of the elements of the dielectric tensor by  $n_\pm^2 = \epsilon_{xx} \pm i\epsilon_{xy}$ . If we assume the Kerr rotation and Kerr ellipticity to be



small, one can approximate these parameters by combining the expressions for  $n_{\pm}$ ,  $\tilde{r}_{\pm}$ ,  $\theta_K$  and  $\eta_K$ , yielding

$$\theta_K - i\eta_K \simeq f(\epsilon_{xx})(\epsilon_{xy} + O(\epsilon_{xy}^3)), \quad (3.7)$$

where  $f(\epsilon_{xx})$  is a function of (only)  $\epsilon_{xx}$ . Equation 3.7 explains that the Kerr rotation  $\theta_K$  is proportional to  $\epsilon_{xy}$  in a first approximation. The parameter  $\epsilon_{xy}$  itself is proportional to the relative imbalance in spin up and spin down charge carriers in the system. Note, however, that one should include a spectral dependence as well, and that the Kerr rotation of a light beam does not have to be at resonance with the transition energy of the charge carriers with the spin. The Kerr rotation signal is composed of contributions of oriented spins of charge carriers at all transition energies.

## Setup

The time-resolved Kerr rotation setup is based at the group 'Physics of Nanostructures' of the Eindhoven University of Technology. The main experimentalists, associated with this setup during our collaboration, have been J.H.H. Rietjens and C.A.C. Bosco.

A scheme of the time-resolved Kerr-rotation setup is shown in Fig. 3.8. We use a pulsed Ti:Sapphire laser with a repetition rate of 82 MHz. The laser pulses have a duration of 70 ps, which corresponds to a spectral width of  $10 \sim 15$  nm. The setup does not contain a device which corrects for the group velocity dispersion, therefore, the pulse duration is slightly larger.

The laser beam is divided into a pump and probe beam by a beam splitter. The power of the pump beam is typically 3 – 5 times higher than the power of the probe beam. An optical delay is installed to allow for time-resolved measurements (up to 1.2 ns). The pump beam is modulated into circularly polarized pulses by a PEM module operating at a frequency  $f_{PEM} = 50$  kHz, which is much smaller than the laser repetition frequency. The first lock-in amplifier in Fig. 3.8 is utilized to extract the signal from the modulation of the 50 kHz PEM module.

The probe beam, consequently, passes a 60 Hz chopper to improve the signal-to-noise ratio, which involves the second lock-in in Fig. 3.8. Furthermore, it passes an additional  $\lambda/2$  and linear polarizer for variation in the excitation density. Interaction of the beam with the sample leads to a change in the linear polarization, due to the Kerr effect, and is measured by a  $\lambda/4$  plate, a linear analyzer and a photodiode. The  $\lambda/4$  plate is installed for measurements of the ellipticity, which are not performed in our measurement series.

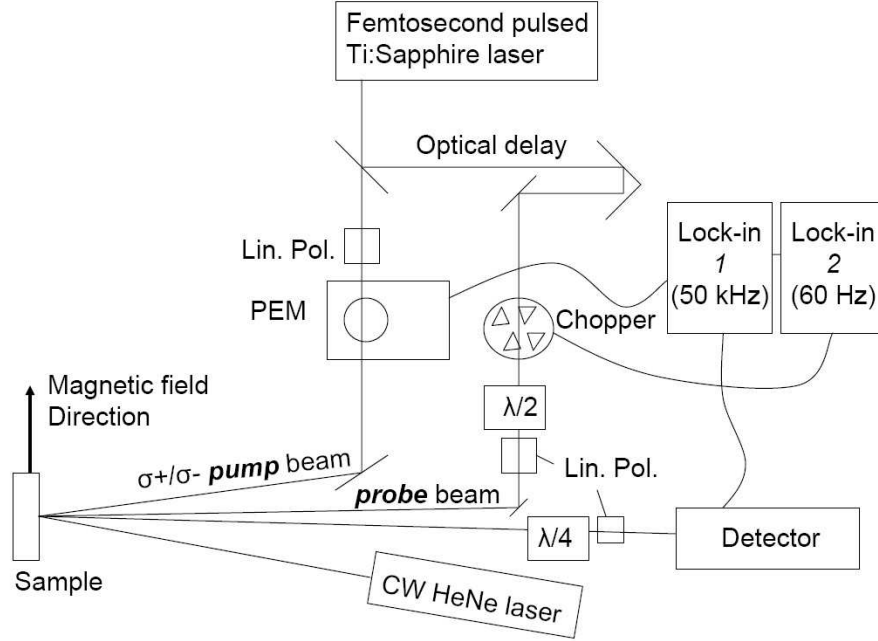


**Figure 3.8:** The time-resolved Kerr-rotation setup.

### 3.4 Sample structure

The structure, grown by molecular beam epitaxy in the group 'Photonics and Semiconductor Nanophysics', consists of a  $p$ -type GaAs substrate (Be-doped,  $5 \times 10^{18} \text{ cm}^{-3}$ ), a 200 nm  $p$ -type (buffer) layer, a 60 nm undoped GaAs and 20 nm  $n$ -type GaAs (Si-doped,  $5 \times 10^{18} \text{ cm}^{-3}$ ). The self-assembled quantum dots are positioned in the middle of the undoped layer. Since the quantum dots are only 50 nm below the surface of the structure, losses due to absorption of laser light are less than 5%. The layer growth sequence is terminated with a growth of identical uncapped quantum dots, which were investigated by AFM measurements. An example of a  $500 \times 500 \text{ nm}$  AFM image of our sample has been shown in Fig. 1.2 (in Ch. 1), which revealed an average base diameter of  $25 \pm 5 \text{ nm}$ , height of  $6.7 \pm 1.5 \text{ nm}$ , and density of  $4.5 \times 10^{10} \text{ cm}^{-2}$ . Besides these densities and average sizes, Fig. 1.2 shows that the quantum dots have an elongated shape. For self-assembled (In,Ga)As quantum dots, the longest axis is pointing in the  $[1\bar{1}0]$  direction, while the short axis is aligned along the  $[110]$  direction. The average aspect ratio of the long and short axis is found to be 1.6 for our quantum dots. Calculations by Pryor and Flatté (2006, 2007) and Sheng (2007) indicate that the  $g$  factor of the quantum dot is very sensitive to the elongation of the quantum dot.

The growth process is initiated by deposition of a wetting layer of 2.1 monolayers of InAs at a relatively high temperature of  $525^\circ\text{C}$ . The high temperature leads to intermixing and to larger dots, since one can expect a larger diffusion path over the surface

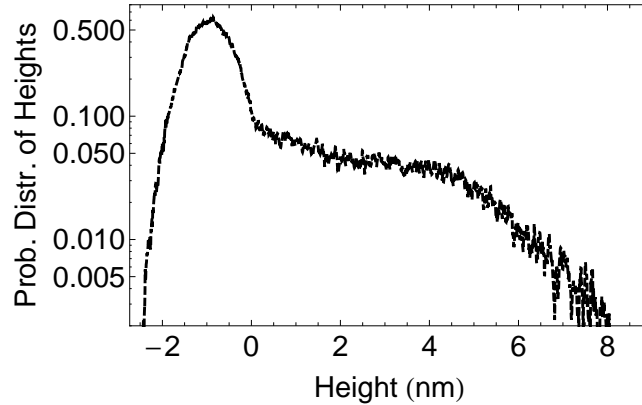


**Figure 3.9:** Figure A shows the quantum dot height probability distribution of the AFM measurement. The height of 0 nm is considered to be the threshold above which only quantum dots occur. Quantum dot heights vary between 4 and 8 nm.

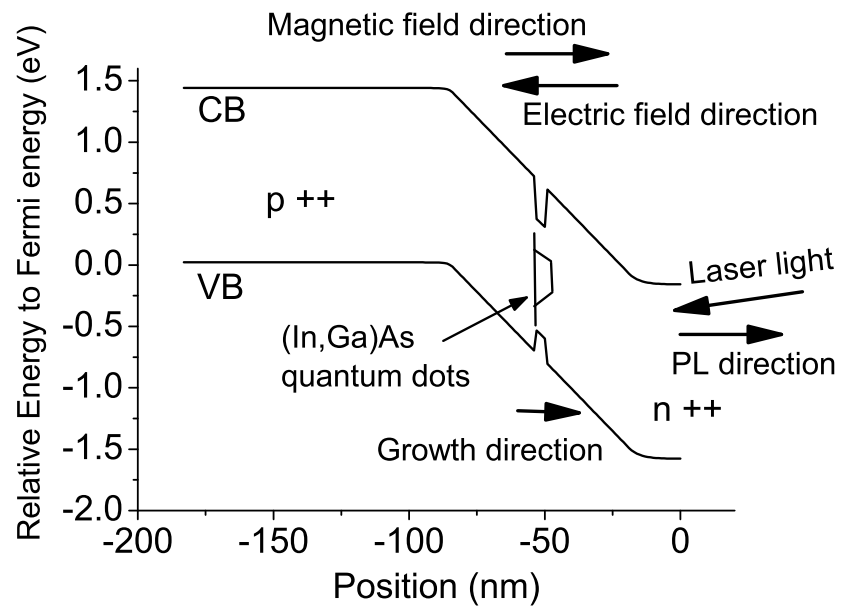
at higher temperatures. Heyn and Hansen (2003) show that the percentage of Gallium in the quantum dot is likely to reach over 50 % for a growth at 525°C. Furthermore, it is shown that the intermixing levels are not uniform throughout the quantum dot (Bruls *et al.*, 2002; Offermans *et al.*, 2005; Heyn *et al.*, 2005).

Fig. 3.9 shows the probability distribution of the heights throughout of the AFM image in Fig. 1.2 in Ch. 1. The quantum dots height varies between 4 and 8 nm. Based on this figure, one would estimate the height of the quantum dots to be slightly smaller than  $\sim 6$  nm (due to the logarithmic scale).

The band-structure of the sample, shown in Fig. 3.10, can be calculated by a simulation program (Tan *et al.*, 1990). This yielded a maximum built-in electric field of 240 kV/cm in the undoped region, where the quantum dots are located. Equivalently, one can estimate this value from the voltage drop of  $\sim 1.5$  V over the 60 nm width of the undoped region.

### 3.5 Electrical characterization of the structure

This work was initially focussed on electrical spin injection into quantum dots. For this reason, mesas were processed from the wafer. The process consisted of the photolithography of the wafer to form circular mesas with a diameter of 200  $\mu\text{m}$ , followed by a wet etch of approximately one minute of a diluted mixture of  $\text{H}_2\text{O}_2$  and  $\text{H}_2\text{SO}_4$ . The process was finished by contacting the top of the mesa with several tens of nanometers of Ti and a thinner layer of gold. On top of this gold surface, a wire was bonded. Current-voltage (I-V) characteristics could be recorded for approximately 20% of the (at least) 50 processed mesas.



**Figure 3.10:** Band diagram of the  $p-i-n$  structure with a single layer of (In,Ga)As quantum dots in a Faraday geometry. The built-in electric field of the structure is  $F = 240 \text{ kV/cm}$ .

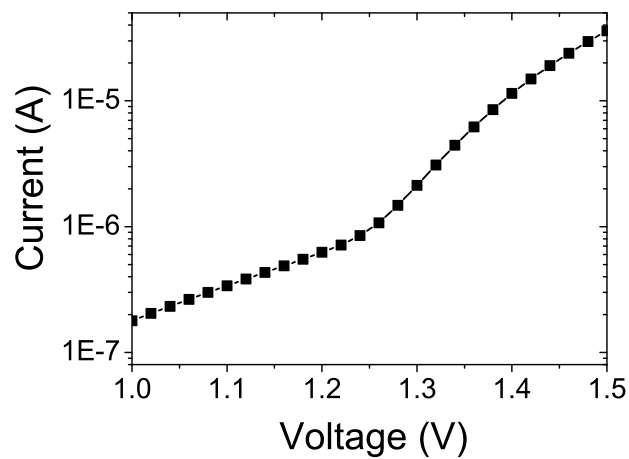


**Figure 3.11:** The current as a function of voltage of one of the diodes.

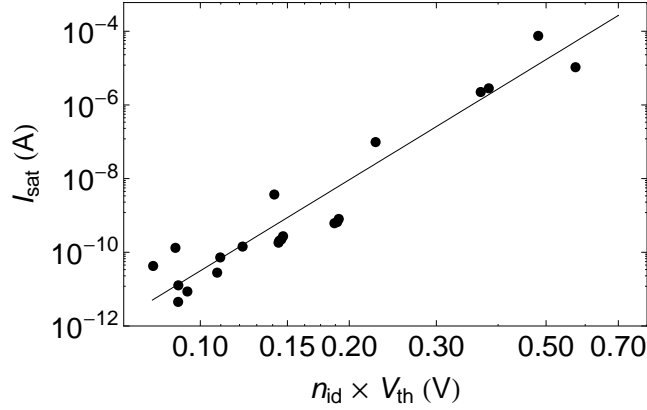


**Figure 3.12:** The saturation current  $I_{sat}$  and product  $(n_{id}V_{th})$  (which is proportional to the temperature) of 21 diodes, determined by Eq. 3.8. The line shows the power law dependence  $A \times (n_{id}V_{th})^m$ , where  $A = 0.005$  and  $m = 8.2$ .

The I-V curves are described by

$$I(V) = I_{sat} \left( e^{\frac{V}{n_{id}V_{th}}} - 1 \right), \quad (3.8)$$

where the ideality factor  $n_{id}$  indicates the quality of the diode,  $V_{th}$  is the thermal voltage,  $\frac{kT}{e}$ , and  $I_{sat}$  is the saturation current. We determined the product  $n_{id}V_{th}$  and  $I_{sat}$  from the measured I-V curves by a least-squares fitting procedure employing Eq. 3.8, which results are shown in Fig. 3.12. The median of the saturation currents from this sample of diodes is  $1.9 \times 10^{-10}$  A. The data reveal a power law dependence between  $I_{sat}$  and  $n_{id}V_{th}$ , which can be written as  $I_{sat} \sim A \times (n_{id}V_{th})^m$ , where  $A = 0.005$  and  $m = 8.2$ . The power law behavior is not fully understood up to now.

The values for  $n_{id}V_{th}$  are much larger than one expects on the basis of the thermal voltage at 5 K and a common ideality factor between 1 and 2. At the temperature of 5 K, where we measure, the thermal voltage *should* be  $V_{th} \sim 4 \times 10^{-4}$  V, whereas Fig. 3.12 reveals values a hundred times larger. The differences could be explained by parasitic resistances.

## Electroluminescence

Besides the I-V curves of the diodes, we were able to observe electroluminescence (EL) from the quantum dots. Figure 3.13A shows the EL spectra as a function of the current, where the spectrum at each current has been normalized. The spectrum shifts to higher energies with increasing current, which is due to a reduced Stark shift through screening. The Stark shifts reach up to 40 meV. Moreover, Fig. 3.13B shows that the integrated EL intensity depends *linearly* on the current for currents above  $\sim 3 \mu\text{A}$ .

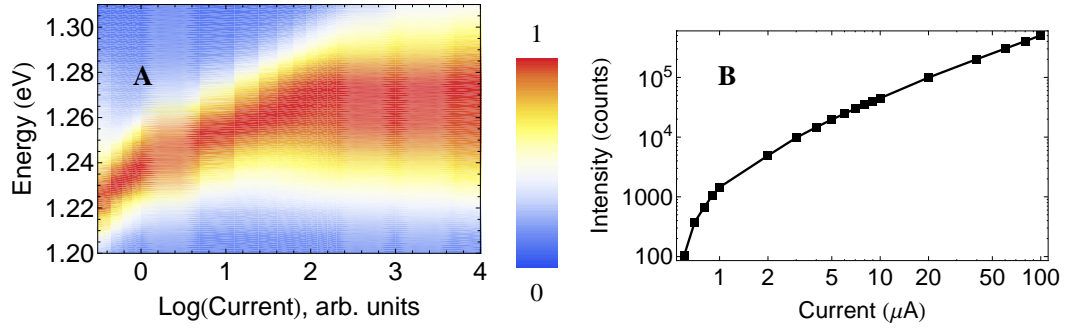


**Figure 3.13:** Figure A shows the normalized electroluminescence spectra as function of the current (logarithmic scale for the current). Figure B shows the integrated intensity of the EL as a function of the current. There exist a linear dependence between the intensity and current for currents above 1  $\mu\text{A}$ .

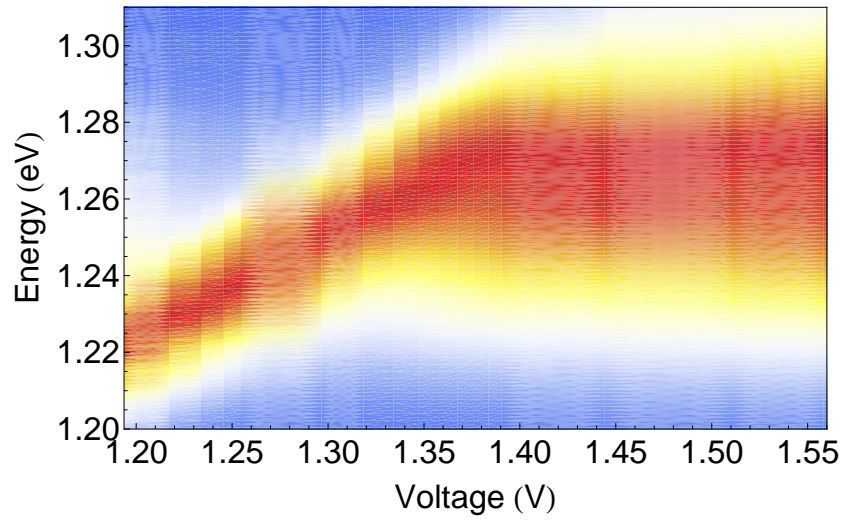


**Figure 3.14:** The normalized EL spectra as a function of the voltage.

Figure 3.14 shows the EL spectrum as a function of voltage. The relatively large voltage which is required to achieve EL can be explained by the work function of the Ti contact.



# All-optical control of the exciton $g$ factor in (In,Ga)As quantum dots

## ABSTRACT

In this chapter, we demonstrate optical tunability of the exciton  $g$  factor of an ensemble of (In,Ga)As quantum dots (Quax *et al.*, 2008). The (In,Ga)As quantum dots are embedded in the center of a  $p-i-n$  structure and, therefore, experience a built-in electric field. Control over the electric field is achieved by a CW laser, since the photo-generated charge carriers can screen the electric field. We employ a Faraday geometry, where the sign of the degree of *circular* polarization of the PL of the quantum dots is a measure of the sign of the  $g$  factor of the quantum dots in the growth direction. Moreover, the Stark shift in the PL spectra acts as a measure for the electric field. Since we observe a sign change in the degree of polarization exactly at the excitation densities where the Stark shift varies, we associate the sign change with the electric field. In fact, we interpret the (sign of) the growth direction  $g$  factor to be controllable with electric field, which is demonstrated by all-optical means in this work. Furthermore, the magnitude of the degree of circular polarization of the PL allows us to determine the longitudinal spin relaxation time  $T_1$  of the exciton. We develop a model for the degree of circular polarization for both low and high excitation densities. The spin relaxation time decreases with increasing magnetic field, following a power law behavior,  $\sim B^m$ , where  $m = -2.9 \pm 0.4$ . This value is in fair agreement with theoretical predictions of Tsitsishvili *et al.* (2003).



## 4.1 Introduction

In chapter 1, we have discussed the possible benefits of (sign) controllable  $g$  factors for quantum information processing (Kane, 1998; Vrijen *et al.*, 2000). Among the experiments aimed at control over the  $g$  factor in nanostructures, both static control over the  $g$  factor in magnetically doped semiconductor quantum dots (Schmidt *et al.*, 2006), as well as dynamic control over the  $g$  factor in quantum wells (Salis *et al.*, 2001) and bulk semiconductors (Kato *et al.*, 2003) have been demonstrated. In the cases of dynamic control, an electric field is used to deform the charge carrier wavefunction, resulting in a modified  $g$  factor. Besides the modification of the shape of the wavefunction, an applied electric field can be used to induce an additional  $g$  factor variation by modifying the wavefunction *overlap* in materials with different  $g$  factors (Salis *et al.*, 2001). In the case of quantum dots, calculations have shown that the  $g$  factor of a strongly confined exciton in a small quantum dot can have a sign opposite to the  $g$  factor of a less confined exciton in a large quantum dot (Nakaoka *et al.*, 2004; Sheng and Babinski, 2007). This sensitivity of the  $g$  factor to the degree of exciton confinement, in combination with large spin relaxation times, makes quantum dots attractive for quantum information devices.

The second part of this chapter focusses on the magnetic field dependence of longitudinal spin relaxation time  $T_1$ . Like the controllable  $g$  factor, long spin relaxation times (and spin decoherence times) are one of the technological requirements for quantum computers. After the first observation of Paillard *et al.* (2001), it appeared that quantum dots indeed have a good spin memory, with spin relaxation times exceeding the recombination time of the exciton. Later, Kroutvar *et al.* (2004) and Heiss *et al.* (2007) have shown that the longitudinal spin relaxation time show a strong magnetic field dependence. Gerardot *et al.* (2008) have recently presented longitudinal spin relaxation times in the order of a millisecond for holes. Generally speaking, the experimental evidence (Kroutvar *et al.*, 2004; Heiss *et al.*, 2007) matches well with the theoretical predictions for the conduction electron (Khaetskii and Nazarov, 2000, 2001; Woods *et al.*, 2002; Westfahl *et al.*, 2004) and holes (Woods *et al.*, 2004; Lü *et al.*, 2005). Whereas there exists a theoretical prediction for the spin relaxation time of the exciton (Tsitsishvili *et al.*, 2003), no experimental evidence for this behavior has been presented so far. In Section 4.5 of this chapter, we show the first experimental evidence of the  $T_1 \sim B^{-3}$  power law behavior of the exciton (Tsitsishvili *et al.* (2003), see also Tsitsishvili *et al.* (2005)).

In the experiments in this chapter, we measure the photoluminescence (PL) and degree of circular polarization of the PL to probe the  $g$  factor and the spin relaxation time. We measure *circular* polarization, since we employ a Faraday geometry where

exciton levels emit photons with opposite helicity. Due to this Faraday geometry, the  $g$  factor in this chapter is the  $g$  factor *in the growth direction*. The degree of circular polarization depends on both the growth direction  $g$  factor and spin relaxation time  $T_1$ , although stronger on the spin relaxation time in our measuring conditions. Section 4.2 describes the two-level model for the bright exciton, to get insight in how the polarization signal depends on the aforementioned parameters, whereas Section 4.3 discusses the overall properties of the PL and the Stark shifts as a function of excitation density. Section 4.4 and 4.5 discuss the two main results on the  $g$  factor and spin relaxation time, respectively.

## 4.2 Model

As an introduction to the model, we recall that we excite the sample with a continuous wave unpolarized Ti:Sapphire laser at 1.61 eV. Since we excite with unpolarized light, we create a balanced amount of spin up and spin down carriers above the GaAs bandgap. Spin relaxation before capture into the quantum dot is neglected. We describe the PL signal to be composed of emission of the two (Zeeman) ground-state exciton levels, denoted by  $|+1\rangle$  and  $|-1\rangle$ , and exclude emission from excited states. Emission from an exciton level is assumed to be proportional to its average occupancy. The experiments are performed in a Faraday geometry with magnetic fields up to 7 Tesla. In such magnetic fields, the Zeeman energy of the ground state exciton can exceed the thermal energy.

The relative occupancy of both Zeeman levels can be investigated since the respective levels emit photons with an opposite polarization. We neglect intermixing between the light- and heavy hole bands in the quantum dot for the moment, which implies that each of the levels emits hundred percent polarized  $\sigma_{\pm}$  photons. Transitions of (predominantly) light holes states are not participating, since these are split apart by several (tens of) meV in the electronic spectrum of the quantum dots. The degree of circular polarization of the PL is defined as

$$\rho = \frac{I_{\sigma_{+1}} - I_{\sigma_{-1}}}{I_{\sigma_{+1}} + I_{\sigma_{-1}}}, \quad (4.1)$$

where  $I_{\sigma_{\pm 1}}$  represents the intensity of  $\sigma_{\pm}$  photons, which thus can only be identified with the polarization of the occupancy of the exciton levels when one excludes heavy-hole/light-hole intermixing.

We denote the up- and downward longitudinal spin relaxation time between the two exciton levels by  $\tau_{s,\uparrow}$  and  $\tau_{s,\downarrow}$ . The downward arrow corresponds to a process where the final state has a lower energy than the initial state. Since the exciton is

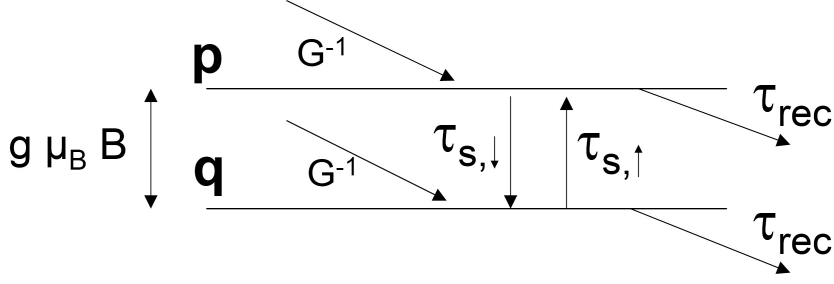


**Figure 4.1:** The spin levels  $p$  and  $q$  of the ground state exciton experience an equal capture rate  $G$  in our experiments. Both levels are assumed to have the same recombination time  $\tau_{rec}$ . Each of the levels emit hundred percent polarized  $\sigma_{\pm}$  light. The degree of circular polarization in the photoluminescence originates from a difference in the occupation of level  $p$  and  $q$ , induced by a difference in downward spin relaxation time  $\tau_{s,\downarrow}$  and upward spin relaxation time  $\tau_{s,\uparrow}$ .

composed of the conduction and valence electron, the exciton spin relaxation time can be described as a product of the spin relaxation times of both charge carriers. For a transition from a *bright* exciton state to the other *bright* exciton state, both the conduction and the valence electron have to flip their spin. We can therefore write, for example,  $(\tau_{|+1\rangle \rightarrow |-1\rangle})^{-1} = (\tau_{|-\frac{1}{2}\rangle \rightarrow +|\frac{1}{2}\rangle})^{-1} (\tau_{|-\frac{3}{2}\rangle \rightarrow +|\frac{3}{2}\rangle})^{-1}$  where  $\tau$  is the spin relaxation time and the subscripts refer to the exciton ( $|\pm 1\rangle$ ), conduction electron ( $|\pm \frac{1}{2}\rangle$ ), and valence electron ( $|\pm \frac{3}{2}\rangle$ ).

The two Zeeman levels of the ground state exciton, denoted by  $p$  and  $q$ , are shown in Fig. 4.1. Note that  $p$  and  $q$  represent Zeeman levels and are nondegenerate. Their average occupancy is expressed by a value between 0 and 1, and their energies are split by  $g\mu_B B$ . The time-dependent evolution of the occupancy of the levels ( $p(t)$  and  $q(t)$ ) is described by the differential equations (Hyland *et al.*, 1999; Mackowski *et al.*, 2003; Flissikowski *et al.*, 2003)

$$\begin{aligned} \dot{p} &= G - \frac{p}{\tau_{rec}} - \frac{p}{\tau_{s,\downarrow}} + \frac{q}{\tau_{s,\uparrow}}, \\ \dot{q} &= G - \frac{q}{\tau_{rec}} + \frac{p}{\tau_{s,\downarrow}} - \frac{q}{\tau_{s,\uparrow}}, \end{aligned} \quad (4.2)$$

where  $G$  is the generation rate (i.e., capture rate) in the levels,  $\tau_{rec}$  is the radiative recombination time of a single exciton for the levels, and  $\tau_{s,\downarrow(\uparrow)}$  is the downward (upward) spin relaxation time. Equations 4.2 describe the two-level exciton system at low excitation densities, such that a transition between the exciton levels (by spin relaxation) or capture is never inhibited because of an already occupied final state. Transitions are thus only dependent on the occupation of the *initial* state. The case of high excitation densities is discussed later in this section. The spin relaxation times  $\tau_{s,\downarrow}$  and  $\tau_{s,\uparrow}$  in

Eq. 4.2 are related to the longitudinal spin relaxation time  $T_1$  by (Hyland *et al.*, 1999; Marshall and Miller, 2001; Tsitsishvili *et al.*, 2003)

$$T_1 \equiv \left( \frac{1}{\tau_{s,\downarrow}} + \frac{1}{\tau_{s,\uparrow}} \right)^{-1}, \quad (4.3)$$

$$\simeq \tau_{s,\downarrow} \quad \text{when} \left( \frac{1}{\tau_{s,\uparrow}} \right) \rightarrow 0, \quad (4.4)$$

where the condition in Eq. 4.4 occurs for  $g\mu_B B \gg kT$ .

One can consider two possible mechanisms of relaxation between the Zeeman levels: phonon-assisted relaxation and Auger recombination. In the literature, relaxation processes dominated by both phonon-assisted relaxation (Adler *et al.*, 1996) as well as Auger recombination (Morris *et al.*, 1999) have been observed, although Auger recombination processes between Zeeman levels have not been reported. Auger recombination is inefficient when (i) the temperature is low (Uskov *et al.*, 1997), (ii) the quantum dot sizes are large (due to reduced wavefunction overlap with charge carriers outside the quantum dot) (Uskov *et al.*, 1997; Ferreira and Bastard, 1999), and when (iii) the 3D carrier concentration in the surrounding bulk material is high (due to effective screening of surrounding charge carriers) (Uskov *et al.*, 1997). Furthermore, it is required that the spin is conserved in a two-identical-particle Auger process (e.g., employed by Ferreira and Bastard (1999)). Since our measurements are performed in high magnetic fields, at low temperatures (i), in relatively large quantum dots (ii), and with a CW laser creating charge carriers in the bulk material surrounding the quantum dot (iii), one can already expect the Auger process to be inefficient. However, a much stronger, experimental argument is presented in Ch. 5, where risetimes exceeding 100 ps are observed (see Fig. 5.5). In very recent experiments (data not shown here), such long risetimes were also observed on equivalent quantum dots by T.E.J. Campbell Ricketts. These long risetimes can be associated with phonon-assisted recombination (Adler *et al.*, 1996). Based on this evidence, we assume the spin relaxation process to be dominantly phonon-assisted.

In the case of phonon-assisted spin relaxation, one can express the upward rate in terms of the downward rate, because of a different absorption and emission probability of acoustic phonons. For the downward spin relaxation transition, an acoustic phonon is emitted, while for an upward transition, an acoustic phonon is absorbed. One can write (Blum, 1981)

$$\frac{1}{\tau_{s,\downarrow}} \sim (N_{\omega_q} + 1) \quad , \text{ whereas } \quad \frac{1}{\tau_{s,\uparrow}} \sim N_{\omega_q}, \quad (4.5)$$

where  $N_{\omega_q} = (e^{\frac{\hbar\omega_q}{kT}} - 1)^{-1}$  is the thermal phonon distribution (i.e., Bose-Einstein distribution), and  $\omega_q$  is the angular frequency of the acoustic phonon. We assume that the

transitions are driven by acoustic phonons, which have an energy  $\hbar\omega_q = g\mu_B B$  when the Zeeman energy is  $g\mu_B B$ . The ratio between the upward and downward rate, in the case of an energy difference  $g\mu_B B$ , is given by a (Boltzmann) factor  $\frac{N_{\omega_q}}{N_{\omega_q+1}} = e^{-\frac{g\mu_B B}{kT}}$ . We can therefore replace  $\frac{1}{\tau_{s,\uparrow}}$  by  $e^{-\frac{g\mu_B B}{kT}} \frac{1}{\tau_{s,\downarrow}}$  in Eq. 4.2.

## Simple Model

Firstly, we present a simple model to get a sense of the most important parameters in this chapter:  $T_1$  and  $\tau_{rec}$ . The simple model is based on two assumptions:

- Transitions are not suppressed because of an already occupied *final* state.
- The Zeeman energy is much larger than the thermal energy  $kT$ :  $g\mu_B B \gg kT$ .  
This condition holds for our measurements at the highest magnetic fields.

Due to the last approximation, the last term in the Eq(s). 4.2 can be neglected. In the stationary case, where  $\dot{p} = 0$  and  $\dot{q} = 0$ , the polarization becomes independent of the generation rate  $G$ , and is described by

$$\rho(\tau_{rec}, T_1) \simeq \frac{\tau_{rec}}{\tau_{rec} + T_1}, \quad (4.6)$$

$$\rho(\tau_{rec}, T_1) \simeq \frac{\tau_{rec}}{T_1} \quad \text{when } \tau_{rec} \ll T_1, \quad (4.7)$$

where the condition of Eq. 4.7 is occurring in our measurements. Equation 4.6 explains, that under the condition  $g\mu_B B \gg kT$ , one can determine the spin relaxation time of the excitation from the recombination time  $\tau_{rec}$  and the degree of circular polarization  $\rho$  only.

## Extended Model

To describe the signal in the case of higher temperatures or lower magnetic fields, one can employ a model using the following conditions:

- Transitions are not suppressed because of an already occupied *final* state.
- The Zeeman energy is comparable to the thermal energy  $kT$ :  $g\mu_B B \sim kT$ . Such a condition occurs when the magnetic field is around 3 T in our experiments. Neglecting the upward rate is not possible now and an upward term like  $\frac{1}{\tau_{s,\uparrow}} = e^{-\frac{g\mu_B B}{kT}} \frac{1}{\tau_{s,\downarrow}}$  is included.

Note that in this situation,  $T_1 \neq \tau_{s,\downarrow}$ , because of Eq. 4.3, and we have to use  $\tau_{s,\downarrow}$ . If one employs the relation  $\tau_{s,\uparrow} = e^{\frac{g\mu_B B}{kT}} \tau_{s,\downarrow}$  in the Eqs. 4.2, one finds for the steady-state polarization

$$\rho(\tau_{rec}, \tau_{s,\downarrow}, \frac{g\mu_B B}{kT}) = \frac{(1 - e^{-\frac{g\mu_B B}{kT}})\tau_{rec}}{(1 + e^{-\frac{g\mu_B B}{kT}})\tau_{rec} + \tau_{s,\downarrow}}, \quad (4.8)$$

$$\rho(\frac{g\mu_B B}{kT}) \simeq \tanh(\frac{g\mu_B B}{2kT}) \quad \text{when } \tau_{s,\downarrow} \ll \tau_{rec}. \quad (4.9)$$

To estimate the effects of the exponential term in Eq. 4.8, we investigate the sensitivity of the polarization  $\rho$  on the  $g$  factor by plotting the ratio of  $\rho/\rho_0$  (where  $\rho_0$  is the polarization in Eq. 4.6) as a function in of the ratio  $g\mu_B B/kT$  in Fig. 4.2. The asymptotic behavior for  $g\mu_B B \gg kT$  in Fig. 4.2 reveals that, independent of the ratio of the downward spin relaxation time and the recombination time,  $\rho$  is only sensitive to the  $g$  factor when  $g\mu_B B \lesssim 4kT$ . In this regime, the extended model should be applied. At a temperature of 1.7 K and a  $g$  factor of 2, the equality  $g\mu_B B = 4kT$  corresponds to a magnetic field of 5 T. Therefore, application of Eq. 4.8 instead of Eq. 4.6 is required for magnetic fields below 5 T.

Although posed for reasons of completeness, the condition in Eq. 4.9 ( $\tau_{s,\downarrow} \ll \tau_{rec}$ ) is unlikely to occur in our measurements. It is accepted that the  $T_1$  times are much larger than the radiative recombination time in (In,Ga)As quantum dots (Paillard *et al.*, 2001; Kroutvar *et al.*, 2004; Gerardot *et al.*, 2008).

## Extended model including suppressed transitions

A difficulty arises when the average number of excitons in the quantum dot,  $\bar{n}$ , is not negligably small. Qualitatively, one can expect that the degree of circular polarization is reduced, since one can expect a relatively larger contribution from transitions of the upper spin level. One can quantitatively include this by introducing a 'partial Pauli

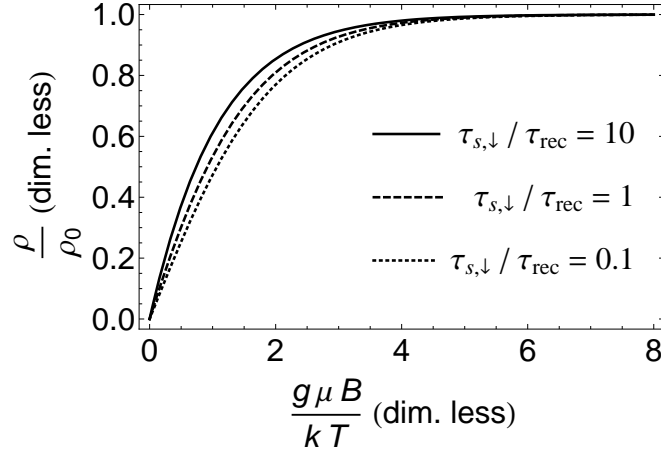


**Figure 4.2:** The ratio  $\rho/\rho_0$  (where  $\rho$  is Eq. 4.8 and  $\rho_0$  is Eq. 4.6) as a function of the ratio  $g\mu_B B/kT$ , for a ratio  $\tau_{s,\downarrow}/\tau_{\text{rec}}$  of 10, 1, and 0.1. The asymptotic behavior shows that the exciton  $g$  factor is easier to probe when  $g\mu_B B \lesssim \frac{kT}{4}$ .

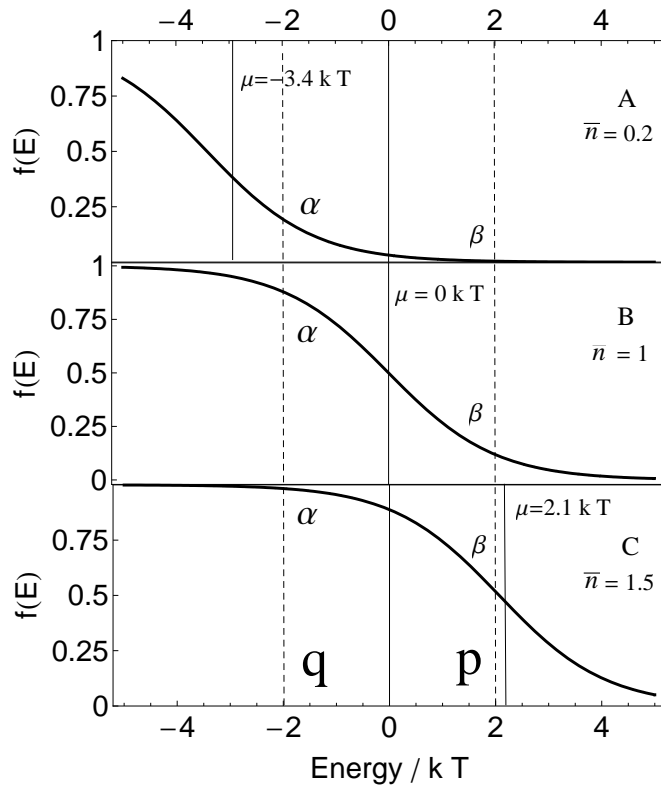


**Figure 4.3:** The panels show the Fermi-Dirac distribution as a function of energy, for an average population of 0.2 (Fig. A), 1.0 (Fig. B) and 1.5 (Fig. C). We identify the occupation probabilities  $\alpha$  and  $\beta$  with the values of the function at the energies of the levels  $p$  and  $q$ . In this example,  $p$  and  $q$  are positioned at  $2kT$  and  $-2kT$ . The associated chemical potentials  $\mu$  are denoted in the frames.

blockade<sup>†</sup> in the differential equations of Eq. 4.2. One should incorporate terms like  $p(1 - \alpha)$  and  $q(1 - \beta)$  to express that transitions are blocked when the final state is already occupied<sup>‡</sup>. The differential equations can in that case be written as

$$\begin{aligned}\dot{p} &= G - \frac{p}{\tau_{rec}} - \frac{p(1 - \alpha)}{\tau_{s,\downarrow}} + e^{-\frac{g\mu_B B}{kT}} \frac{q(1 - \beta)}{\tau_{s,\downarrow}}, \\ \dot{q} &= G - \frac{q}{\tau_{rec}} + \frac{p(1 - \alpha)}{\tau_{s,\downarrow}} - e^{-\frac{g\mu_B B}{kT}} \frac{q(1 - \beta)}{\tau_{s,\downarrow}},\end{aligned}\quad (4.10)$$

where we have already incorporated the relation  $\tau_{s,\uparrow} = e^{\frac{g\mu_B B}{kT}} \tau_{s,\downarrow}$ . One should in principle also include a factor of the type  $(1 - \alpha/\beta)$  to describe the reduction in the generation rate  $G$ . However, in the stationary case, the final result is independent of this term. For the stationary case, where  $\dot{p} = 0$  and  $\dot{q} = 0$ , we can write

$$\rho(\tau_{rec}, \tau_{s,\downarrow}, \frac{g\mu_B B}{kT}, \alpha, \beta) = \frac{(1 - \alpha - (1 + \beta)e^{-\frac{g\mu_B B}{kT}})\tau_{rec}}{(1 - \alpha + (1 - \beta)e^{-\frac{g\mu_B B}{kT}})\tau_{rec} + \tau_{s,\downarrow}} \quad (4.11)$$

which results in Eq. 4.8 when  $\alpha, \beta \rightarrow 0$ . One can identify  $\tau_{s,\downarrow}$  with  $T_1$  when  $\alpha, \beta \rightarrow 0$ . The values of  $\alpha$  and  $\beta$  represent the relative occupance of both spin levels, and describe the 'strength' of the blocking by a number between 0 and 1. Since the lowest spin level has the largest occupation, the value  $\alpha$  should be larger than  $\beta$  (see Eq. 4.10 and Fig. 4.1). Equation 4.11 confirms that  $\rho$  decreases when  $\alpha$  increases, and is a translation of the reduced polarization in the case of biexcitonic transitions.

It is not obvious how the occupation of the spin levels is distributed for the two-level spin system in the quantum dot. We approximate the distribution of the levels to follow a Fermi-Dirac distribution,  $f_{FD}(E - \mu) = (1 + e^{\frac{E - \mu}{kT}})^{-1}$ , where  $E$  represents the relative energy and  $\mu$  the chemical potential. The  $\alpha$  and  $\beta$  are approximated to be the Fermi-Dirac probabilities at the energies of the levels  $p$  and  $q$ . They can be derived from the following equations

$$\alpha = f_{FD}(-\frac{1}{2}g\mu_B B - \mu(\bar{n})), \quad (4.12)$$

$$\beta = f_{FD}(+\frac{1}{2}g\mu_B B - \mu(\bar{n})), \quad (4.13)$$

$$\text{where } \bar{n} = f_{FD}(-\frac{1}{2}g\mu_B B - \mu) + f_{FD}(+\frac{1}{2}g\mu_B B - \mu), \quad (4.14)$$

---

<sup>†</sup>Strictly speaking, the Pauli blockade is a discrete 'on/off' process, for example written as 0 or 1. For the *average* degree of circular polarization of  $\sim 10^6$  quantum dots, however, we assume this effect to be describable by a real value between 0 and 1.

<sup>‡</sup>The parameters  $\alpha$  and  $\beta$  can be interpreted as the average occupance of both levels:  $\alpha = \bar{q}$  and  $\beta = \bar{p}$ . One can also employ factors like  $(1 - q)$  and  $(1 - p)$  instead of  $(1 - \alpha)$  and  $(1 - \beta)$ , but the polarization is in that case dependent on the capture rate. We want to avoid that in this model.



where  $\mu(\bar{n})$  can be derived as the inverse function of Eq. 4.14. For every  $\bar{n}$ , one can find an  $\alpha$  and  $\beta$ , from which we derive  $\tau_{s,\downarrow}$  (given  $\rho$ ). Figure 4.3 shows how  $\alpha$  and  $\beta$  increase when the chemical potential  $\mu$  increases.

### Sign of the polarization

Although the magnitude of the polarization depends on the average number of excitons in the dot, the *sign* of the polarization is exclusively determined by the sign of the  $g$  factor of the exciton. Our orientation of the magnetic field and the detection optics is such, that a negative exciton  $g$  factor corresponds to a positive polarization. This sign determination is confirmed by a calibration of the polarization detection on the free-to-bound transitions in  $p$ -type GaAs (Obukhov *et al.*, 1980).

### Circular polarization in the case of 'relaxed optical selection rules'

If each of the exciton levels does not emit fully polarized light due to heavy-hole/light-hole intermixing, a fraction of the detected photons is misinterpreted. We denote this fraction of photons with opposite helicity by  $\epsilon$ , where  $0 \leq \epsilon < 1$ . We assume that the heavy-hole/light-hole intermixing is 'symmetric', which means that if one of the exciton levels emits 5% of photons with a light-hole related helicity, the other exciton level also emits 5% (again with opposite helicity). This can be quantified by applying the replacement rules  $I_{\pm 1} \rightarrow (1 - \epsilon)I_{\pm 1} + \epsilon I_{\mp 1}$  in Eq. 4.1. In the case of intermixing with a fraction  $\epsilon$ , the *observed* degree of polarization  $\rho^*$  of the PL can be expressed in the polarization of the occupancy of the levels by

$$\rho^*(\epsilon, \rho) = (1 - 2\epsilon)\rho, \quad (4.15)$$

where  $\rho^*$  can only be identified with  $\rho$  when  $\epsilon = 0$ .

Calculations on lens-shaped quantum dots have shown a near unity conversion of spin- to photon polarization, when measuring in the growth direction, indicating that  $\epsilon$  is small (Pryor and Flatté, 2003). Based on experiments of Cortez *et al.* (2001) and calculations by Sheng and Babinski (2007), one can estimate  $\epsilon$  to be at most  $\sim 0.1$ . Note that  $\epsilon$  depends on both the squared amplitude of the light hole state (in the predominantly heavy hole state) and the oscillator strength between the conduction electron and light hole. For  $\epsilon = 0.1$ , one can have a squared amplitude of 0.3 for the light holes, since the oscillator strength between the conduction electron and light hole is three times smaller.

Finally, we consider the effects of a nonzero  $\epsilon$  on our analysis. First of all, one should note that intermixing does not affect the sign of the polarization. The analysis of the  $T_1$  times, however, is affected. Employing Eq. 4.6 and Eq. 4.15, one can write,

$$\left(\frac{T_{1,\epsilon}}{T_{1,0}}\right) = \frac{1}{1-2\epsilon} \left(\frac{1-\rho+2\epsilon\rho}{1-\rho}\right), \quad (4.16)$$

$$\simeq \frac{1}{1-2\epsilon} \simeq 1+2\epsilon + O((2\epsilon)^2) \quad \text{when } \epsilon \ll 1, \quad (4.17)$$

where  $T_{1,0}$  is the spin relaxation time based on the assumption of a one-to-one conversion of occupancy of the exciton levels into the polarization of the light ( $\epsilon = 0$ ). The  $T_{1,\epsilon}$  represents the deduced spin relaxation time in the case of heavy-hole/light-hole intermixing by a fraction  $\epsilon$  (i.e., the 'observed' spin relaxation). The 'observed' spin relaxation time, deduced from the observed degree of polarization  $\rho^*$  (reduced because of  $\epsilon > 0$ ), in fact, overestimates  $T_{1,0}$  by a factor  $\sim (1+2\epsilon)$ . From the maximum  $\epsilon = 0.1$ , one can conclude that  $T_{1,0}$  is at least 80% of  $T_{1,\epsilon}$ .

### 4.3 Photoluminescence and Stark shifts

Figure 4.4 shows the normalized PL spectra, the integrated intensity and full width at half maximum (FWHM) of the PL spectra, respectively, as a function of laser excitation density. At excitation densities below  $20 \text{ Wcm}^{-2}$  (regime I), the PL peak is centered at  $1.23 \text{ eV}$  and is independent on the excitation density. When the excitation density is increased above  $20 \text{ Wcm}^{-2}$  (regime II), the PL peak is shifted to higher energies for excitation densities of  $40 \text{ Wcm}^{-2}$  (regime III), saturating at  $1.27 \text{ eV}$ . Regime I corresponds to the situation where the quantum dots experience the unscreened built-in electric field. The electric field is progressively screened by photo-created carriers in regime II. Finally, in regime III, the internal electric field is completely screened by the photo-created carriers. The maximum value for the Stark shift, which is observed in regime I, amounts to  $40 \pm 3 \text{ meV}$  and is associated with the calculated electric field of  $240 \text{ kV/cm}$ . Such a Stark shift is not uncommon for (In,Ga)As quantum dots (Jin *et al.*, 2004; Wang *et al.*, 2006). It is, however, the largest Stark shift in quantum dots observed in an *optical* experiment. A similar behavior of the PL as a function of the excitation density for quantum dots in the intrinsic region of a *p-i-n* structure has been

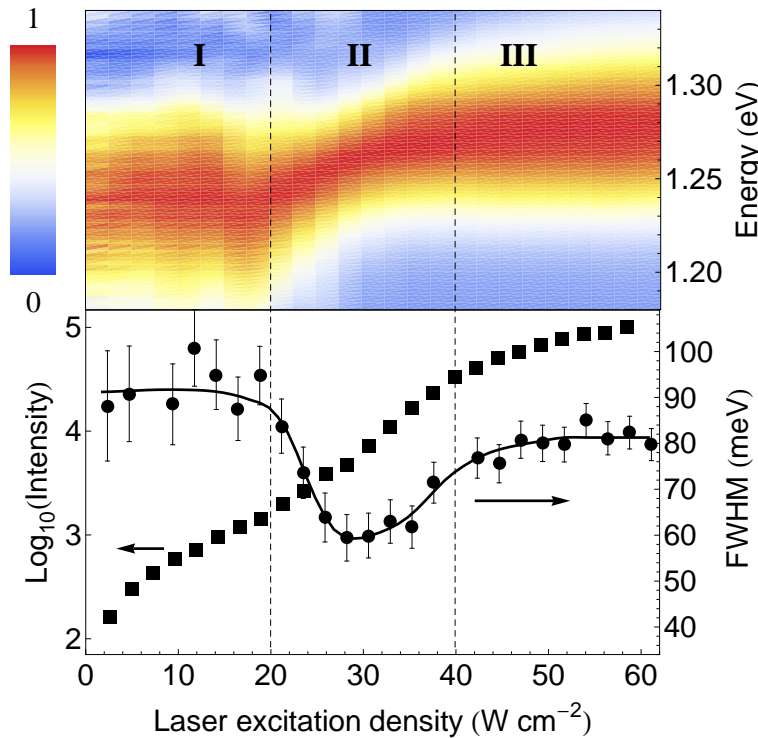


**Figure 4.4:** The top panel shows the normalized PL spectra, and the bottom panel shows the intensity (■, left axis) and the FWHM (●, right axis) of the spectra, as a function of excitation density.

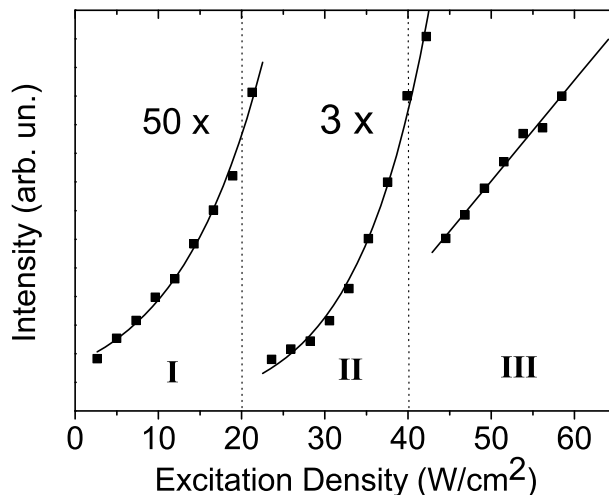


**Figure 4.5:** The integrated intensity of the quantum dot PL as a function of the excitation density. In regime I and II, a (nearly) exponential behavior occurs, due to the electric field over the quantum dots. In regime III, however, the regular linear behavior occurs.

observed before (Bulashevich *et al.*, 2006).

Figure 4.5 shows that the regimes I and II are characterized by a near-exponential dependence of the intensity on the excitation density, whereas regime III shows a linear dependence. This indicates that in regime I and II, the electric field induces a reduction of the PL intensity through tunneling of carriers out of the quantum dot (Fry *et al.*, 2000a). The lower panel of Fig. 4.4 shows that the total range of intensities covers three orders of magnitude. This figure also shows that the FWHM is found constant in regime I and III (where the electric field is also constant) and that a minimum occurs in regime II.

One can use the relation between the observed Stark shift  $\Delta_S$  in the PL and the electric field  $F$  to assign an electric field to every excitation density. This relation is quadratic in  $F$ ,  $\Delta_S = \beta F^2 + pF$ , where  $\beta$  describes the polarizability and  $p$  is the built-in dipole moment in the dot. A value for  $\beta$  for (In,Ga)As quantum dots has been determined by Hsu *et al.* (2001). They report  $\beta = (8.8 \pm 0.8) \times 10^{-35} \text{ C V}^{-1} \text{ m}^2$ . There have been observations of built-in dipoles in an apex-to-base orientation (Fry *et al.*, 2000b; Hsu *et al.*, 2001) and a base-to-apex orientation (Jin *et al.*, 2004). Absolute values for the dipole range from  $p = 5 \times 10^{-29} \text{ C m}$  (Fry *et al.*, 2000b) to  $p = 12 \times 10^{-29} \text{ C m}$  (Hsu *et al.*, 2001).

In the PL of Fig. 4.4, we observe a maximum Stark shift of 40 meV. To reach this Stark shift at 240 kV/cm, with  $\beta = 8.8 \times 10^{-35} \text{ C V}^{-1} \text{ m}^2$  (Hsu *et al.*, 2001), the dipole should be in a base-to-apex orientation, and is found to be  $p = (5.4 \pm 1.9) \times 10^{-29} \text{ C m}$  ( $= (3.4 \pm 1.2) \text{ e}\text{\AA}$ ). If one excludes the built-in dipole, one can estimate a

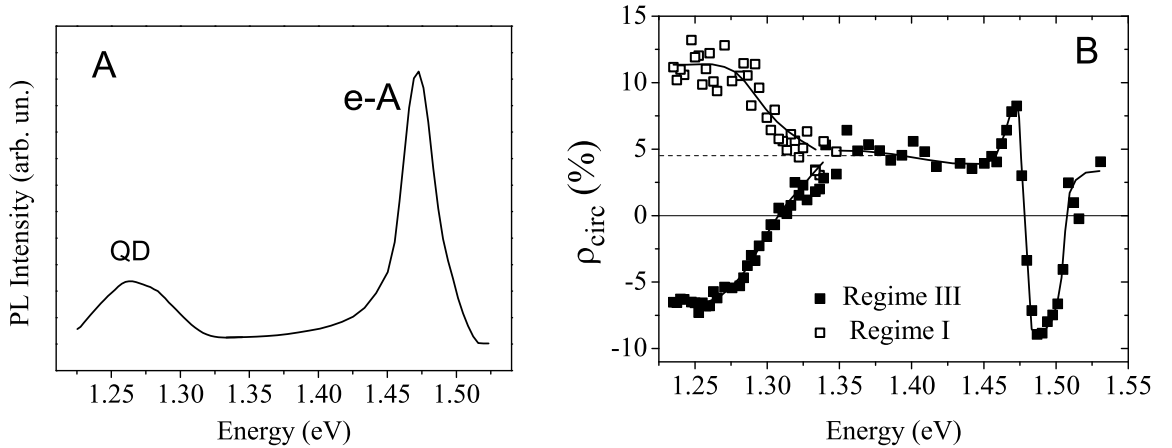
$\beta = (11.0 \pm 0.8) \times 10^{-35} \text{ C V}^{-1} \text{ m}^2$  from the maximum Stark shift at 240 kV/cm. The value for  $p$  is relatively small, whereas the  $\beta$  is relatively large (see Table 2.2). This matches with calculations of Wang *et al.* (2006), who indicate that strong intermixing of Gallium into the quantum dots, which we expect to have occurred during our quantum dot growth, leads to reduction of the built-in dipole and increase of the polarizability. The parameters  $\beta$  and  $p$  are used later in our analysis.

Now we have introduced the regimes to discriminate whether the quantum dots experience a high or low electric field, we comment on how the polarization signal is built up.

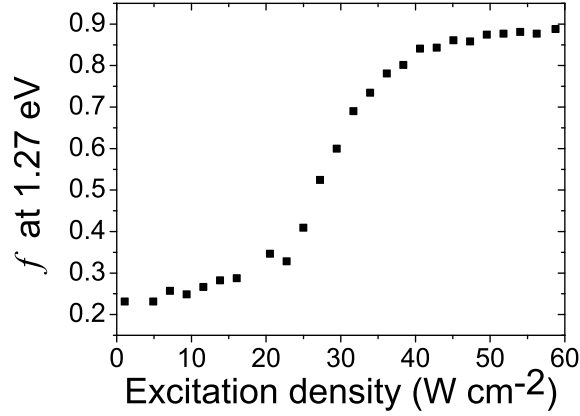
### Corrections of the polarization signal

Figure 4.6A shows the PL of the sample at high excitation density (regime III) in the energy range 1.22 – 1.53 eV, where we clearly observe the contributions from the quantum dots (QD in Fig. 4.6A) at 1.22 – 1.34 eV and the free-to-bound transitions from the  $p$ -type material (e-A in Fig. 4.6A) at 1.45 – 1.50 eV. Note that there is PL emission in the range 1.34 – 1.45 eV, between the peaks, which is associated with emission of (deep) acceptors as well. These acceptors have their transition energies slightly lowered due to, for example, a nearby vacancy or other impurity. The intensity of the PL in this range is several orders of magnitude smaller than from the main acceptor peak at 1.48 eV. We observe the emission of these deep acceptors to be apparent at the quantum dot energies as well. Therefore, we have to apply a background correction to the measured degree of polarization of the quantum dots.

Figure 4.6B shows the degree of circular polarization,  $\rho$ , at a temperature of 1.7 K and magnetic field of 7 T in the range from 1.22 – 1.53 eV. The polarization data in Fig. 4.6B is uncorrected data. From Fig. 4.6B, one can already observe the difference in the sign of the polarization in Regime I and III (discussed further in Section 4.4). In the energy range from 1.34 – 1.45 eV, there appears a rather constant value of 4.5%, independent of the excitation density. The change in the polarization near the main



**Figure 4.6:** Figure A shows a PL spectrum at high excitation density, where we identified the quantum dot transitions (QD) and the free-to-bound transitions in the  $p$  type material (e-A). A maximum of approximately 35% of the transitions occur in the quantum dots. Figure B shows the uncorrected degree of circular polarization throughout the full energy range, both for an excitation density in regime I ( $\square$ ) and for excitation density in regime III ( $\blacksquare$ ). The polarization is independent of the excitation density, except for the energies below  $\sim 1.34$  eV, where the quantum dots emit.



**Figure 4.7:** The fraction of quantum dot signal in the total PL signal,  $f$ , as a function of the excitation density at 1.27 eV. This data is used to extract the polarization data of Fig. 4.8, employing Eq. 4.18.

acceptor peak at 1.48 eV in Fig. 4.6B has been observed and explained by Obukhov *et al.* (1980).

Based on the polarization we observe in the energy range 1.34 – 1.45 eV in Fig. 4.6, we assume that the 4.5% of polarization in this range also applies to the *background* intensity of the quantum dots (1.22 – 1.34 eV). The actual polarization from the quantum dots,  $\rho_{qd}$ , can be extracted from a weighted average of the polarization of the background ( $\rho_{bg} = 4.5\%$ ) and the quantum dots. We describe the background fraction by  $f$ , where  $f$  is a value between 0 and 1. This background fraction depends on the energy  $E$ , therefore we write

$$\bar{\rho}(E) = f(E)\rho_{qd}(E) + (1 - f(E))\rho_{bg} \quad (4.18)$$

where  $\bar{\rho}$  is the observed polarization. The correction is particularly important in the PL spectra with low excitation densities.

Figure 4.7 shows the ratio  $f$  from the quantum dots at an average energy of 1.27 eV. We used the integrated intensities from 1.264 eV to 1.276 eV. The ratio  $f$  varies from  $\sim 0.2$  to 0.9.

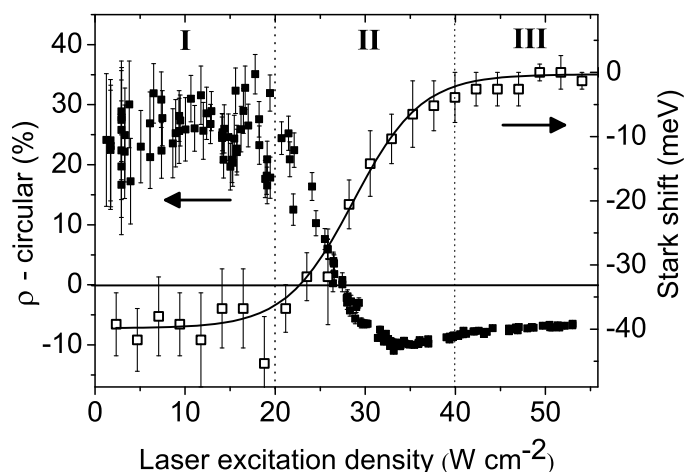
#### 4.4 Sign reversal of the exciton $g$ factor

Figure 4.8 shows the degree of circular polarization after correction for the background by Eq. 4.18, at the center of the PL peak (in high excitation densities, 1.27 eV), in a magnetic field of 7 Tesla and a temperature of 1.7 K. As the excitation power is increased, the polarization varies from  $25 \pm 4\%$  in regime I to  $-9.5 \pm 0.5\%$  in regime II. The degree of circular polarization reverses sign at an excitation density of  $\sim 27 \text{ W/cm}^2$ . A further increase of the excitation density in regime III leads to a small increase in the polarization to  $-7\%$ .

The Stark shift and sign reversal of the degree of circular polarization occur in the excitation density regime II. We propose that the electric field over the quantum dot, modified by the excitation density, induces this reversal. The sign reversal of  $\rho$  is interpreted as a sign reversal of the  $g$  factor *in the growth direction* of the ground state exciton.

We exclude a sign reversal caused by excited (shell) states, since these are not observed in the PL spectra at even the highest excitation densities in our measurements. We do not exclude that biexcitons transitions occur at the highest excitation densities. However, these transitions are not expected to become dominant. Furthermore, biexcitons would only suppress the polarization, since they emit unpolarized light on average. Note that the polarization of biexcitons can be described by Eq. 4.11, where  $\bar{n} > 1$  in Eq. 4.14.

One can extract an upper boundary for the average number of excitons in a quantum dot,  $\bar{n}$ , from the input flux of photons. The photon flux is  $\phi = 2.0 \times 10^{20} \text{ cm}^{-2}\text{s}^{-1}$  at a



**Figure 4.8:** The degree of circular polarization (■, left axis) and Stark shift (□, right axis) at a magnetic field of 7 Tesla and a temperature of 1.7 K, as a function of the laser excitation density.



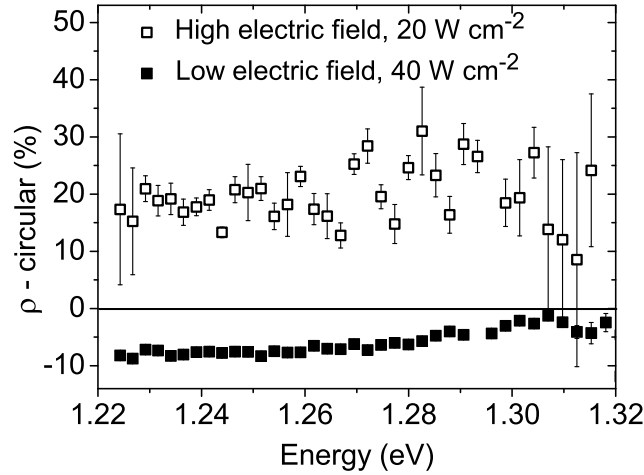


**Figure 4.9:** The spectral dependence of the polarization, measured at the boundaries of regime II ( $20 \text{ kW cm}^{-2}$  ( $\square$ ) and  $40 \text{ kW cm}^{-2}$  ( $\blacksquare$ )).

high excitation density of  $50 \text{ W cm}^{-2}$ . The flux per quantum dot is  $\phi/n_{qd}$ , where  $n_{qd}$  is the surface density of the quantum dots (see Ch. 3). We determined that a maximum of 35% of the radiative recombination occurs in the quantum dots, by comparing the overall intensity of the free-to-bound transitions and the transitions from the quantum dots in the PL spectra. Therefore, the maximum rate of radiative recombination in the dots is  $1.6 \times 10^9 \text{ s}^{-1}$ . We measured a radiative recombination time of 1.0 ns, from which a maximum average number of excitons per quantum dot  $\bar{n} = 1.6$  at  $50 \text{ W/cm}^2$  is deduced. Note that this calculation does not take into account non-radiative recombination, and hence acts as an upper boundary.

Figure 4.9 shows the two extrema of the polarization of Fig. 4.8 observed at excitation densities of  $20 \text{ W/cm}^2$  and  $40 \text{ W/cm}^2$  at a magnetic field of 7 T. These excitation densities correspond to the boundaries of range II where we observed the full range of the polarization sign reversal. Figure 4.9 shows only a weak dependence of the extrema as a function of energy. The sign reversal of the polarization appears throughout the whole ensemble, therefore, it has not been necessary to correct for the Stark shift, which is not done in Fig. 4.9. Moreover, the sign reversal is also observed at the low energy side of the spectrum, where *only* ground state transitions occur, which is considered as additional evidence that the reversal is not driven by excited states transitions.

Since we know the relation between the Stark shift and the electric field,  $\Delta_S = \beta F^2 + pF$ , one can plot the polarization data as a function of the electric field. Figure 4.10 shows the transformed data for the  $\beta = 8.8 \times 10^{-35} \text{ C V}^{-1} \text{ m}^2$  and  $p = 5.4 \times 10^{-29} \text{ C m}$ , and for the  $\beta = 11.0 \times 10^{-35} \text{ C V}^{-1} \text{ m}^2$  and  $p = 0 \text{ C m}$ . Both sets of parameters result in a maximum observed Stark shift at  $F = 240 \text{ kV/cm}$ . Depending on the choice

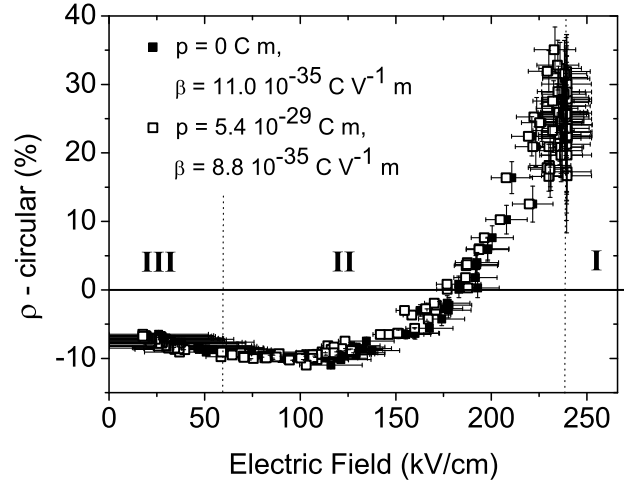


**Figure 4.10:** The degree of circular polarization as a function of the electric field, for a parameter pair including a built-in dipole ( $\square$ ) and excluding the built-in dipole ( $\blacksquare$ ). For clarity, only one set of data is displayed with error bars.

of parameters and taking into account the error bars, sign reversal occurs between  $F = 170 \text{ kV/cm}$  and  $F = 210 \text{ kV/cm}$ . The inclusion of a dipole only leads to an insignificant correction.

The literature on  $g$  factors in the *growth direction* of quantum dots provides insight into its dependence on size, shape and In-Ga composition in the quantum dot. One can claim that the electron  $g$  factor appears in the range from  $-1$  to  $0$  (Nakaoka *et al.*, 2004; Pryor and Flatté, 2006; Sheng and Babinski, 2007; Pryor and Flatté, 2007) for normal quantum dot parameters. The valence electron  $g$  factor occurs in the range from  $-5$  to  $+1$  (Nakaoka *et al.*, 2004), for parameters yielding PL energies in the range  $1.25 \sim 1.30 \text{ eV}$ . It was shown that small dots have a small positive  $g_v$ , whereas large dots have a large negative  $g_v$ . Since  $g_e$  shows little sensitivity to parameter changes, we expect the valence electron  $g_v$  to induce the sign change.

The negative polarization at low electric fields is associated with a positive  $g_{exc}$ . We think that the electric field effectively leads to a reduction of the exciton confinement in the quantum dot, inducing  $g_v$  to cancel  $g_e$  and yielding a sign change of  $g_{exc}$ . This interpretation would match qualitatively with the behavior of  $g_{exc}$  for increasing quantum dot sizes (Nakaoka *et al.*, 2004).

### Sign reversal at magnetic fields below 7 T

We discussed the sign reversal of the polarization as a function of the excitation density at a magnetic field of 7 T. The highest available magnetic field was chosen to achieve largest possible contrast in the sign reversal measurement. In this subsection, we show

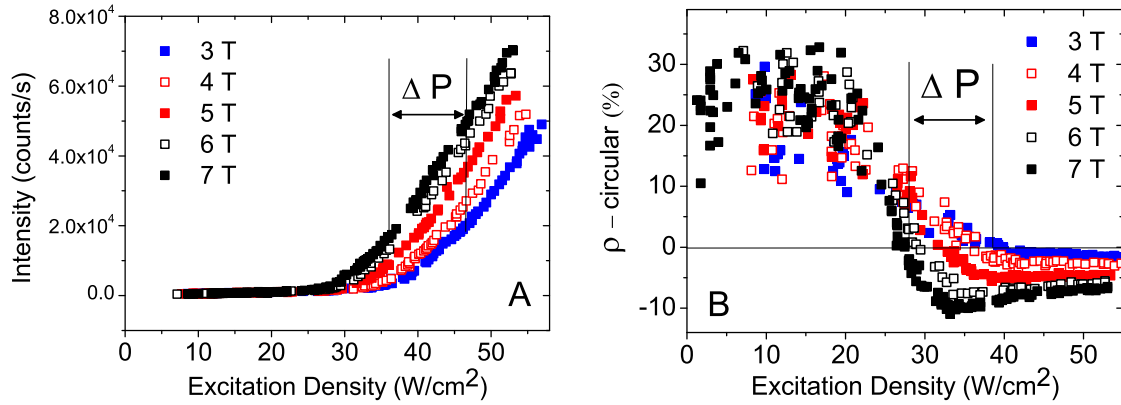


**Figure 4.11:** Figure A shows the intensities of the PL and Fig. B shows the degree of circular polarization of the PL, as a function of excitation density at magnetic fields from 3 T to 7 T. The error range in Fig. B at every excitation density can not be compared between the data sets, since the polarization was determined from a variable amount of total counts. Figure A and B show both a difference  $\Delta P \sim 10 \text{ W/cm}^2$  in the excitation density.

severals scans of the polarization at lower magnetic fields, to verify whether the sign reversal occurs at the same electric field in different magnetic fields.

To achieve a similar mapping as in Fig. 4.10 for different magnetic fields, we performed the scans of the degree of polarization as a function of the excitation density from 0 T up to 7 T, with steps of 1 T. Whereas Fig. 4.11A shows the intensities associated with this PL measurements, Fig. 4.11B shows its degree of circular polarization. The error range in Fig. 4.11B at every excitation density can not be compared between the data sets, since the polarization was determined from a variable amount of total counts. A sign change is observable at all magnetic fields, also for the data at 1 T and

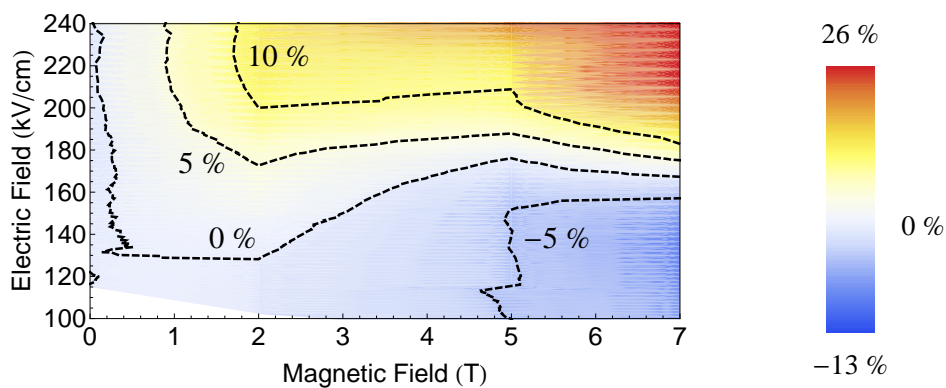


**Figure 4.12:** This figure shows the degree of circular polarization and the iso-polarization lines of  $-5\%$ ,  $0\%$ ,  $5\%$ , and  $10\%$  as a function of the magnetic field and electric field.

2 T, which is not shown in Fig. 4.11B.

The most important observation in Fig. 4.11A is that the PL intensities show a clear magnetic field dependence. The excitation density difference,  $\Delta P$ , is not induced by drift of the detector, since the measurements are performed in a couple of hours after each other. In fact, the difference  $\Delta P$  of approximately  $10 \text{ W/cm}^2$  in excitation density could be caused by a magnetic field dependent capture rate. The magnetic length (i.e., the radius of the cycle of an electron in a magnetic field) might play an important role here. At 3 T, the magnetic length roughly equals the diameter of the quantum dot, which could suppress capture and lower the PL efficiency, as shown in Fig. 4.11A. The suppression of capture could possibly be described by a kind of Bragg reflectance in the case of resonance between the charge carrier magnetic length and quantum dot diameter.

Since the excitation density difference  $\Delta P$  is also observed in the measurements of the degree of polarization in Fig. 4.11B, we expect that  $\Delta P$  does *not* represent a *magnetic field* dependence of the sign change of the exciton  $g$  factor (which Fig. 4.11B suggests in first instance). Also the Stark shifts in the PL (data not shown here), like the intensities in Fig. 4.11A, exhibited a excitation density difference  $\Delta P$ .

By combining the PL spectra (with Stark shifts) and polarization data, we formed the plot in Fig. 4.12. No exact overlap was found between this Stark shift measurement at 7 T and the Stark shift in Fig. 4.4 and Fig. 4.8 (difference of  $\sim 35 \text{ kV/cm}$ ), which is likely due to the difference in the sensitivity of the detector (each of the detectors has its own sensitivity curve as a function of energy). We have, however, matched the zero-crossing in this figure with the  $F = 170 \text{ kV/cm}$  in Fig. 4.10. The dashed iso-polarization lines represent polarization values of  $-5\%$ ,  $0\%$ ,  $5\%$  and  $10\%$ . Values at 0 T are below  $0\%$  (due to a systematical error in the alignment) and are therefore just left of the  $0\%$  iso-polarization line.

Figure 4.12 shows that a sign reversal is achieved between  $130 \text{ kV/cm}$  and  $170 \text{ kV/cm}$ , which we, regarding the coarse method, consider to be constant. This confirms that the  $g$  factor in the growth direction changes sign as a function of the electric field only, independent of the magnetic field.

## 4.5 Spin relaxation time as a function of magnetic field

In Section 4.1, we noted the importance of long spin relaxation times for applications of the spin of charge carriers to act as a qubit. This section presents measurements on the spin relaxation times of the exciton in magnetic fields from 3 T to 7 T. The data reveals a power law behavior for  $T_1$ , as predicted by Tsitsishvili *et al.* (2003).

The downward spin relaxation process of the exciton at the highest energy is characterized by the emission of an acoustic phonon. The typical time associated with this process, the downward spin relaxation time, can be written as (Tsitsishvili *et al.*, 2003)

$$T_1 \simeq \tau_{s,\downarrow} \sim \left( \frac{E_{lh} - E_{hh}}{\Delta_{ex}} \right)^2 (g\mu_B B)^{-3}, \quad (4.19)$$

where the  $\Delta_{ex}$  is the exchange interaction energy between the bright and dark exciton and  $(E_{lh} - E_{hh})$  is the energy difference between the light hole (lh) and heavy hole (hh). Equation 4.19 shows that spin relaxation times get smaller when the energy difference between the light hole exciton and heavy hole exciton gets smaller or when the exchange interaction  $\Delta_{ex}$  gets larger. In this work, however, we focus on the magnetic field dependence of the spin relaxation time. We derive the behavior for the polarization as a function of the magnetic field from the different scans in Fig. 4.11B. The dependence is investigated for low electric fields (regime III in Fig. 5.3).

To select a comparable set of polarization data at every magnetic field, we combine Fig. 4.11A and Fig. 4.11B to form Fig. 4.13. This figure shows that the point at which

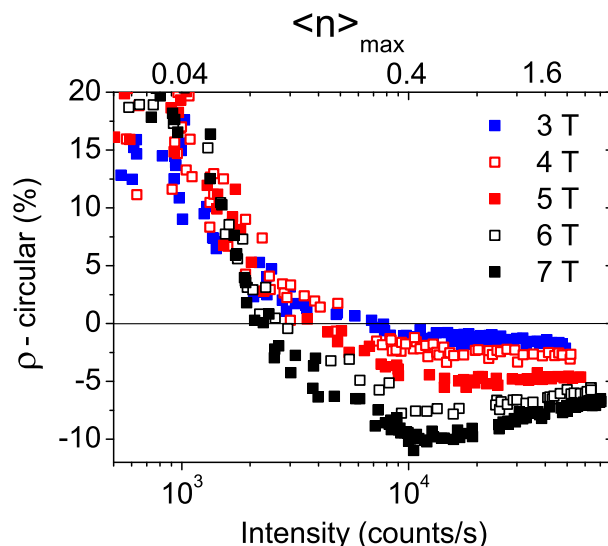


**Figure 4.13:** The degree of circular polarization as a function of PL intensity. The top axis represents the maximum occupancy in the quantum dot,  $\bar{n}$ . The data has not been corrected for the  $-0.5\%$  of background.

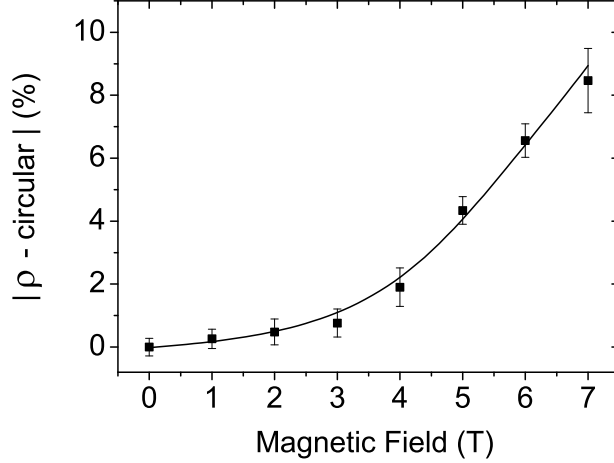


**Figure 4.14:** The absolute value of the average of the degree of circular polarization as a function of the magnetic field. The values have been corrected for a background of  $-0.5\%$ . The error range represents the variation of the polarization data within the selection. The line is a guide to the eye.

the circular polarization strongly changes its derivative with excitation density (e.g., the minimum in  $\rho$  at 7 T), in fact, occurs at the same PL intensity of  $\sim 10^4$  counts per second for every magnetic field. On the top axis in Fig. 4.13, we have shown the maximum occupancy of the quantum dot,  $\bar{n}_{\text{max}}$ , where we used the estimate of  $\bar{n}_{\text{max}} = 1.6$  at  $50 \text{ W/cm}^2$ . For such a linear mapping between the intensity and  $\bar{n}$ , the rate of biexciton emission should be small.

Since we are interested in the degree of circular polarization as a function of the magnetic field at low electric fields, we incorporate the polarization data of regime III. In Fig. 4.13, regime III corresponds to intensity rates exceeding  $2 \times 10^4$  counts/s. We should, however, avoid to incorporate the polarization data associated with a high occupancy of the quantum dot (because this suppresses the polarization, recall Eq. 4.11). Since the descending trends (in absolute value) of the polarization data with increasing excitation density for the magnetic fields of 6 T and 7 T suggest that some biexciton transitions occur, we include the polarization data only up to  $4 \times 10^4$  counts/s. For the same reason, we also include the data in the range from  $1 \times 10^4$  to  $2 \times 10^4$ , which experience a small electric field (this boundary is also suggested by the minimum of  $\rho$  at 7 T). The variation of the degree of circular polarization within the final range of intensities between  $1 \times 10^4$  counts/s and  $4 \times 10^4$  counts/s in Fig. 4.13 is translated into an error bar.

Figure 4.14 shows the absolute value of the polarization at high excitation densities as a function of the magnetic field, where the error range represents the variation of the polarization data within the intensity range selection. A background correction of  $0.5\%$  has been applied to the both the data series (due to a systematical error in the

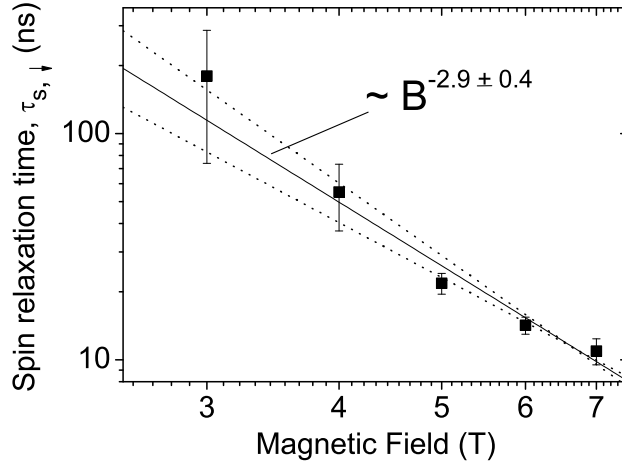


**Figure 4.15:** The spin relaxation times as a function of the magnetic field. The data has been obtained employing Eq. 4.8 with a  $g$  factor of 2. A power law behavior,  $\sim B^m$ , where  $m = -2.9 \pm 0.4$  is observed, in close agreement with the prediction of Tsitsishvili *et al.* (2003). The solid line shows the fit of  $CB^m$  with  $C = 2.8 \mu\text{s}$  and  $m = -2.9$ , whereas the slopes of the dotted lines correspond with  $m = -2.5$  and  $m = -3.3$ .

alignment), based on the average polarization at 0 T. The data points at 1 T and 2 T have been discarded in the analysis of the spin relaxation times, since their error range crosses zero.

We start the analysis using Eq. 4.8. This equations hold for the condition that the excitation density is low, such that  $\bar{n} \ll 1$ . The recombination time  $\tau_{rec}$  has been found to be 1.0 ns, which will be discussed in Ch. 5. Figure 4.15 shows the spin relaxation times  $\tau_{s,\downarrow}$  as a function of the magnetic field, applying Eq. 4.8 with  $g = 2$ . The value for the  $g$  factor is determined by  $\mu$ -PL measurements. The error bars in Fig. 4.15 correspond to the errors of the polarization at every magnetic field in Fig. 4.14.

Figure 4.15 shows a lower boundary for the spin relaxation time of  $\sim 70$  ns at 3 T. Exceeding this magnetic field, a strong decrease of the spin relaxation time occurs, reaching  $T_1 = 10.9 \pm 1.4$  ns at 7 T. The data in the range from 3 to 7 T shows a linear descending trend on the double-logarithmic plot, which corresponds to a power law behavior. A fitting procedure with  $CB^m$ , where  $B$  is the magnetic field, yielded  $m = -2.9 \pm 0.4$ , close to the predicted  $m = -3$  of Tsitsishvili *et al.* (2003). Each of the data points has been weighted inversely proportional to their error range on the logarithmic scale in Fig. 4.15. The dotted lines in Fig. 4.15 correspond to a power law behavior with  $m = -2.5$  and  $m = -3.3$ .

Besides the polarization at high excitation densities, we investigated the dependence at low excitation densities (data not shown). This data did not reveal a threshold at 3 T, like in Fig. 4.14, and showed a nearly linearly increasing dependence. Like for the

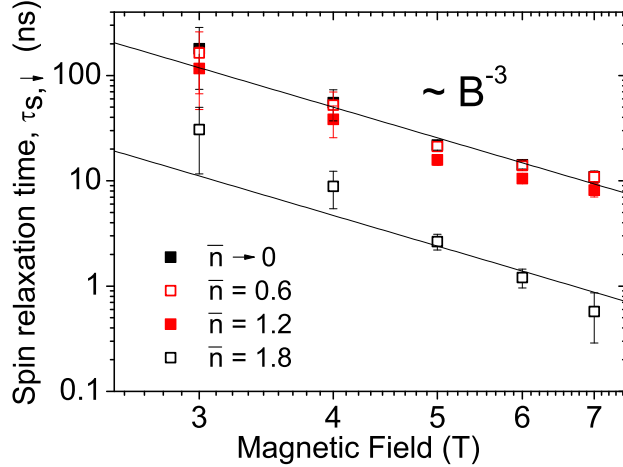


**Figure 4.16:** This figure shows the spin relaxation time in the range from 3 T to 7 T at several average occupations  $\bar{n}$ , determined by Eq. 4.11 and the parameters  $\alpha$  and  $\beta$  in Eq. 4.12 and Eq. 4.13. The lines show a  $B^{-3}$  power law behavior, but are not actual fits.

high excitation density data, we performed a fitting procedure with  $CB^m$ . A fit with  $g = 0.5$  in Eq. 4.8 yielded a factor  $m = 0$  (i.e.,  $\tau_{s,\downarrow}$  is constant), whereas a fit with  $g = 2$  resulted in  $m = -0.9$ . One can therefore conclude that at high electric fields, the power law behavior with  $m \sim -3$  is not maintained, which is probably due to leakage of the carrier wavefunction out of the quantum dot. Instead of  $m \sim -3$ , one can claim that  $-1 \leq m \leq 0$  in the high electric field regime.

Since the data in Fig. 4.15 is measured at high excitation densities, we derive  $\tau_{s,\downarrow}$  also for the case when  $\bar{n} \ll 1$  is not applicable anymore. For these conditions, we use Eq. 4.11 for  $\rho$ , where we introduced the parameters  $\alpha$  (Eq. 4.12) and  $\beta$  (Eq. 4.13) to include inhibited transitions. Figure 4.16 shows the spin relaxation time for occupations of  $\bar{n} = 0.6$ ,  $\bar{n} = 1.2$ , and  $\bar{n} = 1.8$ . An overall shift to lower values for the spin relaxation time occurs when  $\bar{n}$  increases, but this decrease is at most one order of magnitude. Figure 4.16 reveals, most importantly, that the behavior with increased  $\bar{n}$  still shows a power law behavior  $T_1 \sim CB^m$ , where  $m \sim -3$ . For  $\bar{n} = 1.8$ , one can expect a larger (absolute value of the) exponent than  $|m| = 3$  in the power law.

The values for  $C$  in the fitting procedure with  $CB^m$ , which represent the spin relaxation time at 1 T, yielded a lower boundary of  $C = 0.4 \mu\text{s}$  at  $\bar{n} = 1.8$ . One can therefore safely claim that the spin relaxation time  $T_1$  exceeds  $0.4 \mu\text{s}$  at 1 T and 1.7 K. Upper boundaries for  $C$  are found to be  $48 \mu\text{s}$  (for  $\bar{n} \rightarrow 0$ ), which is larger than the estimate of  $C = 13 \mu\text{s}$  by Tsitsishvili *et al.* (2003). Equation 4.19 explains, however, that the spin relaxation time is very sensitive to the heavy-hole/light-hole energy splitting and the exchange interaction.



To compare these values, the literature presents numerous results on the longitudinal spin relaxation time, both in (In,Ga)As quantum dots (Gotoh *et al.*, 1998; Paillard *et al.*, 2001; Laurent *et al.*, 2005; Kroutvar *et al.*, 2004; Takeuchi *et al.*, 2004; Gündoğdu *et al.*, 2005; Smith *et al.*, 2005; Gerardot *et al.*, 2008) and in CdSe quantum dots (Mackowski *et al.*, 2003; Flissikowski *et al.*, 2003). A dependence of the spin relaxation time on the magnetic field was measured for the conduction electron (Kroutvar *et al.*, 2004), and recently also for the valence electron (Heiss *et al.*, 2007). While some authors have presented shorter values for the spin relaxation times of the exciton in (In,Ga)As quantum dots (Gotoh *et al.*, 1998; Takeuchi *et al.*, 2004) than we observe, others presented comparable values (Paillard *et al.*, 2001). Differences with Gotoh *et al.* (1998) can be explained by the different geometry and sizes of the system.

The method we employ can be considered crucial to observe such long spin relaxation times. For example, from a method where one compares the PL decay rates after circularly polarized excitation (Paillard *et al.*, 2001), it would have been harder to determine a spin relaxation time of the order of 100 ns.

The fact that the power law with  $m \sim -3$  was retrieved, even when  $\bar{n} \ll 1$  is not applicable anymore, acts as strong experimental evidence for the theory of Tsitsishvili *et al.* (2003). To our knowledge, this is the first observation of this behavior for excitons in quantum dots. Since the strong power law behavior is abandoned when an electric field is applied, one can conclude that confinement within the quantum dots is crucial for good spin memory. This experiment confirms that quantum dots indeed 'freeze' the spin very well.

# Radiative recombination times of (In,Ga)As quantum dots in electric fields

## ABSTRACT

In this chapter, we present the electric field dependence of the radiative recombination time of (In,Ga)As quantum dots embedded in a *p-i-n* structure. This dependence is determined from spectrally- and time-resolved PL data. The photo-created carriers of the pulsed laser system quench the built-in electric field of the *p-i-n* structure temporarily, which can be monitored via the time-resolved Stark shift in the PL. Nearly 1 ns after the laser pulse arrival, the quenching effect (i.e., lowering of the built-in electric field) reaches a maximum. The electric field builds up again after this maximum, with a typical time-scale of several nanoseconds. Besides the time-dependent Stark shift, the PL intensity showed a clearly non-exponential decay. The irregular, non-exponential decay is associated with a temporally varying recombination time. We find a reduced recombination rate (i.e., increasing recombination time) as a function of time, which is associated with the increasing electric field as a function of time. The data of the non-exponential decay and the time-resolved Stark shift are combined to extract the recombination time as a function of the electric field. The recombination time without electric field is found to be  $\tau_{rec} = 1.0$  ns, which increases almost a factor 4 when the electric field is increased to  $\sim 150$  kV/cm.

## 5.1 Introduction

Much research has been focussed on finding possibilities to tune the radiative lifetime of excitons in modulated semiconductor structures. Increased radiative lifetimes, using electric fields, were observed in *quantum wells* by Polland *et al.* (1985) and Köhler *et al.* (1988). By applying electric fields, they control the overlap between the conduction and valence electron wavefunction. On the other hand, measurements employing exciton-photon coupling have demonstrated a decrease in radiative recombination time in quantum wells (Deveaud *et al.*, 1991).

The first studies on recombination times in *quantum dots* (Mukai *et al.*, 1996; Raymond *et al.*, 1996; Bayer *et al.*, 1999; Dekel *et al.*, 2000) were solely focussed on mapping the decay processes in quantum dots. Like for the quantum wells, later studies shifted their attention to create active control over the recombination time, employing special sample structures and gates to induce and control electric fields over the quantum dots. For example, Smith *et al.* (2003) describes the controlled two-exponential decay in a sample structure with a hole gas next to the quantum dot layer. To control the radiative lifetime, even the quantum-electrodynamical Purcell effect has been exploited in quantum dots in microcavities (Gerard *et al.*, 1998; Graham *et al.*, 1999; Kiraz *et al.*, 2001; Solomon *et al.*, 2001; Gayral *et al.*, 2001; Reithmaier *et al.*, 2004; Peter *et al.*, 2005), as well as coupled quantum dots (Bayer *et al.*, 2000). Like the experiment by Smith *et al.* (2003), Kroutvar *et al.* (2004) also employ a gate to control the occupation of one of the charge carriers in the quantum dot, hence yielding long recombination times ( $\tau_{rec} > 10$  ns). However, Kroutvar *et al.* (2004) 'ionize' the exciton by extracting one of the charge carriers out of the quantum dot, after which recombination is enforced by having a charge carrier enter the quantum dot again. Contrary to the study of Kroutvar *et al.* (2004), where the recombination time is 'dictated' by the voltage pulse sequence, this study investigates the 'intrinsic' increase in recombination time when the overlap between the charge carrier wavefunctions is reduced by an electric field.

The control of the radiative lifetime in quantum dots can be particularly interesting for applications as single-photon sources (Santori *et al.*, 2000) and quantum dot lasers (Anantathanasarn *et al.*, 2008). Furthermore, lifetime-control has been proposed for quantum information devices (Pellizari *et al.*, 1995; Imamoglu *et al.*, 1999), where cavity modes would mediate interactions between qubits. An electrically-controllable radiative lifetime in quantum dots could be applicable in single-photon sources in a relatively simple fashion, i.e., without implementation of high finesse cavities.

This study is characterized by an integral analysis of the *temporal* and *spectral* response of the photoluminescence (PL) of a single layer of (In,Ga)As/GaAs quantum dots, embedded in a *p-i-n* structure. The details of the sample structure have been

explained in Ch. 3. We employ pulsed excitation which can temporarily quench the built-in electric field in the structure, due to the screening of the photo-created carriers. Note that we refer to photo-created carriers outside the quantum dots here. In this sense, the quantum dots experience a modulated electric field, varying at the pulse frequency of the laser system. The PL spectra show a time-dependent Stark shift as a signature of the modulated electric field. The amount of quenching of the built-in electric field depends on the laser excitation density, and can be measured by the PL peak position just after the laser pulse arrival. Complete quenching of the built-in electric field can be achieved at the highest excitation densities.

Besides the Stark shifts observed in the temporal response of the PL, we observe clear variation in the intensity decay rates (i.e., derivatives) of the time-resolved PL spectra. We exclude that the variation of decay rates originates from a summation of single exponential decays from the inhomogeneous size distribution of the quantum dots, since it is highly unlikely that the range of recombination times within the probed bandwidth varies so strongly as we observe (almost a factor 4 for a probed bandwidth of 10 meV). Instead, we associate the time-dependent electric field with the varying decay rates to determine the electric field dependence of the recombination times.

## 5.2 Model

The pulsed excitation of the laser induces a time-dependent Stark shift in the PL spectra, which is utilized to determine the time-dependent electric field. We employ the quadratic dependence of the Stark shift on the electric field, written as  $\Delta_S(F) = \beta F^2 + pF$ , where  $\beta$  is the polarizability and  $p$  is the internal dipole of the quantum dot (Fry *et al.*, 2000b; Hsu *et al.*, 2001; Jin *et al.*, 2004), and the parameters  $\beta = 6.0 \times 10^{-4}$  meV/(kV/cm) (Hsu *et al.*, 2001) and  $p = 6.4$  eÅ. The time-dependent Stark shifts and electric fields are schematically drawn in Fig. 5.1A–C.

Figure 5.1D shows a schematic intensity decay of the quantum dots, which was tracked on the maximum of the PL spectrum at every time-step. In practice, we measure the intensity on a grid with ranges  $t \in [0; 10]$  ns for the time and  $E \in [1.175; 1.365]$  eV for the energy. The step-sizes in this grid are  $\Delta t = 110$  ps and  $\Delta E \sim 6$  meV for the time and energy, respectively. In our analysis, we make use of interpolated functions at every time-step to determine the position of the maximum. Consequently, we integrate the intensity in a bandwidth of 10 meV to obtain the intensity of the signal at every time  $t$ . In this way, we have obtained a tracked intensity decay (i.e., following the maxima), which evidently did *not* show a single exponential decay. As stated, we assume that this is due to the time-dependent electric field. The tracked intensity decay (Fig. 5.1D) and the time-dependent electric field (Fig. 5.1C) can be used to determine

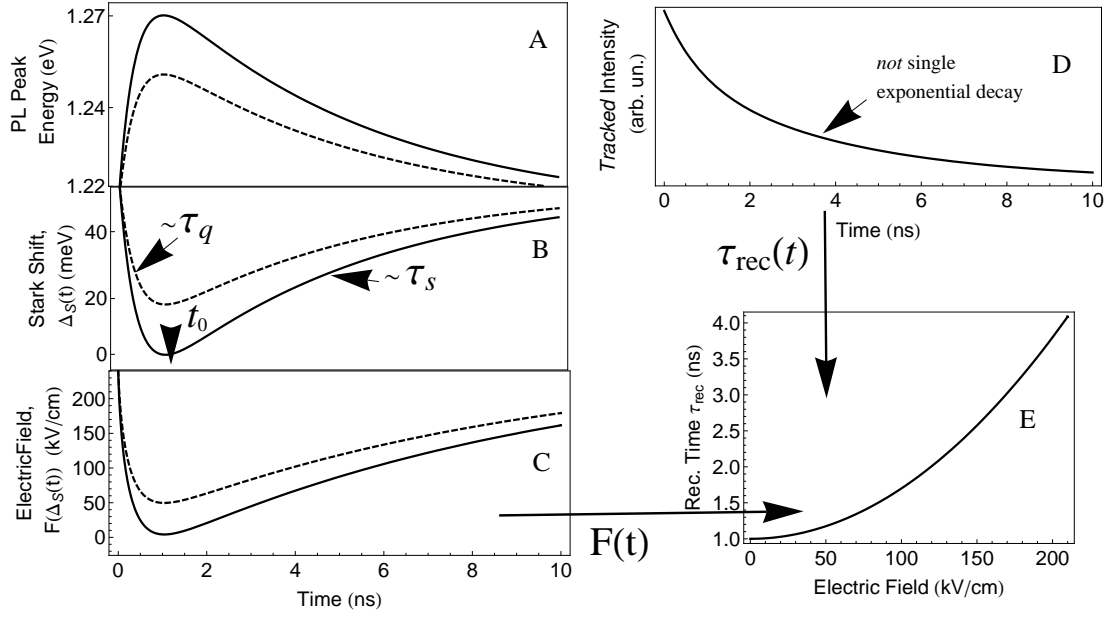


**Figure 5.1:** The left three panels show the schematic behavior of the position of the PL peak (A), Stark shift (B), and electric field (C) as a function of time. The model introduces a time-constant for the decrease of the Stark shift, denoted by  $\tau_q$ , and a recovery time-constant  $\tau_s$  when the minimum Stark shift at  $t = t_0$  has been passed. The electric field as a function of time (C), is combined with the time-dependent decay rates (D) to determine  $\tau_{rec}$  as a function of the electric field (E). The values in these schematic figures resemble the values in the actual experiment.

the recombination time as a function of the electric field (Fig. 5.1E). Our model neglects the energy dependence of the recombination time (within the bandwidth of 10 meV).

For a single exponential intensity decay of a quantum emitter (i.e., quantum dot in our case), with a radiative recombination time  $\tau_{rec}$ , one can write  $I(t) \sim e^{-t/\tau_{rec}}$ . The recombination time is found by differentiating the logarithm of the intensity:  $\frac{d(\ln I)}{dt} \sim \frac{1}{\tau_{rec}}$ . Since we ascribe the variation of the decay rates of the intensity to the electric field, we replace  $\tau_{rec}$  by  $\tau_{rec}(F(t))$ .

We approach the derivative  $\frac{d(\ln I)}{dt}$  with a numerical method of finite differences, for we obtain a finite set of data points for the tracked intensities. For the decay function  $I(t) = A \exp(-\frac{t}{\tau_{rec}(F(t))})$ , one can write  $\ln I(t) = \ln A + \frac{-t}{\tau_{rec}(F(t))}$ . The value of  $\ln I(t)$  after one time-step  $\Delta t$  can be written as  $\ln I(t + \Delta t) = \ln A + \frac{-t + \Delta t}{\tau_{rec}(F(t + \Delta t))}$ .

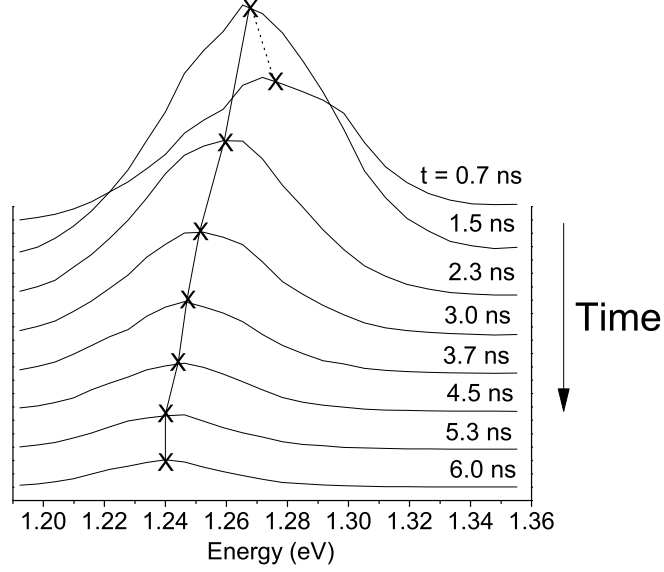


**Figure 5.2:** The raw PL intensity as a function of energy at different times. As time increases, the maximum of the PL peak shifts to lower energies.

Subtraction of these expressions yields

$$\ln I(t + \Delta t) - \ln I(t) = \frac{-t + \Delta t}{\tau_{rec}(F(t + \Delta t))} + \frac{t}{\tau_{rec}(F(t))}. \quad (5.1)$$

Since the difference of the electric field within the required measurement time  $\Delta t$  is small, we approximate the electric field to be constant *within* a time-step  $\Delta t^\dagger$ . Within the temporal resolution of the data of  $\Delta t = 110$  ps, the PL spectra exhibit a maximum Stark shift of  $\sim 1$  meV ( $\Delta F \sim 4.5$  kV/cm). Applying the assumption  $F(t) = F(t + \Delta t)$  to Eq. 5.1, one can write

$$\tau_{rec}(F(t)) = \frac{\Delta t}{\ln I(t + \Delta t) - \ln I(t)}. \quad (5.3)$$

We combine this expression with  $F(t)$  to determine  $\tau_{rec}(F)$ .

We approximate the time-dependence of the Stark shift with a single exponential behavior. In our PL spectra, it is possible to observe the (partial) quench of the built-in electric field in the Stark shift in the PL spectrum after arrival of the laser pulse,

<sup>†</sup>We make an error by omitting the chain rule in calculating  $\frac{d \ln I}{dt}$  in our analysis. The complete expression for  $\frac{d \ln I}{dt}$  can be written as

$$\frac{d \ln I(\tau(F(t)), t)}{dt} = -\frac{1}{\tau(F(t))} + \frac{t F'(t) \tau'(F(t))}{\tau(F(t))^2} \quad (5.2)$$

The last term is negligible when  $F'(t) \tau'(F) \ll \frac{\tau(F)}{t}$ . One can show *a posteriori* that this condition is fulfilled.

until the maximum Stark shift is reached. We characterize the initial behavior of the Stark shift, due to the electric field quench just after  $t = 0$ , by a time-constant  $\tau_q$ . This is shown in Fig. 5.1B. We will, however, not analyze  $\tau_q$  in great detail. After a minimum of the Stark shift at  $t = t_0$ , the Stark shift 'recovers' with a time-constant  $\tau_s$  (see Fig. 5.1B). The experiment reveals that the 'quenching' time-constant  $\tau_q$  is much smaller than the 'recovery' time-constant of the Stark shift,  $\tau_s$ . For the time-dependent Stark shift  $\Delta_S(t)$ , we can therefore write

$$\begin{aligned}\Delta_S(t) &= \Delta_0 e^{-\frac{t}{\tau_q}} \left(1 - e^{-\frac{(t-t_0)}{\tau_s}}\right) && \text{for } t > 0, \\ &\approx \Delta_0 \left(1 - e^{-\frac{(t-t_0)}{\tau_s}}\right) && \text{when } \tau_q \ll \tau_s, \text{ for } t > t_0,\end{aligned}\quad (5.4)$$

where  $\Delta_0$  denotes the maximum observed Stark shift in the applicable time range. The approximation in Eq. 5.4 is used for the functional dependence of the observed Stark shifts in time.

### 5.3 Results

Figure 5.3 shows two PL spectra up to 10 ns, where the spectra have been normalized by the value of the spectral peak intensity at every time-step. The panels in Fig. 5.3 show these spectra with decreasing excitation density from top to bottom, respectively  $12.1 \text{ mJ/cm}^2$  (Fig. 5.3A),  $8.4 \text{ mJ/cm}^2$  (Fig. 5.3B) and  $6.5 \text{ mJ/cm}^2$  (Fig. 5.3C). The figures show a dynamic Stark shift as a function of time. The electric field quench (observed in the Stark shift) becomes larger with increasing excitation density. This can be explained by a larger screening effect when the amount of photo-created charge carriers is larger. At  $t = 10 \text{ ns}$ , the Stark shifts in all panels of Fig. 5.3 have not yet saturated. Other PL data (not shown here), measured at excitation densities below  $4.5 \text{ mJ/cm}^2$ , reveal that the shift saturates at  $1.22 \text{ eV}$ . We associate this emission energy with the maximum built-in electric field of  $240 \text{ kV/cm}$ . Furthermore, we presented PL data with continuous wave excitation in Ch. 4, which indicates that the electric field can be compensated completely. A peak position of the PL of  $1.27 \text{ eV}$  is associated with this condition. Figure 5.3A shows that one, in fact, can compensate the electric field completely with pulsed excitation, since the PL peak reaches  $1.27 \text{ eV}$  at about  $1 \text{ ns}$ . Based on this observation, we apply  $t_0 = 1 \text{ ns}$  in Eq. 5.4 for the rest of our analysis. The extrema of the PL peak positions indicate that the Stark shift can reach up to  $50 \text{ meV}$  in this structure, which is not uncommon in (In,Ga)As quantum dots (Jin *et al.*, 2004; Wang *et al.*, 2006).

We determined the time-dependence of the peak position of the PL to establish the electric field as a function of time. Stark shifts were derived from the difference of



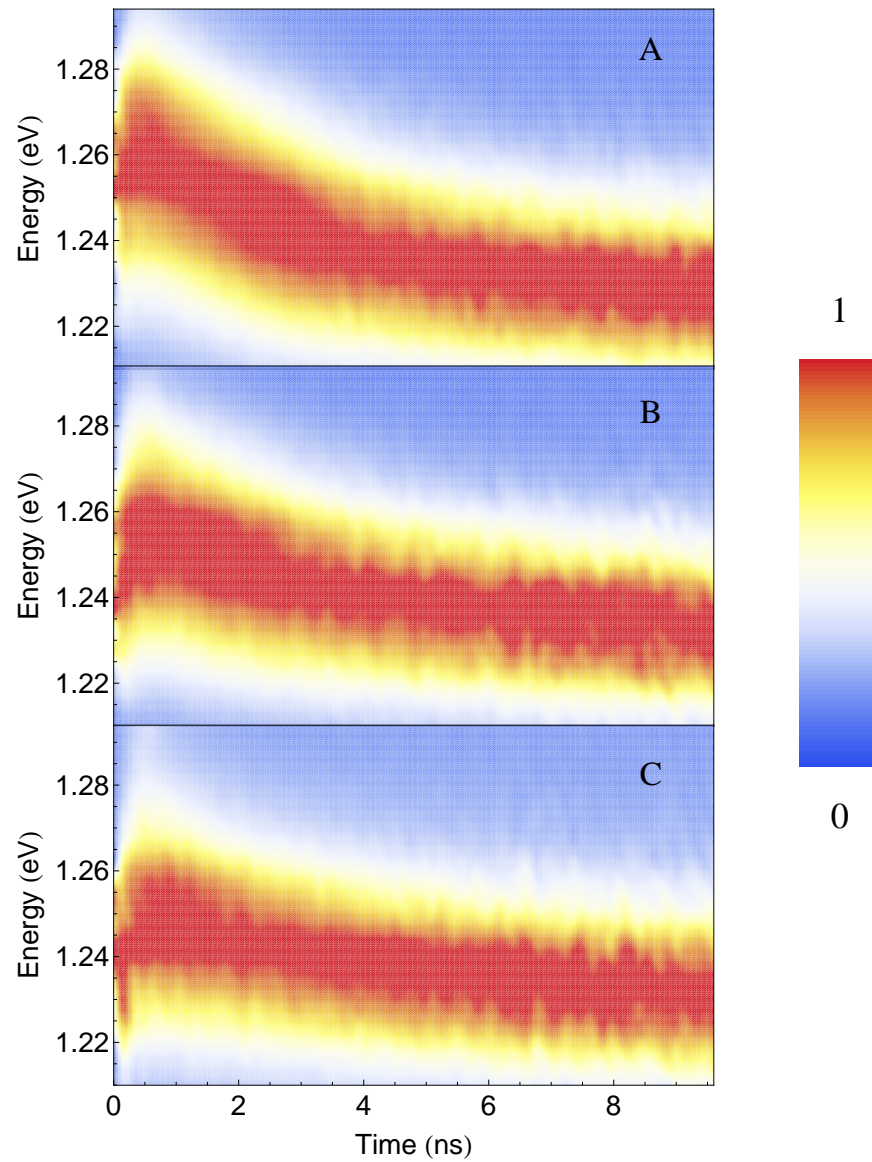


**Figure 5.3:** The dynamic Stark shift of the PL at  $12.1 \text{ mJ/cm}^2$  (A),  $8.484 \text{ mJ/cm}^2$  (B), and  $6.5 \text{ mJ/cm}^2$  (C).



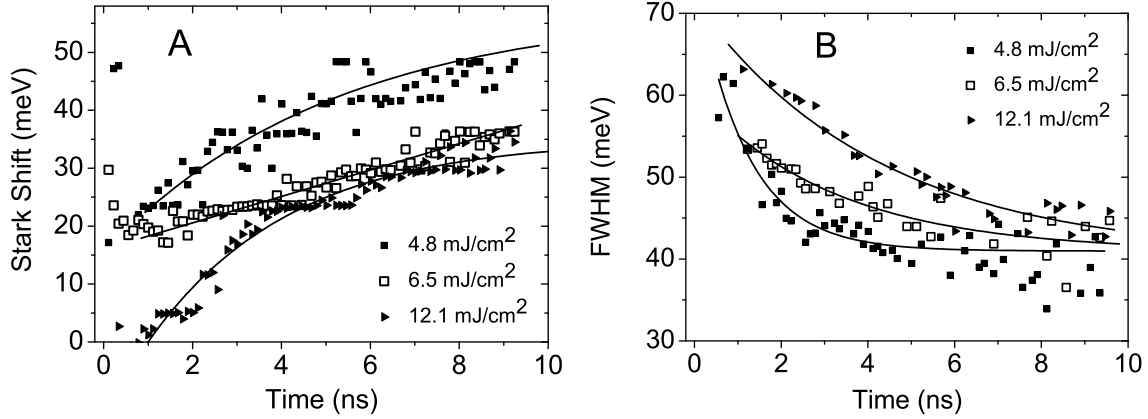


**Figure 5.4:** The Stark shift as a function of time depends on the excitation density of the laser. Figure A shows its dependence for 4.5 mJ/cm<sup>2</sup>, 6.5 mJ/cm<sup>2</sup> and 12.1 mJ/cm<sup>2</sup>. The functional dependence of the Stark shift is approximated with Eq. 5.4.

the peak position with 1.27 eV, associated with the completely quenched electric field. Figure 5.4 shows the Stark shift as a function of time for 4.8 mJ/cm<sup>2</sup>, 6.5 mJ/cm<sup>2</sup> and 12.1 mJ/cm<sup>2</sup>. The minimum Stark shift depends on the excitation density due to the screening effect. For example, at the minimum Stark shift at  $t = t_0$ , we observe a Stark shift of  $\sim 20$  meV at 4.8 mJ/cm<sup>2</sup>, whereas it is 0 meV (i.e., complete quench) at 12.1 mJ/cm<sup>2</sup>.

Besides the Stark shift, Fig. 5.3 shows a time-varying full width at half maximum (FWHM) as well, which is shown in Fig. 5.4B. The largest FWHM was found at the highest excitation densities, just after the laser pulse arrival, reaching almost 70 meV. The FWHM showed a decreasing trend in time for all excitation densities, which is possibly due to tunneling of charge carriers out of the quantum dot. Tunneling is neglected in our analysis. Since we only include data with  $t > 2$  ns, the FWHM varies at most 15 meV within the analyzed data set, which is still much smaller than the Stark shift.

From the time-dependence of the Stark shift, we are able to determine the time-constants  $\tau_q$  and  $\tau_s$  of Eq. 5.4 for every excitation density. For the quenching time  $\tau_q$ , only small differences were observed between the different excitation densities. This value was rather hard to determine since it was not always clear where to assign the peak in the spectra at  $t < t_0$ . On the material at hand, we crudely estimate  $\tau_q = 0.4 \pm 0.1$  ns for all the excitation densities. Note that the quenching is certainly not instantaneous with the laser pulse arrival. The values of  $\tau_s$  were determined by a fitting procedure with Eq. 5.4. For the high excitation density of 12.1 mJ/cm<sup>2</sup>, we find  $\tau_s = 3.3$  ns, whereas for 6.5 mJ/cm<sup>2</sup>, we find  $\tau_s = 8.6$  ns. Although there exists literature on the charge carrier dynamics in our (open-circuit) structure, we use these parameters as phenomenological

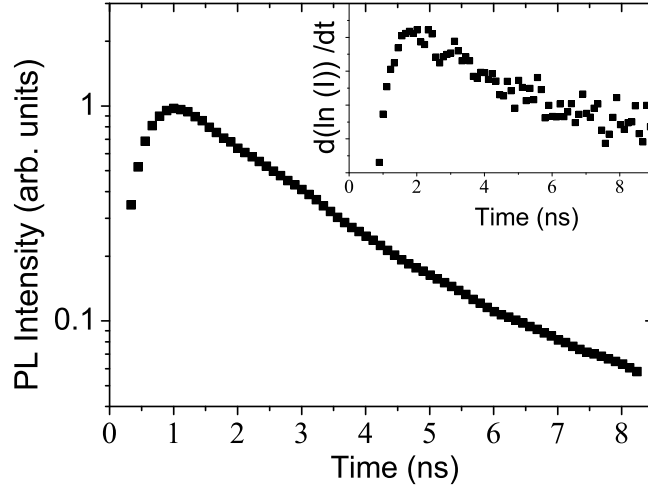
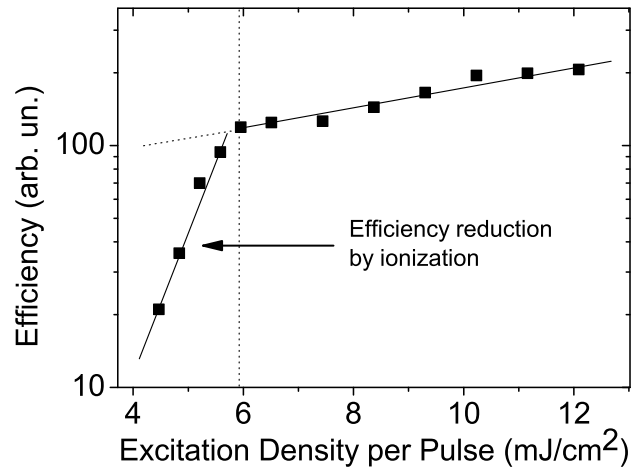


**Figure 5.5:** The tracked intensity as a function of time, not deconvoluted for the IRF (see Ch. 3), at an excitation density of  $12.1 \text{ mJ/cm}^2$ . The inset shows values for the time-dependent decay rate  $\frac{d \ln I}{dt}$ , approximated by Eq. 5.3.

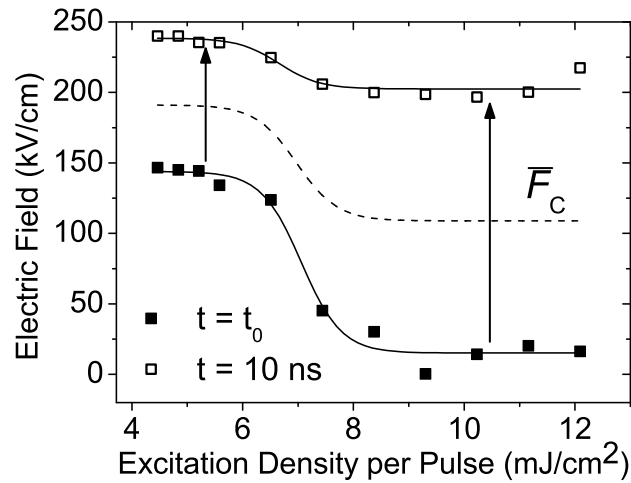
parameters and do not focus on the physics behind these characteristic times.

Figure 5.5 shows an example of the tracked intensity of the PL peak (which is not deconvoluted for the IRF, see Ch. 3), at the excitation density of  $12.1 \text{ mJ/cm}^2$ . The inset shows the finite difference approximation of the derivative  $\frac{d \ln(I)}{dt}$  (Eq. 5.3) as a function of time. We clearly observe a time-dependent decay rate. From the descending trend in the inset of Fig. 5.5, one can already determine the increasing trend of  $\tau_{rec}$  in time. Furthermore, large rise times are observed, exceeding 100 ps, which are associated with a dominating phonon-assisted relaxation between the levels in the quantum dot (Adler *et al.*, 1996). In our analysis, we employ a moving average procedure to these intensity profiles to reduce the noise level.

Figure 5.6 shows the efficiency of the luminescence process at several excitation densities. The efficiency is calculated by dividing the integrated tracked *output* intensity by the *input* excitation density of the pulsed laser. At low excitation density, the electric field remains large throughout the whole time range, and is not completely quenched. We propose that the electric field is high enough to induce cold ionization, i.e., tunneling of the charge carriers out of the quantum dot. Quite distinctively, the cold ionization strongly affects the intensity below a threshold excitation density of  $5.8 \text{ mJ/cm}^2$ , whereas the efficiency is nearly independent of the excitation densities above this threshold. The boundary at  $5.8 \text{ mJ/cm}^2$  is *not* associated with a higher occupation level of the quantum dot (i.e.,  $\bar{n} > 1$ ), since one would expect an *increasing* efficiency in that case. The data that is obtained below  $5.8 \text{ mJ/cm}^2$  is not included in the analysis of the electric field dependence of the recombination time.



**Figure 5.6:** The efficiency, defined as the output power (i.e., intensity) divided by the input power, as a function of the excitation density.



**Figure 5.7:** The minimum (■) and maximum (□) electric field within the measured period from 0 to 10 ns. The minimum of the electric field is reached approximately 1 ns after the laser pulse.

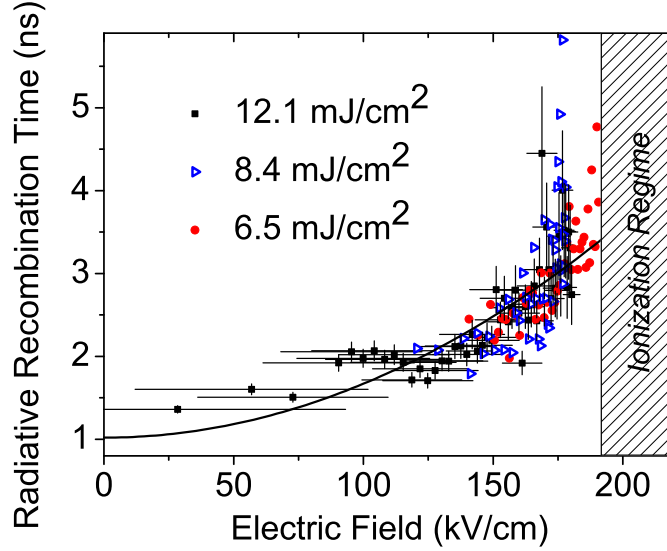


**Figure 5.8:** The recombination times as a function of the electric field, for the excitation densities  $6.5 \text{ mJ/cm}^2$ ,  $8.4 \text{ mJ/cm}^2$ , and  $12.1 \text{ mJ/cm}^2$ . Only the error bars of  $12.1 \text{ mJ/cm}^2$  are shown. The line shows a quadratic fit of the data,  $cF^2 + d$ , where  $c = 7.0 \times 10^{-6} \text{ ns/(kV/cm)}$  and  $d = 1.0 \text{ ns}$ .

The distinct threshold at  $5.8 \text{ mJ/cm}^2$  led us to investigate the range of electric fields at every excitation density. Figure 5.7 shows the lowest and highest electric field per laser pulse cycle as a function of the excitation density. Like in Fig. 5.6, we observe different behavior for excitation densities above and below  $\sim 6 \text{ mJ/cm}^2$ . Above the threshold of  $6 \text{ mJ/cm}^2$ , the electric field can not fully recover to its maximum built-in electric field of  $240 \text{ kV/cm}$ . Below  $6 \text{ mJ/cm}^2$ , the averaged electric field exceeds a critical value of  $\bar{F}_c = 190 \text{ kV/cm}$ . We associate this electric field as a threshold for cold ionization to occur. Therefore, the data with excitation densities below  $6 \text{ mJ/cm}^2$  is not incorporated in our final analysis of  $\tau_{rec}(F)$ . The quality of the data (i.e., signal-to-noise ratio) is also strongly reduced at electric fields above  $\bar{F}_c$ . Other authors find a critical electric field of  $\bar{F}_c \sim 120 \text{ kV/cm}$  in AlGaAs/GaAs quantum wells (Polland *et al.*, 1985) and (In,Ga)As quantum dots Fry *et al.* (2000a). Finley *et al.* (2004) finds a critical electrical field of  $\bar{F}_c \sim 150 \text{ kV/cm}$  for quantum dots. The difference between  $\bar{F}_c = 190 \text{ kV/cm}$  and the other experimental observations can be explained by the dependence of the tunneling rate on the quantum dot parameters (Fry *et al.*, 2000a), which was expressed in Eq. 1.13 in Ch. 2.

Figure 5.8 shows the dependence of the radiative recombination time on the electric field  $\tau_{rec}(F)$ . This plot shows data obtained for the excitation densities of  $12.1 \text{ mJ/cm}^2$ ,  $8.4 \text{ mJ/cm}^2$ , and  $6.5 \text{ mJ/cm}^2$ . To maintain a clear figure, only the error bars from the data at  $12.1 \text{ mJ/cm}^2$  is shown. The overlap between the data sets acts as additional support for the employed method. The radiative recombination time increases

monotonically with increasing electric field. Values for the recombination times  $\tau_{rec}$  range from 1.3 ns to 5.8 ns for electric fields from 30 kV/cm to 190 kV/cm. We find  $\tau_{rec} = 3.7 \pm 0.7$  ns for an electric field  $F \sim 190$  kV/cm, which is larger than the typical recombination times in quantum dots (Hours *et al.*, 2005; Bacher *et al.*, 1999). Electric fields above  $\overline{F}_c = 190$  kV/cm are associated with a dominant role of tunneling effects, which is denoted by the dashed area in Fig. 5.8. Few data points could be extracted for the lowest electric fields, since these could only be reached at 12.1 mJ/cm<sup>2</sup>.

## 5.4 Discussion

We associate the increasing recombination times in Fig. 5.8 with a *reduced overlap* between the conduction electron and valence electron wavefunction. One can approximate  $\tau_{rec}(F)$  by calculating the matrix elements with and without electric field:

$$\tau_{rec}(F) = \tau_0 \frac{|\int \Psi_c(F=0, \mathbf{r}) \Psi_v(F=0, \mathbf{r}) d\mathbf{r}|^2}{|\int \Psi_c(F, \mathbf{r}) \Psi_v(F, \mathbf{r}) d\mathbf{r}|^2}, \quad (5.5)$$

where  $\tau_0$  is the recombination time at  $F = 0$  kV/cm. The  $\Psi_c(F, \mathbf{r})$  and  $\Psi_v(F, \mathbf{r})$  represent the wavefunction in a  $\mathbf{r}$ -representation of the conduction and valence electron, respectively, as a function of the electric field  $F$ . In the case of a reduced overlap between the wavefunctions  $\Psi_c$  and  $\Psi_v$ , the denominator in Eq. 5.5 decreases and  $\tau_{rec}$  increases.

We approximate the electric field dependence only to affect the growth direction ( $z$ -direction) of the wavefunction. We therefore denote the trial wavefunction  $\Psi_{c,v} = f(x, y) \exp[-(\frac{z}{z_0})^2]$ , where  $z_0$  is measure of (half) the height of the quantum dot. Moreover, we approximate the electric field to induce a linear peak-shift in the  $z$ -direction with increasing electric field. The conduction and valence electron exhibit a different dependence on the electric field, respectively denoted by  $\Psi_c(F) = f(x, y) \exp[-(\frac{z-\alpha F}{z_0})^2]$  and  $\Psi_v(F) = f(x, y) \exp[-(\frac{z-\beta F}{z_0})^2]$ . The integral in 5.5 can therefore be written as

$$\begin{aligned} \tau_{rec}(F) &= \tau_0 \frac{|\int \exp[-2(\frac{z}{z_0})^2] dz|^2}{|\int \exp[-(\frac{z-\alpha F}{z_0})^2] \exp[-(\frac{z-\beta F}{z_0})^2] dz|^2} = \tau_0 \exp\left[\frac{(\alpha + \beta)^2 F^2}{z_0^2}\right] \\ &= \tau_0 \left(1 + \frac{(\alpha + \beta)^2 F^2}{z_0} + O(F^4)\right) \quad (5.6) \\ &= d + cF^2 + O(F^4) \quad (5.7) \end{aligned}$$

where we have applied a Taylor expansion in the approximation. Such an expansion is valid as long as  $(\alpha + \beta)^2 F^2 \ll z_0^2$ . Note that the dependence for the Stark shift contains a quadratic term as well. In this sense, the Stark shift can be used as a measure

for the recombination time ( $\tau(\Delta_s) \sim \Delta_s + O(\Delta_s^2)$ ), if one assumes a purely quadratic dependence,  $\Delta_s \sim F^2$ .

The quadratic approximation  $\tau_{rec}(F) = cF^2 + d$  from Eq. 5.7 is used to extrapolate the value of the recombination time at  $F = 0$  kV/cm. A fitting procedure yields  $c = (7.0 \pm 0.3) \times 10^{-6}$  ns/(kV/cm)<sup>2</sup> and  $d = 1.0 \pm 0.2$  ns. We therefore write  $\tau_{rec} = 1.0 \pm 0.2$  ns at  $F = 0$  kV/cm. Note that the approximation is only valid for electric fields below 190 kV/cm.

If we assume  $\alpha = \beta$  for the moment, we can determine  $\alpha$  from the exact Taylor expansion in Eq. 5.6. The parameter  $\alpha$  is, in fact, a measure for the polarizability of the peak of the electron-hole pair, which depends both on the shape of the potential of the quantum dot as on the mass of the charge carrier (i.e., band structure of the material). Employing  $\alpha = \beta$  in Eq. 5.6, we find  $\alpha = z_0 1.9 \times 10^{-3}$  m/(kV/cm). Our quantum dots have  $z_0 \sim 3$  nm, and therefore  $\alpha = 5.7 \times 10^{-12}$  m/(kV/cm). The induced dipole (equivalent to  $\beta F$ ) at an electric field of 100 kV/cm would be  $p = 11.4$  eÅ, more than twice as large as 5.5 eÅ, observed by Hsu *et al.* (2001). However, Hsu *et al.* (2001) investigate quantum dots with a height of 4 nm, corresponding to  $z_0 = 2$  nm. The smaller height results in a smaller dipole moment.

From the parameter  $\alpha$ , we can determine the position of the peak of the wavefunction at the critical electrical field  $\bar{F}_c$ , denoted by  $z_c$ , and find  $z_c = \alpha \bar{F}_c = 1.1$  nm. The value  $z_c$  shows that tunneling effects become dominant when the peak position has shifted a fraction ( $z_c/z_0$ )  $\sim 0.36$  of the total height of the quantum dot. Note that the condition  $2\alpha^2 \bar{F}_c^2 = 2z_c^2 \ll z_0^2$  is still fulfilled for this ratio, such that the Taylor expansion is still valid.

This study shows that control over the recombination time is possible, like in quantum wells, by controlling the overlap of the electron and hole wavefunctions. For applications in quantum information devices, the  $\sim 4$  ns of 'operation time' might not be sufficient. A design where one of the charge carriers is ionized, applied by Kroutvar *et al.* (2004), could be a solution to extend recombination times further.



# Time-Resolved Kerr rotation spectroscopy on (In,Ga)As quantum dots

## ABSTRACT

This chapter presents time-resolved Kerr rotation measurements on a single layer of unannealed self-assembled (In,Ga)As quantum dots, performed in collaboration with the 'Physics of Nanostructures' group at the Eindhoven University of Technology. The single layer of (In,Ga)As quantum dots is embedded in a *p-i-n* structure, resulting in a built-in electric field in the growth direction. This system allows us to investigate the absolute values of the *in-plane*  $g$  factors of these quantum dots, as well as its electric field dependence. Control over the electric field is achieved by an additional continuous wave HeNe laser, which photo-created charge carriers screen the built-in electric field of the *p-i-n* structure. The Kerr rotation data shows precession of the spin due to an in-plane magnetic field. A single main frequency is observed, which is assigned to the spin precession of the valence electron. This assignment is based on calculations of J.A.F.S. Pingenot and M.E. Flatté. They show that the substantial elongation of the footprint of the quantum dots, determined in AFM measurements, leads to strong intermixing of the heavy and light hole states, which is required for the valence electron in-plane  $g$  factor to be larger than the conduction electron in-plane  $g$  factor (Pryor and Flatté, 2006, 2007). The absolute value of the in-plane  $g$  factor of the valence electron,  $|g_{v,\parallel}|$ , is found to be  $0.42 \pm 0.01$ . In electric fields of the order of  $F \sim 50$  kV/cm and higher, the  $g$  factor marginally increases. These observations of the precession are in fair agreement with similar measurements on the same sample structure, published by Rietjens *et al.* (2008), except that Rietjens *et al.* (2008) assign the precession to originate from the conduction electron. Values for the conduction



electron spin decoherence time  $T_{2,c}^*$ , of the order of 800 ps, are consistently found to be larger than the valence electron spin decoherence time  $T_{2,v}^*$  of about 450 ps. Whereas the valence electron spin decoherence time  $T_{2,v}^*$  strongly decreases in electric fields, the conduction electron spin decoherence time  $T_{2,c}^*$  appears to be independent of the electric field.

## 6.1 Introduction

It is interesting to achieve control over the  $g$  factors in nanostructures, particularly quantum dots, because of the application of such nanostructures in quantum computation (Kane, 1998). Proposed geometries employ a static magnetic field, on which RF pulses can be superimposed to perform operations on the spin of localized charge carriers. To achieve control over the spin of charge carriers in *individual* impurities or quantum dots, one should have control over the  $g$  factor. Such can be realized by static electric fields (Kane, 1998). Since the sensitivity of the  $g$  factor to an electric field can be crucial for the choice for certain quantum computer geometry or architectures, it is worthwhile studying the electric field dependence for both the in-plane and the growth direction  $g$  factor. Whereas chapter 4 has focussed on  $g$  factors in the growth direction, this chapter focusses on in-plane  $g$  factors. We measure the spin precession, which frequency is proportional to the in-plane  $g$  factor, by a time-resolved Kerr rotation technique.

In the last decade, Kerr rotation spectroscopy has been mostly used for the study of thin film structures of metals (Katayama *et al.*, 1993; Mégy *et al.*, 1995; Koopmans *et al.*, 1995). The advancement into time-resolved studies of semiconductor quantum wells (Koopmans and de Jonge, 1999; Salis *et al.*, 2001; Camilleri *et al.*, 2001) and quantum dots (Gupta *et al.*, 1999; Kanno and Masumoto, 2006), has revealed, among others, electrically-controllable  $g$  factors in quantum wells (Salis *et al.*, 2001) and a generally wide range of spin decoherence times for such nanostructures. After a study of electrically-controllable  $g$  factors in (Al)GaAs quantum wells (Salis *et al.*, 2001) and bulk GaAs semiconductor material (Kato *et al.*, 2003), this study treats (In)GaAs quantum dots. Whereas the aforementioned literature results determine the control of the conduction electron  $g$  factor, the precession in this study is likely due to the valence electron. This has been indicated by recent calculations of J.A.F.S. Pingenot and M.E. Flatté.

In chapter 3, we discussed how a spin imbalance in a solid state material can induce a rotation in the polarization of a linearly polarized beam, known as the Kerr rotation  $\theta_K$ . The goal in this chapter is to investigate whether the in-plane  $g$  factor and decoherence times  $T_2^*$  are dependent on an electric field in the growth direction of the structure. Like the experiments discussed in Ch. 4 and Ch. 5, the built-in electric field of the  $p-i-n$  structure is varied by the laser excitation density. Since we apply a time-resolved optical pump-probe technique, we employ an additional *continuous wave* He:Ne laser to vary the electric field. The Stark shift in the PL spectra serves as a measure for the electric field over the quantum dots. Two series of data have been taken: one *with* and an other *without* magnetic field. Both series cover the time-resolved decay of the Kerr rotation  $\theta_K(t)$  at various He:Ne excitation densities (i.e., electric fields over the quantum dots).

We recall some of the equations for the two-level spin system as an introduction to

the model. For a spin system with a static magnetic field pointing in the  $z$ -direction, there exist the longitudinal spin relaxation time  $T_1$  and (in-plane) decoherence time  $T_2$ . The  $T_1$  is associated with emission of acoustic phonons, whereas the  $T_2$  describes the timescale of the detrimental effects of the environment on the coherence of the states. A  $T_2^*$  appears in the (experimental) literature as well, which incorporates the spatially inhomogeneous properties of the quantum dots (like the  $g$  factor and the experienced nuclear magnetic field) within the quantum dot ensemble in the probing laser spot.

In the case of a static magnetic field in the  $z$ -direction, the spin dynamics can be described by the Bloch equations (see for example Blum (1981)),

$$\dot{S}_x = \omega S_y - \frac{S_x}{T_2} \quad (6.1)$$

$$\dot{S}_y = \omega S_x - \frac{S_y}{T_2} \quad (6.2)$$

$$\dot{S}_z = \frac{S_{z,eq} - S_z}{T_1}, \quad (6.3)$$

where  $S_{z,eq}$  is the equilibrium value of the magnetization. Note that Eq. 6.1 and Eq. 6.2 for the in-plane components  $S_x$  and  $S_y$  are coupled, but that Eq. 6.3 for the longitudinal component  $S_z$  is uncoupled. The in-plane spin projections process with the (Larmor) frequency  $\omega = \frac{|g_{\parallel}|\mu_B B}{\hbar}$ , where  $|g_{\parallel}|$  is the absolute value of the in-plane  $g$  factor. The solutions to Eq. 6.1–6.3 are (Blum, 1981)

$$\begin{aligned} S_x(t) &= A \sin(\omega t + \phi) e^{-\frac{t}{T_2^*}} \\ S_y(t) &= A \cos(\omega t + \phi) e^{-\frac{t}{T_2^*}} \\ S_z(t) &= (B - S_{z,eq}) e^{-\frac{t}{T_1}} + S_{z,eq}, \end{aligned} \quad (6.4)$$

where  $A$ ,  $B$  and  $\phi$  are constants.

## 6.2 Model

In the experiment, we prepare the spin of the electron and hole to be orthogonal to the magnetic field direction (Voigt geometry). A scheme of the geometry is shown in Fig. 6.1. Absorption of a photon leads to *anti-parallel* alignment of the conduction electron spin with the angular momentum vector of the photon. The spin of the valence electron is aligned *parallel* with the angular momentum vector upon absorption of the photon. In general, the electron spin state can be written as a linear combination of the eigenstates  $|\uparrow\rangle$  and  $|\downarrow\rangle$  with a relative phase difference  $\delta$  between the states:  $\frac{1}{\sqrt{2}}(|\uparrow\rangle + e^{i\delta}|\downarrow\rangle)$ . In a magnetic field, the state will precess due to a difference in energy of both eigenstates,

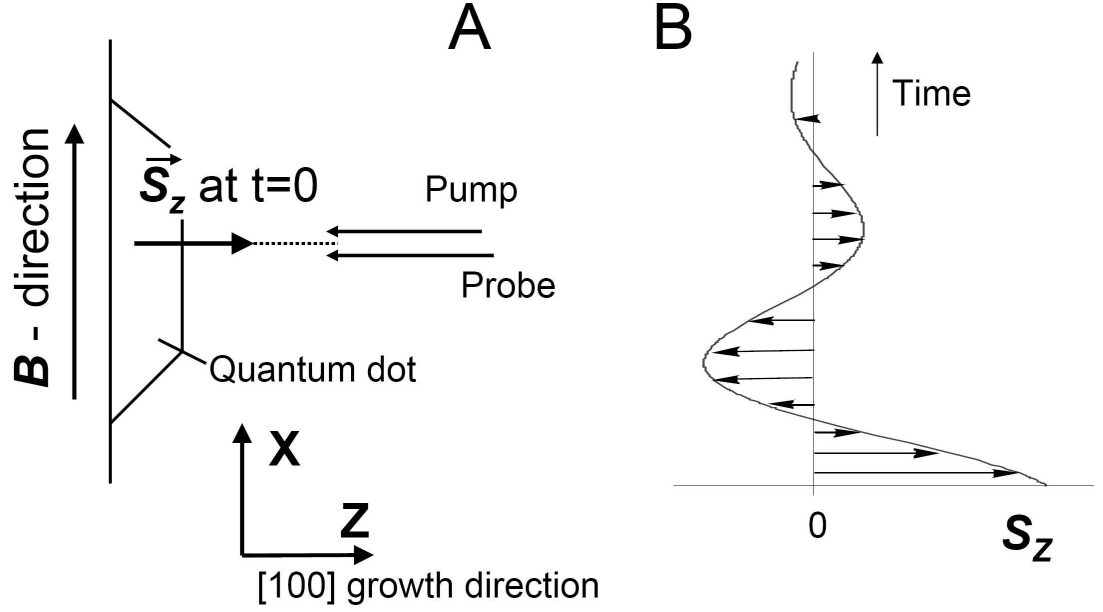


**Figure 6.1:** Figure A shows a side-view (on the  $x$ - $z$  plane) of the sample, where the magnetic field is directed orthogonal to the optically prepared spin. Precession of the spin occurs in the plane *orthogonal* to the magnetic field direction ( $x$  direction). The angle of the magnetic field, relative to the  $[110]$  and  $[1\bar{1}0]$  direction, is not recorded. Oscillatory behavior of the  $z$  component of the spin vector,  $S_z$ , in time, is shown schematically in Fig. B.

which is described by Eqs. 6.4. The precession can be monitored via the Kerr rotation of a linearly polarized probe beam.

The spin state is prepared with a pulsed circularly polarized beam at 82 MHz, at an energy of 1.335 eV and a linewidth of  $\sim 15$  meV. This energy corresponds to the high energy side of the quantum dot PL spectrum, which is shown in Fig. 4.4. The transitions at these energies consist of ground state transitions of small quantum dots, and possibly some excited states or wetting layer states from larger quantum dots. Relaxation from excited states to the ground states can occur within the measuring time of  $\sim 1$  ns after excitation. Such relaxation behavior can be different for the conduction and valence electron.

One should note that when the probe beam is at a different energy than the transition energy  $E_{tr}$  of the exciton, one can still observe a Kerr rotation (Bennemann, 1998). Denoting the energy of the laser by  $E$ , the Kerr rotation intensity is proportional to  $\sim (E - E_{tr})^{-1}$ , whereas the absorption decays as  $\sim (E - E_{tr})^{-2}$ . Since the absorption decays more strongly than the Kerr rotation intensity, it is possible to probe the spin with negligible absorption of photons. This property is for example cleverly exploited by Berezovsky *et al.* (2006), to perform a 'non-demolition' measurement on a single spin in a quantum dot.

The laser excitation pulse at 1.335 eV creates a conduction and valence electron in the quantum dot at a pump excitation density of  $2 \text{ kW/cm}^2$  (which equals  $24 \mu\text{J/cm}^2$  per pulse at 82 MHz). This excitation density yielded the largest contrast between the Kerr rotation signals under He:Ne laser excitation and without He:Ne laser excitation. The probe excitation density, on the other hand, is approximately 3 times smaller,  $P_{probe} \sim 700 \text{ W/cm}^2$  (i.e.,  $8 \mu\text{J/cm}^2$ ). The excitation densities of the pump and probe beam are high compared to the He:Ne excitation density range of  $25 \text{ W/cm}^2 < P_{HeNe} < 130 \text{ W/cm}^2$ . One should note, however, that only a small fraction of the pump pulse is converted into electron-hole pairs, since absorption of the pump beam is limited by a Pauli blockade: when there are no more states available in the energy width of the laser, no more absorption takes place. Although the excitation densities of the He:Ne laser are lower, a situation where  $\bar{n} > 1$  is still likely to be caused by this laser, since it excites *above* the GaAs bandgap. While we had an upper boundary of  $\bar{n} = 1.6$  for  $P_{HeNe} = 50 \text{ W/cm}^2$  in Ch. 4, in this chapter, we greatly surpass this excitation densities. Therefore, one can expect a condition with multiple excitons in the quantum dot ( $\bar{n} > 1$ ) at the highest excitation densities.

The oriented spins of the electron-hole pair induce a linear Kerr rotation of the probe beam. This signal decays in time due to both a conduction electron spin decoherence time  $T_{2,c}^*$  and valence electron spin decoherence time  $T_{2,v}^*$ . While in principle, one should be able to distinguish between the  $T_2$  decay of the conduction and valence electron, in practice, we do not observe such a multi-exponential decay. We therefore use a single magneto-optical decay time  $T_{MO}$  to describe this behavior, extracted from  $\theta_K(t) \sim e^{-\frac{t}{\tau_{rec}} - \frac{t}{T_{MO}}}$ . We have included the recombination time of the electron-hole pair in this signal decay, which is similarly applied to all models in this chapter.

Tunneling of electrons out of the quantum dot would also lead to additional reduction of the signal, but this is not incorporated in the models. We assume such effects to be negligible for the electric fields which appear in these measurements ( $F < 130 \text{ kV/cm}$ ), and solely use the recombination time at zero electric field as input parameter. Tunneling is likely to be an important cause for the loss of signal at higher electric fields.

The first series of experiments were aimed to determine  $T_{MO}$  for the quantum dots at different excitation densities of the He:Ne laser. In the later series, an additional magnetic field was applied to observe the precession of the spin in the quantum dots.

From Kerr rotation signals induced by an electron-hole pair in a quantum confined structure, it is impossible to distinguish between the conduction electron and valence electron precession. Based on assumptions, however, the precessing of the Kerr rotation signal in measurements on III-V quantum wells has been commonly attributed to the conduction electron (Crooker *et al.*, 1996; Kennedy *et al.*, 2006; Chen *et al.*, 2007;

Zhukov *et al.*, 2007). This is a fair assumption when there is little heavy/light hole intermixing in the valence band. In that case, the direction of the angular momentum of the (predominantly) heavy holes is rigidly directed and orthogonal to the magnetic field vector. This geometry *and* the strong coupling between the angular momentum and spins of the heavy holes results in very small Zeeman splittings in a magnetic field.

In the case of a large elongation of the footprint of the quantum dot, however, strong intermixing between the heavy and light hole occurs. Pryor and Flatté (2006) have shown that the absolute values of the valence electron in-plane  $g$  factor ( $|g_{v,\parallel}|$ ) can exceed the conduction electron  $g$  factor ( $|g_{c,\parallel}|$ ) several times for strongly elongated geometries. Since the footprint of our quantum dots has an elongation ratio of 1.6, as determined by AFM measurements, we expect the valence electron  $g$  factor to be larger than the conduction electron  $g$  factor. The ratio between the valence electron and conduction electron in-plane  $g$  factor is maximal at transition energies near  $\sim 1.30$  eV (Pryor and Flatté, 2006), where our quantum dots have their optical transition energy. Because there is no experimental way to distinguish between the precessing of a conduction and valence electron in our measurement, we assume in this study that the highest beating frequencies are arising from the valence electron. We thus assume to probe  $|g_{v,\parallel}|$ . Moreover, the exact in-plane magnetic field direction, relative to the orientation of the crystal, was not recorded. We can therefore not distinguish between the  $g$  factor in the  $[110]$  and  $[1\bar{1}0]$  direction.

An example of how our signal is built up is shown schematically in Fig. 6.2. Both the conduction and valence electron contribute equally to the Kerr rotation, therefore, the signal is built-up from a (nearly) equal amplitude  $A$  and  $B$  for, respectively, the valence and conduction electron. A different relaxation mechanism for the conduction and valence electron can lead to lower amplitudes of one charge carrier. From the oscillation frequency  $\omega$  of the valence electron, one can determine  $|g_{v,\parallel}|$  by  $\omega = \frac{|g_{v,\parallel}|\mu_B B}{\hbar}$ .

In this chapter, we apply two models to analyze the data. Model 1 can be considered a balanced model, where the contributions of the conduction electron and valence electron are set equal. In Model 2, we relax the condition of the strictly equal amplitudes for the conduction and valence electron by two different amplitudes for the conduction and valence electron.

Model 1 implies that the oscillatory and non-oscillatory part of the signal have the same amplitude  $A$ . Such a signal can be described as (Chen *et al.*, 2007; Rietjens *et al.*, 2008)

$$\theta_K(t) = A \cos(\omega t) e^{-\frac{t}{\tau_{rec}} - \frac{t}{T_{2,v}^*}} + A e^{-\frac{t}{\tau_{rec}} - \frac{t}{T_{2,c}^*}} + D, \quad (\text{Model 1}) \quad (6.5)$$

where we have included the radiative recombination time  $\tau_{rec}$  in the exponential decays due to decoherence. We employ the recombination time values of Ch. 5 for  $\tau_{rec}$  and fit

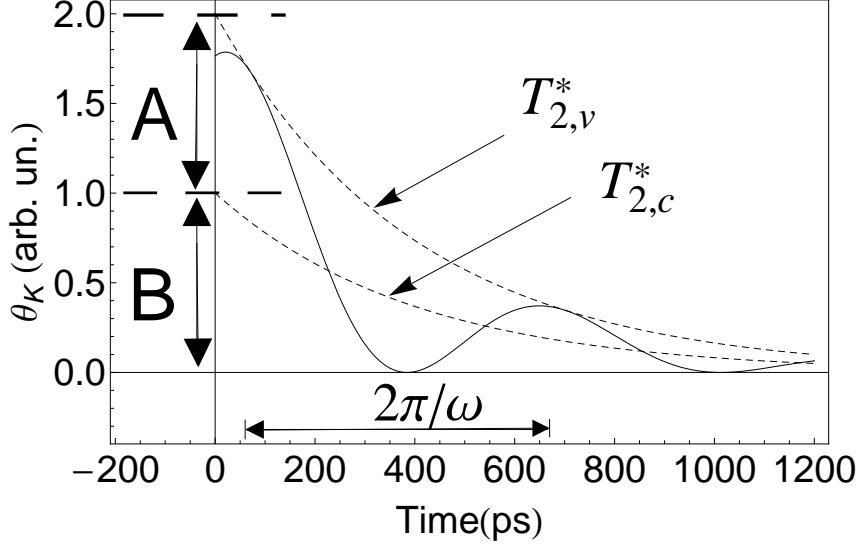


**Figure 6.2:** This figure shows a calculated signal (continuous line), containing a component from the conduction electron and valence electron. The exponential decays of the conduction electron and valence electron signal are displayed with a dashed line. The signal of the valence electron, with an amplitude  $A$ , contains an oscillatory part and a decoherence time  $T_{2,v}^*$ . The precession of the conduction electron is neglected. It only contains an exponential decoherence term ( $T_{2,c}^*$ ), with an amplitude  $B$ .

the 5 parameters values  $\omega$ ,  $T_{2,c}^*$ ,  $T_{2,v}^*$  and the amplitudes  $A$  and  $D$ . The term  $D$  is a background term. Note that the oscillatory behavior is attributed only to the valence electron.

To enhance the flexibility of Model 1, we relax the condition that the amplitude  $A$  should apply to both the conduction and valence electron, but rather ascribe them to have an independent amplitude  $A$  and  $B$ . A physical origin of this could be the different cascaded decay process between excited and ground states for the conduction and valence electron, occurring within their decoherence time. The complete signal can be written as (Chen *et al.*, 2007; Zhukov *et al.*, 2007)

$$\theta_K(t) = A \cos(\omega t) e^{-\frac{t}{\tau_{rec}} - \frac{t}{T_{2,v}^*}} + B e^{-\frac{t}{\tau_{rec}} - \frac{t}{T_{2,c}^*}} + D, \quad (\text{Model 2}) \quad (6.6)$$

where we fit the values for the 6 independent parameters  $\omega$ ,  $T_{2,e}^*$ ,  $T_{2,v}^*$ ,  $A$ ,  $B$ , and  $D$ .

The radiative recombination time  $\tau_{rec}$  has been determined in the time-resolved PL measurements, as discussed in Ch. 5. During all the fitting procedures in this chapter, the recombination time is set 1 ns. The electric field dependence of the recombination time is not included, since implementation of such frequently resulted in erroneous fits.

The fitting process is a least-squares fit. We have included the data points from  $t = 20$  ps to  $t = 1200$  ps. Based on the signal-to-noise ratio in time, we have weighted

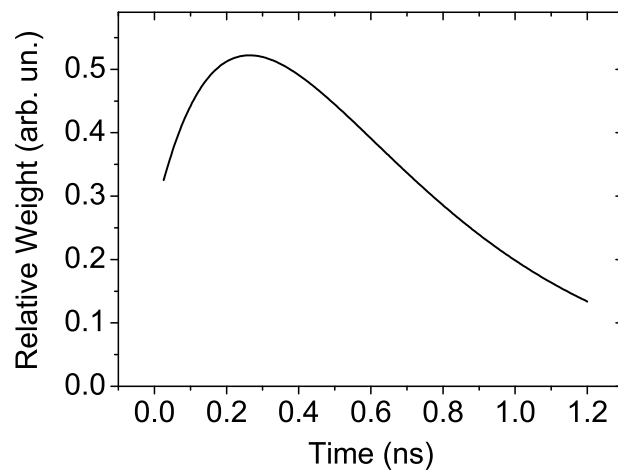


**Figure 6.3:** The relative weight of the data points as a function of time. The highest weights are attributed to the data points near  $t = 0.3$  ns, where the signal-to-noise ratio is high.

the data points following a function shown in Fig. 6.3. The points which exhibit the lowest signal-to-noise ratio, occurring in the time-frame between 0.2 ns and 0.4 ns, have the largest weight.

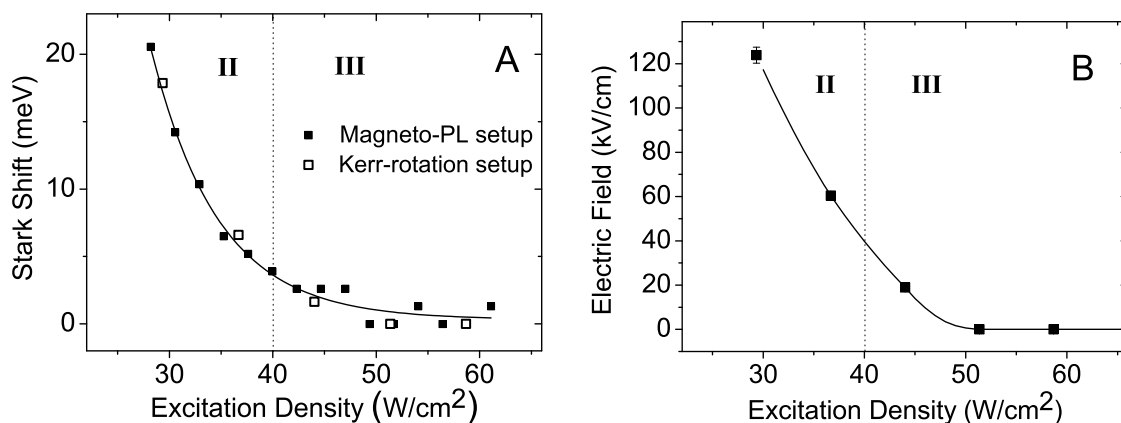


### 6.3 Results

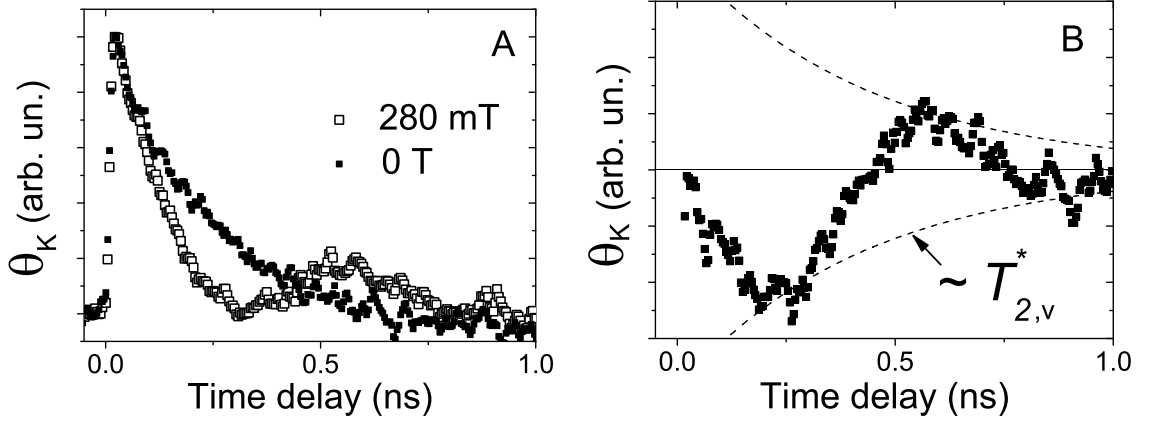
First of all, we measured the Stark shift in the PL spectra by varying excitation density of the He:Ne laser. Figure 6.4A shows the Stark shift which was measured both in the magneto-optical PL setup and the Kerr-rotation setup. The data of the magneto-optical PL setup coincide with the Stark shift data discussed in Ch. 4. We note that there is significant uncertainty in the spot sizes of both setups. Since the shape of both curves is the same, it appeared reasonable to match the excitation densities of the Kerr-rotation setup with that of the magneto-PL setup, which is done in Fig. 6.4A. Like in Ch. 4, we use the Roman I, II and III to indicate the regimes of the Stark shift. The sensitivity of the detection track for the PL on the Kerr-rotation setup is lower, hence, we do not observe a Stark shift above 20 meV.

Figure 6.4B shows the electric fields associated with this Stark shifts, when we apply the quadratic equation  $\Delta_S = \beta F^2 + pF$  for the Stark shift. A similar procedure has been applied in Ch. 4. The electric fields do not exceed 130 kV/cm. We have taken  $\beta = (5.5 \pm 0.5) \times 10^{-4} \text{ meV}/(\text{kV}/\text{cm})^2$  (Hsu *et al.*, 2001) and the built-in dipole moment  $p = 7.6 \times 10^{-2} \text{ meV}/(\text{kV}/\text{cm})$ . These parameters give a Stark shift of 39 meV at 240 kV/cm, which matches with the data of Ch. 4.

An example of a time-resolved Kerr rotation spectroscopy measurement, both with and without magnetic field, is shown in Fig. 6.5A. This figure is an example of a measurement obtained at high excitation density ( $\sim 100 \text{ W}/\text{cm}^2$ ) of the He:Ne laser. The precession measurements are limited by a maximum magnetic field of 280 mT. We observe only one well-distinguishable period of the precession. Figure 6.5B shows an



**Figure 6.4:** The Stark shifts in Fig. A show the same behavior as a function of excitation density of the He:Ne laser in the magneto-PL setup (■) and Kerr-rotation setup (□). The corresponding electric fields, deduced from  $\Delta_S = \beta F^2 + pF$  (where  $\beta = 5.5 \times 10^{-4} \text{ meV}/(\text{kV}/\text{cm})^2$  and  $p = 7.6 \times 10^{-2} \text{ meV}/(\text{kV}/\text{cm})$ ), are shown in Fig. B.



**Figure 6.5:** The Kerr rotation  $\theta_K$  as a function of time, in the case of a compensating CW He:Ne laser at high excitation density ( $\sim 100 \text{ W/cm}^2$ ), without magnetic field ( $\blacksquare$ ) and with a magnetic field of 280 mT ( $\square$ ). To highlight the spin precession of the valence electrons, we show the data after subtraction of an exponential decay with time-constant  $T_{MO}$  in Fig. B.

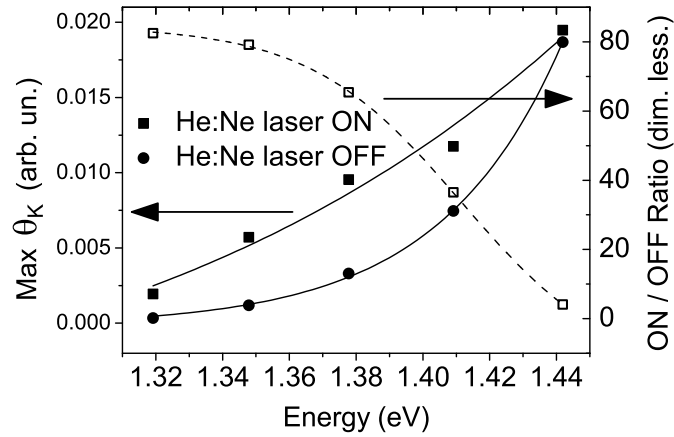


**Figure 6.6:** The solid data points, corresponding the left axis, show the maximum Kerr rotation  $\theta_K(t)$ , measured just after  $t = 0$  (see Fig. 6.5A), either *with* ( $\blacksquare$ , excitation density  $\sim 100 \text{ W/cm}^2$ ) or *without* ( $\bullet$ ) compensation by the He:Ne laser. The ratio between these maxima, denoted by ON/OFF ratio on the right axis ( $\square$ , dashed line), increases from 4 to above 80 for decreasing energies. Since the quantum dots have energies below 1.35 eV, this curve indicates a contribution of the quantum dots to the Kerr rotation signal.

example of the signal where a smoothed exponential decay has been subtracted. Spin precession is clearly visible and has a damping-timescale ( $\sim T_{2,v}^*$ ) of 400 to 500 ps.

Before we continue with the Kerr rotation data, we comment on the origin of the Kerr rotation signal. Since there exist free-to-bound (deep) acceptor transitions at the energies  $\sim 1.33$  eV, the probed Kerr rotation could also be induced by spins of these impurity states. If we assume that the properties of the free-to-bound acceptor transitions are energy-independent below the main acceptor peak at 1.47 eV, these optical transitions can be discarded as an origin of the Kerr rotation signal, since,

- First of all, Fig. 6.6 shows that at the quantum dot energies below  $\sim 1.36$  eV, the contrast (i.e., the ratio of the maximum Kerr rotation signal with and without HeNe laser, labeled 'ON/OFF ratio' in Fig. 6.6) of the Kerr rotation signal increases. The free-to-bound transitions can not induce this increase in contrast. Instead, we assign this increase to the quantum dots, since the energies of their optical transitions occur in this region.
- Secondly, measurements of the radiative recombination time for the free-to-bound acceptor transitions between 1.35 – 1.45 eV revealed a quick radiative recombination ( $\tau_{rec} < 300$  ps) compared to the decay of our magneto-optical signal. Since we observe  $\tau_{rec} > 300$  ps, the signal in our measurements should be due to the quantum dots.
- Finally, the magneto-optical decay time  $T_{MO}$  is much smaller for the free-to-bound acceptor transitions. One does expect the decoherence time to be shorter in a bulk type environment, due to more pronounced decoherence mechanisms like the Bir-Aharonov-Pikus mechanism. In  $p$ -type doped GaAs, where  $p = 5 \times 10^{18} \text{ cm}^{-3}$ , the spin decoherence time would be  $T_{2,c}^* \lesssim 200$  ps at 4 K (Meier and Zakharchenya, 1984) Since we observe  $T_{MO} > 200$ ps, we ascribe the signal to be due to the quantum dots.

For these reasons, we conclude that the Kerr rotation signal indeed originates from charge carriers in the quantum dots.

Figure 6.7A shows the typical magneto-optical decay time  $T_{MO}$ , which is extracted for the function  $\theta_K(t) \sim e^{-\frac{t}{\tau_{rec}} - \frac{t}{T_{MO}}}$ , for several excitation densities of the He:Ne laser. The  $T_{MO}$  appears to increase from 250 ps up to 500 ps with increasing excitation density. Since the electric field is not the origin of the increase in  $T_{MO}$  in regime III, we associate this increasing trend with a higher occupancy of the quantum dot (i.e.,  $\bar{n} > 1$ ). Note that the excitation densities in this chapter are higher than in Ch. 4, therefore, a situation where  $\bar{n} > 1$  is likely to occur.

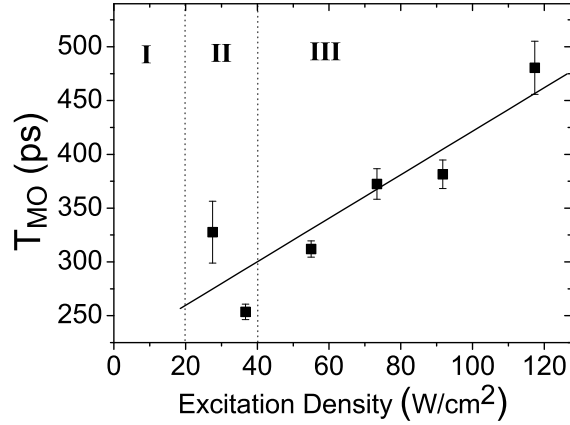


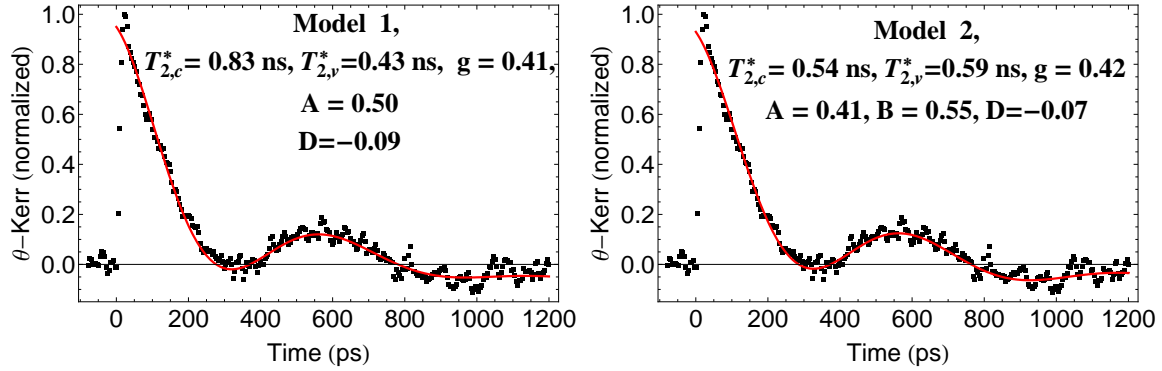
**Figure 6.7:** Magneto-optical decay times  $T_{MO}$  as a function of the CW He:Ne laser excitation density.

In Fig. 6.8, we have plotted example decays with the associated fitted curve and parameters for Model 1 and Model 2. The differences between the quality of the fits can not be observed clearly at first sight. Little difference is found in the variances  $\chi^2$  of the fits for the complete series of data.

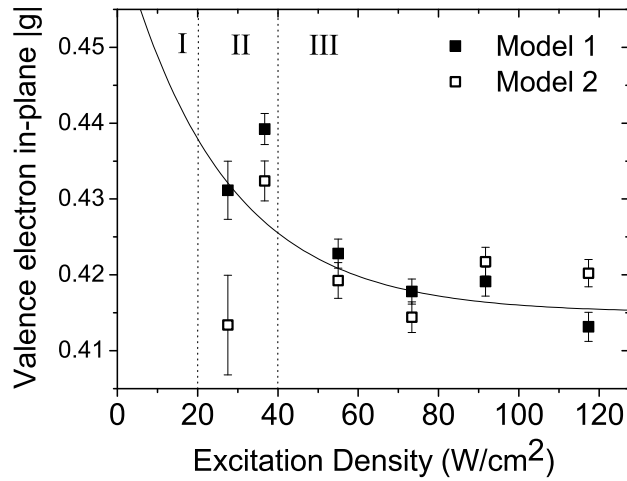
Some of the data, like the data in Fig. 6.8, show small negative values at times  $t > 800$  ps, which can be expected when (i)  $T_{2,c}^* < T_{2,v}^*$  or when (ii) the conduction electron also exhibits some low frequency oscillatory behavior. Since condition (i) would contradict the existing experimental evidence of Gündoğdu *et al.* (2005), we interpret the negative data to be due to a second low frequency precession of the conduction electron. The models 1 and 2 in Eq. 6.5 and Eq. 6.6 effectively incorporate the precession of the conduction electron by the background term  $D$ . Applying a model to the data with two frequencies, setting  $D = 0$ , one rather consistently finds a second frequency to be 10 times smaller than the main frequency, which can be interpreted as a 10 times smaller in-plane  $g$  factor of the conduction electron.

Figure 6.9 shows the in-plane  $g$  factors of the valence electron, where we find an average value  $|g_{v,\parallel}| = 0.42 \pm 0.01$  when there is no electric field (regime III). When the electric field increases (regime II), Model 1 shows a clearly increasing trend, while the increasing trend is less obvious for Model 2. Since the amplitude ratio A/B is not found to be constant for Model 2 for different excitation densities, we consider Model 1 to be more reliable. We thus conclude that  $|g_{v,\parallel}|$  increases with electric field. This trend was also observed in the second measurement series, published by Rietjens *et al.* (2008), where a model similar to Model 1 is applied. Rietjens *et al.* (2008), however, assigns the precession to the conduction electron.

The values for  $T_{2,v}^*$  and  $T_{2,c}^*$ , as a function of the HeNe laser excitation density, are



**Figure 6.8:** Examples of the magneto-optical signal and their fit at 280 mT and an excitation density  $P_{HeNe} = 117 \text{ W/cm}^2$  (regime III) for Model 1 and Model 2. Differences in the fitting quality of both models cannot be clearly observed. Small negative values are observed for  $t > 800 \text{ ps}$ . The measurement in this figure contained the most negative data of the complete measurement series.



**Figure 6.9:** The in-plane  $g$  factor of the valence electron as a function of the excitation density. Except for the lowest excitation density point of Model 1, the data shows an increasing trend with increasing electric field. The in-plane  $g$  factor in the case without electric field is  $|g_{v,\parallel}| = 0.42 \pm 0.01$ . The line is a guide to the eye.

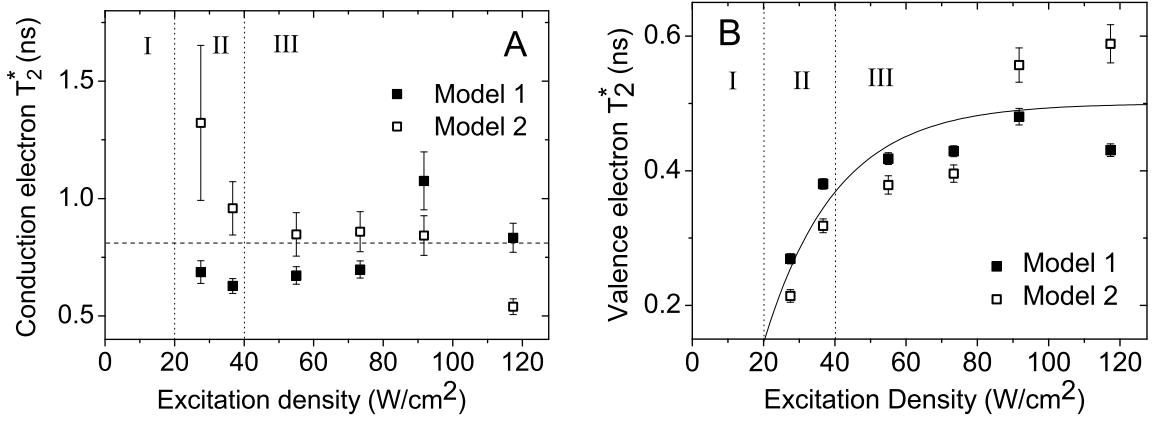


**Figure 6.10:** Values for the conduction electron  $T_{2,c}^*$  (Fig. A) and valence electron  $T_{2,v}^*$  (Fig. B) as a function of the HeNe laser excitation density. The conduction electron is not affected by the electric field, and has a constant value of  $T_{2,c}^* = 830 \pm 70$  ps. The valence electron decoherence time is found to be  $T_{2,v}^* = 490 \pm 90$  ps, but is strongly reduced by the electric field. The line in Fig. B is a guide to the eye.

shown in Fig. 6.10. The conduction electron  $T_{2,c}^*$  in Fig. 6.10A shows larger error bars for Model 2, since it contains an extra fitting parameter. Model 2 shows an increasing trend, while Model 1 shows a slightly decreasing trend of  $T_{2,c}^*$  with increasing electric field. If one assumes the  $T_{2,c}^*$  to be constant with electric field, and takes an average of all the data points, one finds a constant value of  $T_{2,c}^* = 830 \pm 70$  ps.

The valence electron decoherence time, presented in Fig. 6.10B, shows a clear decreasing trend with increasing electric field. In the case without electric field, its value is  $T_{2,v}^* = 490 \pm 90$  ps, while at higher electric fields, the values drop to  $\sim 200$  ps.

One can generally conclude from Fig. 6.10 that the  $T_2^*$  values for the conduction electron are always larger than for the valence electron. This condition,  $T_{2,c}^* > T_{2,v}^*$ , can be explained by a high degree of heavy-hole/light-hole intermixing. In the case of strong intermixing, one can expect spin-flipping processes to be relatively efficient, which leads to quicker decoherence. Moreover, as shown in Fig. 6.10B, the valence electron decoherence time appears to be much more sensitive for the electric field. The shorter decoherence times could be associated with an increased degree of heavy-hole/light-hole intermixing when the electric field is increased.

## 6.4 Discussion

### *g* factors

The trend observed in our data for the *g* factors is similar to that described by Rietjens *et al.* (2008), except that we assign the precession to the valence electron. The increase of the in-plane *g* factor with electric field can be explained by an increased degree of heavy-hole/light-hole intermixing in the valence band. Our value  $|g_{v,\parallel}| = 0.42 \pm 0.01$  can only be compared to experiments performed on slightly different quantum dots. In general, comparison of the *g* factor of quantum dots remains difficult, because its strong dependence on parameters like composition, geometry (elongation), degree of intermixing, and homogeneity of the sample structure. However, the experiment resembling our quantum dots and setup most, is performed by Greilich *et al.* (2006b). They measure on annealed (In,Ga)As quantum dots and find a value of  $|g_{\parallel}| = 0.57$ , which they assign to the conduction electron.

### Spin decoherence times

Among the literature on spin decoherence times in quantum dots, one can distinguish between several types of experiments. In experiments which do not employ a magnetic field (Birkedal *et al.*, 1999; Borri *et al.*, 2001; Paillard *et al.*, 2001; Langbein *et al.*, 2004; Gündoğdu *et al.*, 2005; Laurent *et al.*, 2005), one can in principle not discriminate between  $T_1$  and  $T_2$  times. These experiments generally reveal spin relaxation times between  $\sim 100$  ps and (a few) nanoseconds. A special type of experiments is performed at the Walter Schottky Institute (Garching, Germany), where separation of the electron-hole pair is performed employing diode-structures. These type of experiments are performed in magnetic fields, to measure  $T_1$ , and reveal values exceeding microseconds or even milliseconds, depending on the magnetic field. Like in the measurements in Ch. 4, a strong magnetic field dependence was found for the conduction electron  $T_1$  (Kroutvar *et al.*, 2004) and valence electron  $T_1$  (Heiss *et al.*, 2007). Further recent state-of-the-art measurements are single dot Kerr rotation measurements (Mikkelsen *et al.*, 2007) and the coherent optical manipulation of the electron spin in a quantum dot (Berezovsky *et al.*, 2008). Mikkelsen *et al.* (2007) reports a  $T_2^*$  time of 8.4 ns for the conduction electron, at a magnetic field of 50 mT. Values for the  $T_1$  of the hole in a single quantum dot have recently been reported as well (Gerardot *et al.*, 2008), reaching over 0.5 ms.

Like for the in-plane *g* factors, it is hard to compare the different experiments. The most comparable experiments to our system are done by Gündoğdu *et al.* (2005), which report 120 ps for the conduction electron and  $\sim 30$  ps for the valence electron. This experiment has been performed at 77 K, and no magnetic field has been employed.

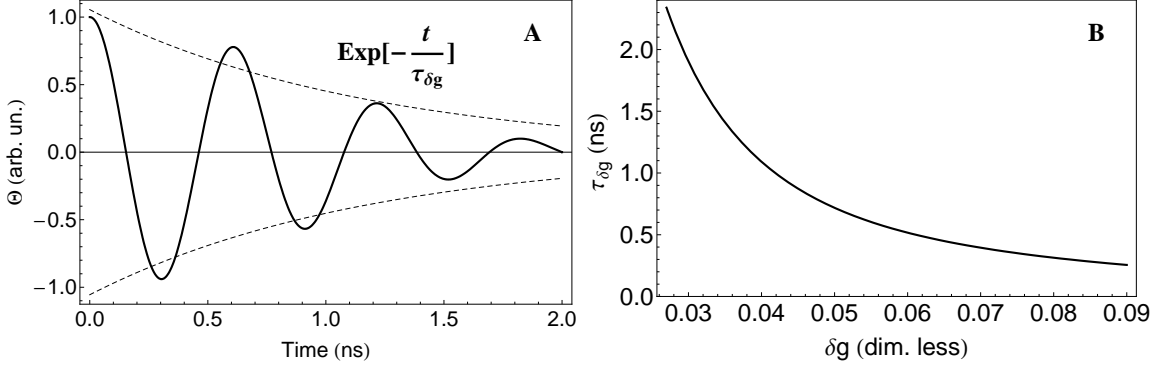


**Figure 6.11:** A distribution in the  $g$  factors between different quantum dots in the excitation spot leads to an nearly exponential decay (if one assumes a Gaussian distribution of  $g$  factors). Figure A shows the signal decay arising *only* from a distribution of  $g$  factors, where  $\bar{g} = 0.35$  and  $\delta g = 0.04$ . Figure B shows the time constants  $\tau_{\delta g}$  which approximate the decay for different standard deviations  $\delta g$ .

Another Kerr rotation experiment, on annealed quantum dots, has been performed by Greilich *et al.* (2006b), which revealed  $T_{2,c}^* = 2$  ns at a magnetic field of 1 T. In the experiment by Greilich *et al.* (2006b), the decoherence time is purely attributed to the 'reversible' decoherence due to an inhomogeneous distribution of  $g$  factors for the quantum dots within the probing laser spot.

To investigate the effect of an inhomogeneous distribution of precession frequencies on the signal decay, we assume a normalized Gaussian distribution  $f(g)$  of the  $g$  factors within the probing spot. The Kerr rotation signal decays due to a distribution of frequencies in the ensemble, and can be written as

$$I(t) \sim \int_g f(g) \times H(t) \cos\left(\frac{g\mu_B B}{\hbar} t\right) dg \approx \cos\left(\frac{\bar{g}\mu_B B}{\hbar} t\right) e^{-\left(\frac{t}{\tau_{\delta g}}\right)} \quad (6.7)$$

where  $g$  is integrated over the complete range of  $g$  factors. The function  $H(t)$  represents a Heaviside function, which only selects values with  $t > 0$ . The integration over the periodic signals with a Gaussian distribution  $f(g)$  leads to a nearly exponential decay for the intensity, of which an example is given in Fig. 6.11A. The comparison of this integral with an exponential decay arises just from the inspection of the calculated graphs and is not based on an analytical derivation. The time constant of the decay of the signal due to the  $g$  factor distribution with dispersion  $\delta g$  is denoted  $\tau_{\delta g}$ . Figure 6.11A shows the signal decay for a  $\bar{g} = 0.35$  and a standard deviation of  $\delta g = 0.04$ . The dashed line in Fig. 6.11 shows an exponential decay with  $\tau_{\delta g} = 1.25$  ns. Figure 6.11B shows the values for  $\tau_{\delta g}$  as a function of  $\delta g$  in the distribution  $f(g)$ . A larger width  $\delta g$  of the  $g$  factor distribution leads to a decrease of  $\tau_{\delta g}$ . Greilich *et al.* (2006b) reports  $\delta g \approx 0.005$  for a laser band width of 15 meV. With this value in mind, one can claim that the  $\tau_{\delta g}$



is exceeding  $10 \sim 100$  ns.

Besides the reversible decoherence due to an inhomogeneous  $g$  factor distribution (this type of decoherence is reversible since the  $g$  factor distribution is static), one should also include the effects of the hyperfine-induced (reversible) decoherence (Khaetskii *et al.*, 2002; Merkulov *et al.*, 2002). The origin of this process is the small variation in the effective nuclear magnetic field per quantum dot, which can be considered static on the timescale of the decoherence (dipole-interaction of the nuclei is of the order  $10^{-4}$  s (Khaetskii *et al.*, 2002)). The associated timescale,  $T_{\Delta}$ , is of the order of nanoseconds, depending on the type of material and size of the quantum dot. One can therefore expect that  $T_{\Delta} < \tau_{\delta g}$ . Due to this condition, the hyperfine-induced decoherence is likely to be the most important source of inhomogeneous broadening effects in the Kerr rotation signal.

Without precise knowledge of the inhomogeneous broadening effects in the ensemble of quantum dots, it is hard to make conclusions on the 'pure'  $T_2$ . To gain clear insight in this parameter, one is forced to perform single dot measurements, as executed by Berezovsky *et al.* (2006, 2008) and Mikkelsen *et al.* (2007).

## Summary

Semiconductor quantum dots have improved solid-state laser technology and introduced a new controllable zero-dimensional system to physicists. Next to laser technology, they can be applied as memory elements and (infrared) detectors as well. Quantum dots are commonly grown by epitaxial methods like Molecular Beam Epitaxy (MBE) or Metal-Organic Chemical Vapour Deposition (MOCVD), where they are embedded as a layer or multiple layers in a larger bulk-type structure. In this work, we study a MBE-grown single layer of (In,Ga)As quantum dots, which is embedded in the middle of a  $p-i-n$  junction of GaAs material.

Charge carriers in quantum dots experience little disturbance from the bulk semiconductor environment, which, for example, leads to relatively long spin relaxation times. For these long spin relaxation times, in particular spin decoherence times (i.e., phase-related relaxation), quantum dots have been mentioned as possible elements in quantum information devices. The spin of the electron can be employed for quantum information purposes, acting as the base element of these systems, the qubit. In one of the proposed device architectures, each quantum dot of the array hosts a charge carrier, which spin is addressed by a radio-frequent field. To achieve addressability of *each* of the charge carriers in the array, one requires a locally tunable  $g$  factor. The  $g$  factor is a measure for the energy splitting between Zeeman levels of the quantum dot in a magnetic field, and is proportional to the required frequency of the radio-frequent field.

This thesis considers several of these quantum information related subjects for self-assembled (In,Ga)As quantum dots. First of all, a general introduction to quantum dots and a motivation is given in Chapter 1. Chapter 2 discusses some more specific subjects of quantum dots in magnetic and electric fields, whereas chapter 3 discusses the experimental setups. Chapter 4, 5, and 6 present the main results of the thesis, pointed out in the next paragraphs.

Chapter 4 presents data on the degree of circular polarization of the photoluminescence (PL) of quantum dots. This data is measured in a magnetic field, which leads to a Zeeman splitting (proportional to the  $g$  factor) between spin eigenstates of the energy levels within the quantum dot. Each of the levels emits circularly polarized photons with opposite helicity. In the case of an unbalanced occupancy of the levels, one observes a degree of circular polarization of the PL. This circular polarization contains information about the sign of the  $g$  factor, the magnitude of the  $g$  factor and the spin relaxation times between the Zeeman levels. Furthermore, we employ the built-in electric field of the  $p-i-n$  structure of the GaAs host material. By excitation of an additional continuous

wave laser, the built-in electric field can be varied, which has its signature in the Stark shift in the PL spectra of the quantum dots.

The first part of chapter 4 presents data in a magnetic field of 7 T, where the degree of circular polarization changes its sign in the same excitation density regime where the Stark shift (i.e., electric field) varies. We associate the sign change of the polarization with a sign change of the exciton  $g$  factor in the growth direction (where the exciton is a combined particle of the electron and hole). Since the Stark shift provides a measure for the electric field, we estimate the sign change to occur for electric fields exceeding 150 kV/cm. The sign change of the polarization is observed throughout the whole PL energy range, including the lowest energies, which excludes a sign change induced by excited states.

The magnitude of the degree of circular polarization is considered in the second part of chapter 4. The magnitude of the polarization is a measure for the spin relaxation time between the exciton spin levels. We measure the magnetic field dependence of the polarization to determine the magnetic field dependence of the spin relaxation time. We observe the exciton spin relaxation time to follow a power law behavior with the magnetic field, which matches with a theoretical prediction of Tsitsishvili *et al.* from 2003. In high electric fields, the strong power law behavior is left and a much weaker dependence with magnetic field occurs. This confirms that quantum dots provide good spin conservation conditions for charge carriers.

Chapter 5 discusses the electric field dependence of the recombination time in quantum dots. We utilize time- and spectrally-resolved PL data to combine the variation of the signal decay (related to the recombination time) and the time-dependent Stark shift. Like in chapter 4, the Stark shift at every time is a measure for the electric field. Recombination times increase from  $\sim 1$  ns when there is no electric field up to  $\sim 4$  ns at electric fields close to 200 kV/cm. Moreover, we observe a significant drop in the PL intensity at electric fields above 200 kV/cm. This is associated with tunneling of charge carriers out of the quantum dot.

In addition to the growth direction  $g$  factors, studied in chapter 4, we consider the in-plane  $g$  factor in chapter 6. In-plane  $g$  factors are difficult to probe in experiments involving luminescence, due to optical selection rules and complex experimental geometries. A common method to measure them is by time-resolved Kerr rotation spectroscopy, where the precession of the signal in a magnetic field is proportional to the in-plane  $g$  factor, which is applied in this chapter as well. Next to the required pulsed laser to determine the temporal dependence of the signal, we employ a continuous wave He:Ne laser to control the electric field over the quantum dots. Furthermore, a relatively small in-plane magnetic field of 280 mT is applied. The oscillations in the signal indicate

spin precession. Calculations of J.A.F.S. Pingenot and M.E. Flatté indicate that the highest frequency is likely due to the valence electron. Without electric field over the quantum dots, the in-plane valence electron  $g$  factor is found to be  $0.42 \pm 0.01$ , whereas in electric fields exceeding 50 kV/cm, the in-plane  $g$  increases slightly (not more than 0.02). The spin decoherence time of the valence electron is found to be larger than the conduction electron for all electric fields. Both are in the order of hundreds of picoseconds. We estimate the hyperfine-interaction to induce a significant effect of decoherence of the spin of the charge carriers.



## Acknowledgements

Let me first thank Andrei Silov and first promotor Paul Koenraad, with who I have spent a significant amount of time reading and correcting this thesis, and Michael Flatté for critically reading and commenting on the thesis as a second promotor. Andrei, thanks for encouraging me to pursue results autonomously, and Paul, you have sharpened my sense for writing. I thank the defense committee members for their careful reading and critics on the first manuscript. I would also like to thank Joachim Wolter for giving me this chance in the first place.

If I include my master thesis research, I have stayed almost six years in the group 'Photonics and Semiconductor Nanophysics'. Although I owe all members of the group some gratitude, some persons have been particularly closely involved in this work. Most obviously, this was the 'optical' sub-group of Andrei Silov, which included Tom Campbell Ricketts, Andrei Yakunin, Pavel Blajnov, Twan van Lippen, Tom Eijkemans and recently also Niek Kleemans. Tom C.R., thanks for your support, your exceptionally persevering state-of-mind, and your introduction to sub-smidgin engineering. Working with our internship student and stock-exchange-analyst Joris Goudsmit has been inspiring as well, not only financially.

Jos van Ruijven, Tom Eijkemans, Frans van Setten, Peter Nouwens and Rian Hamhuis have been crucial for the success in the technical requirements of this work. It could not have succeeded without the knowledge, flexibility and experience of you. Moreover, your jokes during coffee-breaks act as oil for the rusty analytical mind.

I thank Carlos Bosco, Jeroen Rietjens and Bert Koopmans for the collaboration on the Kerr rotation experiments, and for your exceptional experimental and theoretical expertise in this field. You were always ready for a discussion, which most of the times led to new ideas.

The fruitful collaboration with Joseph Pingnot and Michael Flatté of the Department of Physics and Astronomy of the University of Iowa has provided us insights in the interpretation of the Kerr rotation measurements and took place in a motivating atmosphere.

Margriet, thanks for your flexibility during my numerous visits to your office. Without your personality, the group would be subjected to 'a greater degree of decoherence'.

The staff scientists Rob van der Heijden, Jos Haverkort and Richard Nötzel have been decisive in social and scientific issues related to this thesis. Also my former office colleague Erik Bogaart and nearly office colleague Dilna Sreenivasan played an important role by expressing their experiences with the practice of graduate student research. Dilna

and Vinit, thanks for your extraordinary hospitality during my visit in India.

I would like to thank my parents, brother, closest friends and family for their support during these years. You have been exceptional in your consolation and encouragement, as well as your practical support on many occasions.

*Thanks for your support!*

*Guido*

*Eindhoven, 12<sup>th</sup> of July, 2008*

# Bibliography

- Adler, F., M. Geiger, A. Bauknecht, F. Scholz, H. Schweizer, M. H. Pilkuhn, B. Ohnesorge, and A. Forchel, 1996, *J. Appl. Phys.* **80**, 4019.
- Alloing, B., C. Zinoni, L. H. Li, A. Fiore, and G. Patriarche, 2007, *J. of Appl. Phys.* **101**, 024918.
- Anantathanasarn, S., Y. Barbarin, N. I. Cade, P. J. van Veldhoven, E. A. J. M. Bente, Y. S. Oei, H. Kamada, M. K. Smit, and R. Nötzel, 2008, *Materials Science and Engineering B* **147**, 124.
- Anderlini, M., P. J. Lee, B. L. Brown, J. Seby-Strabley, W. D. Phillips, and J. V. Porto, 2007, *Nature* **448**, 452.
- Atatüre, M., J. Dreiser, A. Badolato, A. Högele, K. Karrai, and A. Imamoglu, 2006, *Science* **312**, 551.
- Atatüre, M., J. Dreiser, A. Badolato, and A. Imamoglu, 2007, *Nature Physics* **3**, 101.
- Awschalom, D. D., J.-M. Halbout, S. von Molnar, T. Siegrist, and F. Holtzberg, 1985, *Phys. Rev. Lett.* **55**, 1128.
- Babinski, A., G. Ortner, S. Raymond, M. Potemski, M. Bayer, W. Sheng, P. Hawrylak, Z. Wasilewski, S. Fafard, and A. Forchel, 2006, *Phys. Rev. B* **74**, 075310.
- Bacher, G., R. Weigand, J. Seufert, V. D. Kulakovskii, N. A. Gippius, A. Forchel, K. Leonardi, and D. Hommel, 1999, *Phys. Rev. Lett.* **83**, 4417.
- Bayer, M., A. Kuther, A. Forchel, A. Gorbunov, V. B. Timofeev, F. Schafer, J. P. Reithmaier, T. L. Reinecke, and S. N. Walck, 1999, *Phys. Rev. Lett.* **82**, 1748.
- Bayer, M., T. L. Reinecke, F. Weidner, A. Larionov, A. McDonald, and A. Forchel, 2000, *Phys. Rev. Lett.* **86**, 3168.
- Bayer, M., V. B. Timofeev, T. Gutbrod, A. Forchel, R. Steffen, and J. Oshinowo, 1995, *Phys. Rev. B* **52**, 11623R.
- Bennemann, K. H., 1998, *Nonlinear optics in metals* (Oxford Science Publications).
- Berezovsky, J., M. H. Mikkelsen, O. Gywat, N. G. Stoltz, L. A. Coldren, and D. D. Awschalom, 2006, *Science* **314**, 1916.
- Berezovsky, J., M. H. Mikkelsen, N. G. Stolz, L. A. Coldren, and D. D. Awschalom, 2008, *Science* **320**, 349.



- Birkedal, D., K. Leosson, and J. M. Hvam, 1999, *Phys. Rev. Lett.* **87**, 227401.
- Björk, M. T., A. Fuhrer, A. E. Hanssen, M. W. Larsson, L. E. Fröberg, and L. Samuelson, 2005, *Phys. Rev. B* **72**, 201307R.
- Blokland, J. H., F. J. P. Wijnen, P. C. M. Christianen, U. Zeitler, J. C. Maan, P. Kailuweit, D. Reuter, and A. D. Wieck, 2007, *Phys. Rev. B* **75**, 233305.
- Blum, K., 1981, *Density matrix theory and applications* (Plenum Press).
- Bockelmann, U., W. Heller, and G. Abstreiter, 1997, *Phys. Rev. B* **55**, 4469.
- Borri, P., W. Langbein, S. Schneider, U. Woggon, R. L. Sellin, D. Ouyang, and D. Bimberg, 2001, *Phys. Rev. Lett.* **87**, 157401.
- Bruls, D. M., J. W. A. M. Vugs, P. M. Koenraad, H. W. M. Salemink, and J. H. Wolter, 2002, *J. Cryst. Growth* **81**, 1708.
- Bulashevich, K. A., S. Y. Karpov, and R. A. Suris, 2006, *Phys. Status Solidi B* **243**, 1625.
- Camilleri, C., F. Teppe, D. Scalbert, Y. G. Semenov, M. Nawrocki, M. Dyakonov, J. Sibert, S. Tatarenko, and T. Wojtowicz, 2001, *Phys. Rev. B* **64**, 085331.
- Chang, W. H., T. M. Hsu, C. C. Huang, S. L. Hsu, C. Y. Lai, N. T. Yeh, T. E. Nee, and J. I. Chyi, 2000, *Phys. Rev. B* **62**, 6959.
- Chen, G., N. H. Bonadeo, D. G. Steel, D. Gammon, D. S. Katzer, D. Park, and L. J. Sham, 2000, *Science* **289**, 1906.
- Chen, P., C. Piermarocchi, L. J. Sham, D. Gammon, and D. G. Steel, 2004, *Phys. Rev. B* **69**, 075320.
- Chen, Z., R. Bratschitsch, S. G. Carter, S. T. Cundiff, D. R. Yakovlev, G. Karczewski, T. Wojtowicz, and J. Kossut, 2007, *Phys. Rev. B* **75**, 115320.
- Cortez, S., O. Krebs, P. Voisin, and J. M. Gérard, 2001, *Phys. Rev. B* **63**, 233306.
- Crooker, S. A., J. J. Baumberg, F. Flack, N. Samarth, and D. D. Awschalom, 1996, *Phys. Rev. Lett.* **77**, 2814.
- Dekel, E., D. V. Regelman, D. Gershoni, E. Ehrenfreund, W. V. Schoenfeld, and P. M. Petroff, 2000, *Phys. Rev. B* **62**, 11038.
- Deveaud, B., F. Clrot, N. Roy, K. Satzke, B. Sermage, and D. S. Katzer, 1991, *Phys. Rev. Lett.* **67**, 2355.
- Dutt, M. V. G., J. Cheng, B. Li, X. Xu, X. Li, P. R. Berman, D. G. Steel, A. S. Bracker, D. Gamman, S. E. Economou, R. B. Liu, and L. J. Sham, 2005, *Phys. Rev. Lett.* **94**, 227403.
- Ediger, M., G. Bester, A. Badolato, P. M. Petroff, K. Karrai, A. Zunger, and R. J. Warburton, 2007, *Nature Physics* **3**, 774.

- Elzerman, J. M., M. Hanson, L. H. W. van Beveren, B. Witkamp, L. M. K. Vandersypen, and L. P. Kouwenhoven, 2004, *Nature* **430**, 431.
- Empedocles, S. A., and M. G. Bawendi, 1997, *Science* **278**, 2114.
- Epstein, R. J., D. T. Fuchs, W. V. Schoenfeld, P. M. Petroff, and D. D. Awschalom, 2001, *Appl. Phys. Lett.* **78**, 733.
- Ferreira, R., and G. Bastard, 1999, *Appl. Phys. Lett.* **74**, 2818.
- Finley, J. J., D. J. Mowbray, M. S. Skolnick, A. D. Ashmore, C. Baker, A. F. G. Monte, and M. Hopkinson, 2002, *Phys. Rev. B* **66**, 153316.
- Finley, J. J., M. Subathil, P. Vogl, G. Abstreiter, R. Oulton, A. I. Tartakovskii, D. J. Mowbray, M. S. Skolnick, S. L. Liew, A. G. Cullis, and M. Hopkinson, 2004, *Phys. Rev. B* **70**, 201308.
- Flissikowski, T., I. A. Akimov, A. Hundt, and F. Henneberger, 2003, *Phys. Rev. B* **68**, 161309R.
- Flissikowski, T., A. Hundt, M. Lowisch, M. Rabe, and F. Henneberger, 2001, *Phys. Rev. Lett.* **86**, 3172.
- Fry, P. W., J. J. Finley, L. R. Wilson, A. Lemaitre, D. J. Mowbray, M. S. Skolnick, M. Hopkinson, G. Hill, and J. C. Clark, 2000a, *Appl. Phys. Lett.* **77**, 4344.
- Fry, P. W., I. E. Itskevich, D. J. Mowbray, M. S. Skolnick, J. J. Finley, J. A. Barker, E. P. O'Reilly, L. R. Wilson, I. A. Larkin, P. A. Maksym, M. Hopkinson, M. Al-Khafaji, *et al.*, 2000b, *Phys. Rev. Lett.* **84**, 733.
- Gammon, D., E. S. Snow, B. V. Shanabrook, D. S. Katzer, and D. Park, 1996, *Phys. Rev. Lett.* **76**, 3005.
- Gayral, B., J.-M. Gérard, B. Sermage, A. Lemaître, and C. Dupuis, 2001, *Appl. Phys. Lett.* **78**, 2828.
- Geiger, M., 1998, University of Ulm, *Selbstorganisationseffekte bei Quantenpunkten*, Ph.D. thesis.
- Gerard, J. M., B. Sermage, B. Gayral, B. Legrand, E. Costard, and V. Thierry-Mieg, 1998, *Phys. Rev. Lett.* **81**, 1110.
- Gerardot, B. D., D. Brunner, P. A. Dalgarno, P. Öhberg, S. Seidl, M. Kroner, K. Karrai, N. G. Stoltz, P. M. Petroff, and R. J. Warburton, 2008, *Nature* **451**, 441.
- Gong, Q., P. Offermans, R. Nötzel, P. M. Koenraad, and J. H. Wolter, 2004, *Appl. Phys. Lett.* **85**, 5697.
- Goni, A. R., H. Born, R. Heitz, A. Hoffmann, C. Thomsen, F. Heinrichsdorff, and D. Bimberg, 2000, *Jap. J. Appl. Phys.* **39**, 3907.
- Gorman, J., D. G. Hasko, and D. A. Williams, 2005, *Phys. Rev. Lett.* **95**, 090502.
- Gotoh, H., H. Ando, H. Kamada, and A. Chavez-Pirson, 1998, *Appl. Phys. Lett.* **72**, 1341.
- Graham, L. A., D. L. Huffaker, and D. G. Deppe, 1999, *Phys. Rev. Lett.* **74**, 2408.

- Greulich, A., R. Oulton, E. A. Zhukov, I. A. Yugova, D. R. Yakolev, M. Bayer, A. Shabaev, A. L. Efros, I. A. Merkulov, V. Stavarache, D. Reuter, and A. Wieck, 2006a, *Phys. Rev. Lett.* **96**, 227401.
- Greulich, A., D. R. Yakovlev, A. Shabaev, A. L. Efros, I. A. Yugova, R. Oulton, V. Stavarache, D. Reuter, A. Wieck, and M. Bayer, 2006b, *Science* **313**, 341.
- Gündoğdu, K., K. C. Hall, E. J. Koerperick, C. E. Pryor, M. E. Flatté, and T. F. Bogess, 2005, *Appl. Phys. Lett.* **86**, 113111.
- Gupta, J. A., D. D. Awschalom, X. Peng, and A. P. Alivisatos, 1999, *Phys. Rev. B* **59**, R10421.
- Hanson, R., B. Witkamp, L. M. K. Vandersypen, L. H. W. van Beveren, J. M. Elzerman, and L. P. Kouwenhoven, 2003, *Phys. Rev. Lett.* **91**, 196802.
- Heine, V., 1993, *Group theory in quantum mechanics* (Dover).
- Heiss, D., S. Schaeck, H. Huebl, M. Bichler, G. Abstreiter, and J. J. Finley, 2007, *Phys. Rev. B* **76**, 241306R.
- Heyn, C., A. Bolz, T. Maltezopoulos, R. L. Johnson, and W. Hansen, 2005, *J. Cryst. Growth* **278**, 46.
- Heyn, C., and W. Hansen, 2003, *J. Cryst. Growth* **251**, 140.
- Hours, J., P. Senellart, E. Peter, A. Cavanna, and J. Bloch, 2005, *Phys. Rev. B* **71**, 161306.
- Hsu, T. M., W. H. Chang, C. C. Huang, N. T. Yeh, and J. I. Chyi, 2001, *Appl. Phys. Lett.* **78**, 1760.
- Hyland, J. T., G. T. Kennedy, A. Miller, and C. C. Button, 1999, *Semicond. Sci. Technol.* **14**, 215.
- Imamoglu, A., D. D. Awschalom, G. Burkard, D. P. DiVincenzo, D. Loss, M. Sherwin, and A. Small, 1999, *Phys. Rev. Lett.* **83**, 4204.
- Itskevich, I. E., S. I. Rybchenko, I. I. Tartakovskii, S. T. Stoddart, A. Levin, P. C. Main, L. Eaves, M. Henini, and S. Parnell, 2000, *Appl. Phys. Lett.* **76**, 3932.
- Jin, P., C. M. Li, Z. Y. Zhang, F. Q. Liu, Y. H. Chen, X. L. Ye, B. Xu, and Z. G. Wang, 2004, *Appl. Phys. Lett.* **85**, 2791.
- Joyce, P. B., T. J. Kryzewski, G. R. Bell, B. A. Joyce, and T. S. Jones, 1998, *Phys. Rev. B* **58**, R15981.
- Kaji, R., S. Adachi, H. Sasakura, and S. Muto, 2007, *Appl. Phys. Lett.* **91**, 261904.
- Kane, B., 1998, *Nature* **393**, 133.
- Kane, E. O., 1957, *J. Phys. Chem. Solids* **1**, 249.
- Kane, E. O., 1959, *J. Phys. Chem. Solids* **8**, 38.
- Kanno, A., and Y. Masumoto, 2006, *Phys. Rev. B* **73**, 073309.
- Katayama, T., Y. Suzuki, M. Hayashi, and A. Thiaville, 1993, *J. of Magnetism and Magn. Mat.* **126**, 527.

- Kato, Y., R. C. Myers, D. C. Driscoll, A. C. Gossard, J. Levy, and D. D. Awschalom, 2003, *Science* **299**, 1201.
- Kennedy, T. A., A. Shabaev, M. Scheibner, A. L. Efros, A. S. Bracker, and D. Gammon, 2006, *Phys. Rev. B* **73**, 045307.
- Khaetskii, A. V., D. Loss, and L. Glazman, 2002, *Phys. Rev. Lett.* **88**, 186802.
- Khaetskii, A. V., and Y. V. Nazarov, 2000, *Phys. Rev. B* **61**, 12639.
- Khaetskii, A. V., and Y. V. Nazarov, 2001, *Phys. Rev. B* **64**, 125316.
- Kikkawa, J. M., and D. D. Awschalom, 1999, *Phys. Rev. Lett.* **80**, 4313.
- Kiraz, A., P. Michler, C. Becher, B. Gayral, and A. Imamoglu, 2001, *Appl. Phys. Lett.* **78**, 3932.
- Köhler, K., H. J. Polland, L. Schultheis, and C. W. Tu, 1988, *Phys. Rev. B* **38**, 5496.
- Koopmans, B., and W. J. M. de Jonge, 1999, *Appl. Phys. B* **68**, 525.
- Koopmans, B., M. G. Koerkamp, T. Rasing, and H. van den Berg, 1995, *Phys. Rev. Lett.* **74**, 3692.
- Koppens, F. H. L., C. Buizert, K. J. Tielrooij, I. T. Vink, K. C. Nowack, T. Meunier, L. P. Kouwenhoven, and L. M. K. Vandersypen, 2006, *Nature* **442**, 766.
- Kotlyar, R., T. L. Reinecke, M. Bayer, and A. Forchel, 2001, *Phys. Rev. B* **63**, 085310.
- Kroutvar, M., Y. Ducommun, D. Heiss, M. Bichler, D. Schuh, G. Abstreiter, and J. J. Finley, 2004, *Nature* **432**, 81.
- Kuo, D. M. T., and Y. C. Chang, 2000, *Phys. Rev. B* **61**, 11051.
- Kuther, A., M. Bayer, A. Forchel, A. Gorbunov, V. B. Timofeev, F. Schaefer, and J. P. Reithmaier, 1998, *Phys. Rev. B* **58**, R7508.
- Langbein, W., P. Borri, U. Woggon, V. Stavarache, D. Reuter, and A. D. Wieck, 2004, *Phys. Rev. B* **70**, 033301.
- Larkin, I., and A. Vagov, 2003, *Phys. Rev. B* **67**, 115318.
- Laurent, S., B. Eble, O. Krebs, A. Lemaitre, B. Urbaszek, X. Marie, T. Amand, and P. Voisin, 2005, *Phys. Rev. Lett.* **94**, 147401.
- Li, X., Y. Wu, D. Steel, D. Gammon, T. H. Stievater, D. S. Katzer, D. Park, C. Piermarocchi, and L. J. Sham, 2003, *Science* **301**, 809.
- Loss, D., and D. P. DiVincenzo, 1998, *Phys. Rev. A* **57**, 120.
- Lü, C., J. L. Cheng, and M. W. Wu, 2005, *Phys. Rev. B* **71**, 075308.
- Mackowski, S., T. A. Nguyen, H. E. Jackson, L. M. Smith, J. Kossut, and G. Karczewski, 2003, *Appl. Phys. Lett.* **83**, 5524.

- Marshall, D., and A. Miller, 2001, *Optical and quantum electronics* **33**, 1019.
- Masumoto, Y., S. Oguchi, B. Pal, and M. Ikezawa, 2006, *Phys. Rev. B* **74**, 205332.
- Medeiros-Ribiero, G., E. Ribiero, and H. Westfahl Jr., 2003, *Appl. Phys. A* **77**, 725.
- Mégy, R., A. Bounouh, Y. Suzuki, P. Beauvillain, P. Bruno, C. Chappert, B. Lecuyer, and P. Veillet, 1995, *Phys. Rev. B* **51**, 5586.
- Meier, F., and B. Zakharchenya, 1984, *Optical Orientation* (Elsevier, North-Holland).
- Mensing, T., S. Reitzenstein, A. Löffler, J. P. Reithmaier, and A. Forchel, 2006, *Physica E* **32**, 131.
- Merkulov, I. A., A. I. Efros, and M. Rosen, 2002, *Phys. Rev. B* **65**, 205309.
- Mikkelsen, M. H., J. Berezovsky, N. G. Stoltz, L. A. Coldren, and D. D. Awschalom, 2007, *Nature Physics* **3**, 770.
- Miller, D. A. B., D. S. Chemla, T. C. Damen, A. C. Gossard, W. Wiegmann, T. H. Wood, and C. H. Burrus, 1984, *Phys. Rev. Lett.* **53**, 2173.
- Miller, D. A. B., D. S. Chemla, T. C. Damen, A. C. Gossard, W. Wiegmann, T. H. Wood, and C. H. Burrus, 1985, *Phys. Rev. B* **32**, 1043.
- Miller, D. A. B., D. S. Chemla, and S. Schmitt-Rink, 1986, *Phys. Rev. B* **33**, 6976.
- Morris, D., N. Perret, and S. Fafard, 1999, *Appl. Phys. Lett.* **75**, 3593.
- Mukai, K., N. Ohtsuka, H. Shoji, and M. Sugawara, 1996, *Phys. Rev. B* **54**, R5243.
- Nakaoka, T., T. Saito, J. Tatebayashi, and Y. Arakawa, 2004, *Phys. Rev. B* **70**, 235337.
- Nakaoka, T., T. Saito, J. Tatebayashi, S. Hirose, T. Usuki, N. Yokoyama, and Y. Arakawa, 2005, *Phys. Rev. B* **71**, 205301.
- Nötzel, R., 1996, *Semicond. Sci. Technol.* **11**, 1365.
- Nowack, K. C., F. H. L. Koppens, Y. V. Nazarov, and L. M. K. Vandersypen, 2007, *Science* **318**, 1430.
- Obukhov, S. A., A. A. Rogachev, and N. A. Rud', 1980, *Sov. Phys. Solid State* **22**, 1267.
- Oestreich, M., and W. W. Rühle, 1995, *Phys. Rev. B* **74**, 2315.
- Offermans, P., P. M. Koenraad, J. H. Wolter, K. Pierz, M. Roy, and P. A. Maksym, 2005, *Phys. Rev. B* **72**, 165332.
- Oulton, R., J. J. Finley, A. D. Ashmore, I. S. Gregory, D. J. Mowbray, and M. S. Skolnick, 2002, *Phys. Rev. B* **66**, 045313.
- Paillard, M., X. Marie, P. Renucci, T. Amand, A. Jbeli, and J. M. Gerard, 2001, *Phys. Rev. Lett.* **86**, 1634.
- Pellizari, T., S. A. Gardiner, J. I. Cirac, and P. Zoller, 1995, *Phys. Rev. Lett.* **75**, 3788.

- Peter, E., P. Senellart, D. Martrou, A. Lemaître, J. Hours, J. M. Gérard, and J. Bloch, 2005, *Phys. Rev. Lett.* **95**, 067401.
- Petroff, P. M., and S. P. DenBaars, 1994, *Superlattices and Microstructures* **15**, 15.
- Petta, J. R., A. C. Johnson, J. M. Taylor, E. A. Laird, A. Yacoby, M. D. Lukin, C. M. Marcus, M. P. Hanson, and A. C. Gossard, 2005, *Science* **309**, 2180.
- Pioro-Ladrière, M., Y. Tokura, T. Obata, T. Kubo, and S. Tarucha, 2007, *Appl. Phys. Lett.* **90**, 024105.
- Polland, H. . J., L. Schultheis, J. Kuhl, E. O. Göbel, and C. W. Tu, 1985, *Phys. Rev. Lett.* **55**, 2610.
- Preskill, J., 1998, *Proceedings of the Royal Society A* **454**, 469.
- Pryor, C. E., and M. E. Flatté, 2003, *Phys. Rev. Lett.* **91**, 25.
- Pryor, C. E., and M. E. Flatté, 2006, *Phys. Rev. Lett.* **96**, 026804.
- Pryor, C. E., and M. E. Flatté, 2007, *Phys. Rev. Lett.* **99**, 179901(E).
- Quax, G. W. W., T. E. J. C. Ricketts, A. M. Yakunin, T. van Lippen, R. Nötzel, P. M. Koenraad, C. A. C. Bosco, J. H. H. Rietjens, B. Koopmans, and A. Y. Silov, 2008, *Physica E* **40**, 1832.
- Rajh, T., O. I. Micic, and A. J. Nozik, 1993, *J. Phys. Chem.* **97**, 11999.
- Raymond, S., S. Fafard, P. J. Poole, A. Wojs, P. Hawrylak, S. Charbonneau, D. Leonard, R. Leon, P. M. Petroff, and J. L. Merz, 1996, *Phys. Rev. B* **54**, 11548.
- Reed, M. A., J. N. Randall, R. J. Aggarwal, R. J. Matyi, T. M. Moore, and A. E. Wetsel, 1987, *Phys. Rev. Lett.* **60**, 535.
- Reed, M. A., J. N. Randall, R. J. Aggarwal, R. J. Matyi, T. M. Moore, and A. E. Wetsel, 1988, *Phys. Rev. Lett.* **60**, 535.
- Reithmaier, J. P., G. Şek, A. Löffler, C. Hofmann, S. Kuhn, S. Reitzenstein, L. V. Keldysh, V. D. Kulakovskii, T. L. Reinecke, and A. Forchel, 2004, *Nature* **432**, 197.
- Reuter, D., P. Kailuweit, A. D. Wieck, U. Zeitler, O. Wibbelhoff, C. Meier, and A. L. J. C. Maan, 2005, *Phys. Rev. Lett.* **94**, 026808.
- Rietjens, J. H. H., G. W. W. Quax, C. A. C. Bosco, R. Nötzel, A. Y. Silov, and B. Koopmans, 2008, *J. of Appl. Phys.* **108**, 07B116.
- Roth, L. M., B. Lax, and S. Zwerdling, 1959, *Phys. Rev.* **114**, 90.
- Salis, G., Y. Kato, K. Ensslin, D. C. Driscoll, A. C. Gossard, and D. D. Awschalom, 2001, *Nature* **414**, 619.
- Santori, C., M. Pelton, G. Solomon, Y. Dale, and Y. Yamamoto, 2000, *Phys. Rev. Lett.* **86**, 1502.
- Schliwa, A., M. Winkelkemper, and D. Bimberg, 2007, *Phys. Rev. B* **76**, 205324.

- Schmidt, T., M. Scheibner, L. Worschech, A. Forchel, T. Slobodskyy, and L. W. Molenkamp, 2006, *J. Appl. Phys.* **100**, 123109.
- Sheng, W., 2007, *Physica E* **40**, 1473.
- Sheng, W., and A. Babinski, 2007, *Phys. Rev. B* **75**, 033316.
- Sherwin, M. S., A. Imamoglu, and T. Montroy, 1999, *Phys. Rev. A* **60**, 3508.
- Smith, J. M., P. A. Dalgarno, B. Urbaszek, E. J. McGhee, G. S. Buller, G. J. Nott, R. J. Warburton, J. M. Garcia, W. Schoenfeld, and P. M. Petroff, 2003, *Appl. Phys. Lett.* **82**, 3761.
- Smith, J. M., P. A. Dalgarno, R. J. Warburton, A. O. Govorov, K. Karrai, B. D. Gerardot, and P. M. Petroff, 2005, *Phys. Rev. Lett.* **94**, 197402.
- Solomon, G. S., M. Pelton, and Y. Yamamoto, 2001, *Phys. Rev. Lett.* **86**, 3903.
- Stier, O., M. Grundmann, and D. Bimberg, 1999, *Phys. Rev. B* **59**, 5688.
- Stievater, T. H., X. Li, D. G. Steel, D. Gammon, D. S. Katzer, D. Park, C. Piermarocchi, and L. J. Sham, 2001, *Phys. Rev. Lett.* **87**, 133603.
- Takeuchi, A., R. Ohtsubo, K. Yamaguchi, M. Murayama, T. Kitamura, T. Kuroda, and T. Takagahara, 2004, *Appl. Phys. Lett.* **84**, 3576.
- Tan, I. H., G. L. Snider, L. D. Chang, and E. L. Hu, 1990, *J. Appl. Phys.* **68**, 4071.
- Tartakovskii, A. I., T. Wright, A. Russell, V. I. Fal'ko, A. B. Van'kov, J. Skiba-Szymanska, I. Drouzas, R. S. Kolodka, M. S. Skolnick, P. W. Fry, A. Tahraoui, H.-Y. Liu, *et al.*, 2007, *Phys. Rev. Lett.* **98**, 026806.
- Tarucha, S., D. G. Austing, T. Honda, R. J. van der Hage, and L. P. Kouwenhoven, 1996, *Phys. Rev. Lett.* **77**, 3613.
- Toda, Y., S. Shinomori, K. Suzuki, and Y. Arakawa, 1998, *Appl. Phys. Lett.* **73**, 517.
- Tsitsishvili, E., R. v. Baltz, and H. Kalt, 2003, *Phys. Rev. B* **67**, 205330.
- Tsitsishvili, E., R. v. Baltz, and H. Kalt, 2005, *Phys. Rev. B* **72**, 155333.
- Uhlenbeck, G. E., and S. Goudsmit, 1925, *Naturwissenschaften* **47**, 953.
- Uskov, A. V., F. Adler, H. Schweizer, and M. H. Pilkuhn, 1997, *J. Appl. Phys.* **81**, 7895.
- van Vleck, J. H., 1932, *The theory of electric and magnetic susceptibilities* (Oxford University Press).
- Vrijen, R., E. Yablonovitch, K. Wang, H. W. Jiang, A. Balandin, V. Roychowdhury, T. Mor, and D. DiVincenzo, 2000, *Phys. Rev. A* **62**, 012306.
- Wang, Y., H. S. Djie, and B. S. Ooi, 2006, *Appl. Phys. Lett.* **89**, 151104.
- Ware, M. E., E. A. Stinaff, D. Gammon, M. F. Doty, A. S. Bracker, D. Gershoni, V. L. Korenev, S. C. Bădescu, Y. Lyanda-Geller, and T. L. Reinecke, 2005, *Phys. Rev. Lett.* **95**, 177403.

- Westfahl, H., A. O. Caldeira, G. Medeiros-Ribiero, and M. Cerro, 2004, Phys. Rev. B **70**, 195320.
- Woods, L. M., T. L. Reinecke, and R. Kotlyar, 2004, Phys. Rev. B **69**, 125330.
- Woods, L. M., T. L. Reinecke, and Y. Lyanda-Geller, 2002, Phys. Rev. B **66**, 161318.
- Yu, P. Y., and M. Cardona, 2001, *Fundamentals of semiconductors: physics and material properties* (Springer Verlag).
- Yugova, I. A., A. Greilich, E. A. Zhukov, D. R. Yakovlev, M. Bayer, D. Reuter, and A. D. Wieck, 2007, Phys. Rev. B **75**, 195325.
- Zhukov, E. A., D. R. Yakovlev, M. Bayer, M. M. Glazov, E. L. Ivchenko, G. Karczewski, T. Wojtowicz, and J. Kossut, 2007, Phys. Rev. B **76**, 205310.
- Zrenner, A., E. Beham, S. Stuffer, F. Findeis, M. Bichler, and G. Abstreiter, 2002, Nature **418**, 612.



## Curriculum vitae

- 1979** Born in Breda, The Netherlands
- 1991-1997** Atheneum, Katholieke Scholengemeenschap Etten-Leur
- 1997-1998** First year ('propedeuse') in Applied Mathematics at the Eindhoven University of Technology (TU/e)
- 1997-2003** MSc in Applied Physics at the TU/e
- Internship in the group 'Computer Science and Medical Physics' (currently 'Transport in Permeable Media') at the TU/e, *NMR relaxometrie en diffusometrie aan magnetisch verontreinigde klei en baksteen*, supervised by R.M.E. Valckenborg en prof. dr. K. Kopinga
- Internship at the Department of Chemical Engineering at the University of California at Santa Barbara (USA), *Measurement of absolute radical densities using modulated-beam line-of-sight threshold ionization mass spectrometry*, supervised by S. Agarwal, prof. dr. E.S. Aydil, and prof. dr. ir. M.C.M. van der Sanden
- Master thesis project in the group 'Semiconductor Physics' (currently 'Photonics and Semiconductor Nanophysics') at the TU/e, *Towards spin injection into quantum dots*, supervised by dr. A.Yu. Silov and prof. dr. J.H. Wolter
- 2003-2008** Graduate Research Assistant in the group 'Photonics and Semiconductor Nanophysics' at the Department of Applied Physics of the TU/e, resulting in *All-optical control of the g-factor in self-assembled (In,Ga)As/GaAs quantum dots*



In an arcade of Genova, 2007. Photo by N.A.J.M. Kleemans.

## Publications

*'Optical control over electron g-factor and spin relaxation in (In,Ga)As/GaAs quantum dots'*, J.H.H. Rietjens, G.W.W. Quax, C.A.C. Bosco, R. Nötzel, A.Yu. Silov, B. Koopmans, J. of Appl. Phys., 103, 07B116 (2008)

*'All-optical control of the exciton g-factor in InAs / GaAs quantum dots'*, G.W.W. Quax, T.E.J. Campbell Ricketts, A.M. Yakunin, T. van Lippen, R. Nötzel, P.M. Koenraad, C.A.C. Bosco, J.H.H. Rietjens, B. Koopmans, and A.Yu. Silov, Physica E, 40, 1832 (2008)

*'Measurement of absolute radical densities using modulated-beam line-of-sight threshold ionization mass spectrometry'*, S. Agarwal, G.W.W. Quax, M.C.M. van de Sanden, D. Maroudas, and E.S. Aydil, J. Vac. Sci. Technol. A 22, 71 (2004)

## Prepared for publication

*'Circularly polarized luminescence as a measure for the g-factor and spin relaxation time of the exciton in (In,Ga)As quantum dots in magnetic field'* (content of chapter 4), G.W.W. Quax *et al.*, either Phys. Rev. B or J. of Appl. Phys.

## Conference presentations (oral)

Physics @ Veldhoven, Stichting FOM, January 2008, *'All-optical control of the exciton g-factor in (In,Ga)As/GaAs quantum dots'* by G.W.W. Quax, T.E.J. Campbell Ricketts, R. Nötzel, A.Yu. Silov, and P.M. Koenraad

52nd Magnetism and Magnetic Materials conference, Tampa, Florida, USA, November 2007 *'Optical control over electron g-factor and spin relaxation in InAs/GaAs quantum dots'*, J.H.H. Rietjens, G.W.W. Quax, C.A.C. Bosco, R. Nötzel, A.Yu. Silov and B. Koopmans

13th International conference on Modulated Semiconductor Structures, Genova, Italy, July 2007, *'All-optical control of the exciton g-factor in (In,Ga)As/GaAs quantum dots'*, G.W.W. Quax, T.E.J. Campbell Ricketts, A.M. Yakunin, T. van Lippen, R. Nötzel, P.M. Koenraad, C.A.C. Bosco, J.H.H. Rietjens, B. Koopmans, and A.Yu. Silov